technische universität
dortmund

Dissertation

Real-time monitoring of nanoparticle production with SAXS and DLS

zur Erlangung des Doktorgrades der Naturwissenschaften
der Fakultät Physik der Technischen Universität Dortmund

eingereicht von:

Alexander Schwamberger

September 2014

Contents

Chapter 1

Introduction

Nanoscience deals with tiny structures and objects in the nanometer range. In the nanometer range objects may exhibit different properties compared to their bulk counterparts. However, not only size determines the properties, but other parameters, including the surface and shape of the objects. Thus, modification of the size, shape and the surface in a controlled way enables to engineer materials with novel properties, consequently, making accessible new applications and possibilities that can serve to solve a problem in a smarter or more effective way.

Nanoparticles have become a subject of intense investigations owing to their broad range of features depending on the material, size, shape and the structure. They can serve as a precursor for further processing such as functionalization for bioimaging and biolabling applications [49, 80] and for optoelectronic applications [41, 70] owing to the possibility to tailor the electronic band structure by adjusting the core-shell structure. Moreover, nanoparticles can be used for catalytic applications [19]. Due to the broad field of applications a high demand on diversed nanoparticles is generated. Therefore, efficient and reproducible methods of the nanoparticle production with a high yield are required. Additionally, nanoparticles are required to be monodisperse. However, commonly used batch reaction synthesis methods are afflicted with inherent drawbacks associated with inhomogeneous temperature and concentration distribution and insufficient mixing. Therefore, monodispersity cannot be guaranteed unless extra efforts are made in order to find synthesis parameters and protocols which yield monodispersed nanoparticles. Furthermore, a batch-wise operation is insufficient in terms of obtaining high product yield as batch reactor volumes are typically of a few milliliter only.

Microflow reactors are promissing alternatives for synthesizing nanoparticles in a controlled way [81]. Controllability and reproducibility originate from a high surface to volume ratio and efficient mixing when reactants merge in a microflow reactor. Furthermore, due to the small dimensions of the reactor, heat transfer is more efficient. Additionally, microflow reactors are able to produce constantly nanoparticles upon constant injection of reactants and flow. In this manner scale-up difficulties of batch-wise nanoparticle pro-

duction can be overcome by continuous microflow reactor operation. Further production scale-up can be realized by running several microflow reactors at the same synthesis conditions.

To ensure constant product quality, the nanoparticle production must be monitored in real time, i.e directly after the production. Fast monitoring can be achieved if no sample preparation is involved. This can be realized by an in-line integration of the nanoparticle characterization devices with the synthesis station. Small angle X-ray scattering (SAXS) and dynamic light scattering (DLS) are widely used for investigations of nanoparticle solutions [17]. The complementary use of both techniques enables to access a broad range of information on static and dynamic properties such as the mean size, size destribution, particle concentration, hydrodynamic size and the diffusion coefficient. Especially, using SAXS and DLS simultaneously and at the same sample position helps to correlate and compare measurement results of both techniques. The results obtained from SAXS and DLS measurements facilitate to assess the quality of the nanoparticles directly after the production.

Additionally, by the real-time monitoring of the nanoparticles it is possible to investigate the influence of synthesis conditions on nanoparticle properties such as size and size distribution. In this manner, for each nanoparticle size the corresponding synthesis conditions can be found. Synthesis parameters can be optimized to obtain a narrow size distribution. Thus, the nanoparticle production becomes flexible in terms of providing monodisperse nanoparticles of different sizes. The nanoparticle size can be changed simply by changing the synthesis conditions during production. This facilitates production of nanoparticles with a certain size on request.

In the investigation of the synthesis parameters based on the real-time monitoring concept, two aspects are involved which need to be attuned to each other. The first is the time-dependent variation of the nanoparticle properties. The second is the data collection and analysis to determine and track these changes. To be able to monitor fast changes of the properties, a fast extraction of the relevant nanoparticle parameters is required. Consequently, for effective optimization and investigation of the synthesis conditions, also an optimization of the characterization techniques is needed to achieve a short measurement time and fast analysis.

The presented thesis has three major tasks. The first task deals with an in-line integration of the SAXS and DLS devices to a microflow reactor synthesis station. For this purpose a flow-through capillary will be fabricated which will allow to characterize the nanoparticles directly after the synthesis. Moreover, the SAXS device will be optimized in terms of X-ray flux at the sample position to achieve a short exposure time. The DLS device will be integrated into the SAXS sample chamber for simultaneous SAXS and DLS measurements. The second task is concerned with the development of a concept for real-time monitoring of nanoparticle production. This involves software implementation for

automated and fast SAXS raw data processing. In the third task the developed concepts and optimized characterization devices will be validated by monitoring silica nanoparticles while ongoing production. The influence of different synthesis conditions on nanoparticle properties such as size and size distribution will be investigated.

The thesis is devided as following: In chapter 2 an overview on nanoparticle applications is given. State of the art synthesis methods for silica nanoparticles are introduced and discussed. The theoretical background of SAXS and DLS is introduced in chapter 3. Then, a description of the instruments is given in chapter 4. In chapter 5 the experimental setup comprising the microflow synthesis system and the flow-through capillary is introduced. Furthermore, silica nanoparticle production and the developed software for SAXS data processing is discussed. The results of synthesis experiments of silica nanoparticles are shown in chapter 6. The influence of different synthesis parameters on size and size distribution is investigated. Furthermore, the results of simultaneous SAXS and DLS measurements are discussed. In chapter 7 a summary and conclusions are presented. Finally, in chapter 8 an outlook is given.

Chapter 2

Overview

2.1 Nanoparticles

Nanoparticles represent the bridge between the bulk material and single atoms or molecules. Typically, bulk materials have constant physical properties regardless of the size. Whereas, nanoparticles may exhibit novel properties such as enhanced light absoption and luminescence [39, 51] and reactivity [74] depending on the nanoparticle size. Nanoparticles are defined as fine particles in the size range from 1 nm to 100 nm [2, 1]. The upper size limit is defined due to the fact that novel properties that distinguish nanoparticles from their bulk material counterparts emerge at a characteristic length scale below 100 nm [3]. Nanoparticles can be made of different materials such as:

- metals: Au, Ag, Fe
- semiconductors: CdTe, CdSe, Silizium
- oxides: SiO_2, TiO_2, ZnO, Al_2O_3, Fe_2O_3 or Fe_3O_4

In the next sections some nanoparticle types and their applications are described. As silica nanoparticles as sample system are investigated in this thesis, a detailed description of silica nanoparticles is followed. Finally, a summary of characterization methods is given.

2.1.1 Applications of nanoparticles

The properties mentioned above arise mainly from electron quantum confinement effects [70] and large surface-to-volume ratio [19]. Semiconductor nanoparticles of a size below 10 nm are referred to as quantum dots. Quantum dots show size and shape dependent fluorescence behaviour. This can be exploited for medical imaging or sensing applications. Furthermore, quantum dots are promissing candidates to be used in advanced optoelectronic devices such as LEDs [15], displays [42] or solar cells [69, 54]. Metal nanoparticles

can be applied for catalysis owing to the large active area resulting from the high surface-to-volume ration [19]. Additionally, metal nanoparticles exhibit size dependent interaction with light due to surface plasmon resonances. The resonance frequency can be adjusted by tuning the size and choice of dedicated molecules to attach to the nanoparticle surface or solvents [49]. Gold nanoparticles absorbing near infrared light can be applied for tumor treatment in the so called hyperthermia therapy [38]. Further medical applications involve drug delivery and imaging. Nanofluids, which are nanoparticles suspended in water, oil or glycols, are promissing candidates as advanced transport media or as electromagnetically-active media [71]. Si nanoparticles were applied to enhance performance of the anode in lithium-ion batteries [50]. Silica nanoparticles present an alternative for Cd based quantum dots in biomedical applications. Silica nanoparticles can be utilized for cancer cell imaging, single bacterium detection, DNA detection, separation and purification of biological molecules and cells and drug delivery [76, 79].

2.1.2 Silica nanoparticles

Most widely used synthesis methods of silica nanoparticles are reverse microemulsion, flame synthesis and sol-gel synthesis. In the reverse microemulsion method small water droplets in oil serve as small reactors [23]. This method provides highly monodisperse particles. The flame synthesis involves chemical vapor condensation which provides less controllability over size and particle shape [63]. The most widely used synthesis technique for silica nanoparticles is a sol-gel process based on the Stöber method [68]. It involves a hydrolysis reaction of tetraethylorthosilicate (TEOS) with water and condensation of the hydrolyzed TEOS monomers for particle formation and growth. Different modifications of the Stöber method are proposed which involve the use of different solvents such as ethanol and methanol [29, 48], synthesis under ultrasonication [64] and other modifications to tune the hydrolysis reaction speed [77, 78, 32]. With the modifications it was aimed to achieve a better reproducibility and controllability of the size of the nanoparticles. The reactions were performed in batch reactors and different synthesis parameters such as temperature, stirring, reactor volume and reactant concentrations were investigated [25, 26, 24]. It was found that the stirring rate and reactor volume has a tremendous impact on size, size distribution and final particle concentration. This results indicate that the formation of nanoparticles is highly sensitive on the mixing of the reactants. Additionally, semi-batch reaction experiments were performed to investigate the influence of slow continuous addition of TEOS on the size properties. The overall aims of the investigations are to establish reproducible synthesis routines to be able to synthezise monodisperse nanoparticles. Furthermore, the initial step of nucleation and further growth were investigated to predict the final particle size [13, 14, 29, 30, 66]. For this purpose different growth models such as the monomer addition model [52] and the aggregation model [12] were proposed.

A promissing mean to improve reproducibility and controllability of the size and size distribution is to utilize microflow reactors [81]. Many reports on microflow reactor synthesis of different nanoparticles exist. But there are only a few on silica synthesis [40, 31, 34, 75]. In all reports rather large ($> 100\,\mathrm{nm}$) particles were investigated. Furthermore, for microflow reactor based synthesis only few synthesis parameters are systematically investigated for the influence on size and size distribution.

In this work silica nanoparticles were used as sample system. On the one hand, silica nanoparticles are well investigated for batch and semi-batch reactions so that comparison with existing results facilitates the interpretation of the results obtained during the work of this thesis. On the other hand, it is aimed to extend knowledge about silica synthesis with microflow reactors.

2.1.3 Nanoparticle characterization

Typical nanoparticle properties of interest are the size, size distribution, shape and particle concentration. To determine the size, size distribution and shape commonly transmission electron microscopy (TEM) a scanning electron microscopy (SEM) are utilized. Additionally, light scattering techniques can also yield information on size, size distribution, shape and the particle number density, structure and particle interaction [17]. Small angle X-ray scattering (SAXS) and dynamic light scattering (DLS) are widely used as light scattering techniques. The advantage of light scattering techniques is that, apart from eventual delution, mostly no sample preparation is required. The nanoparticles remain in the solution. In contrary, the nanoparticle solution must dry for TEM and SEM measurements.

Besides, spectroscopic techniques such as XANES (X-ray absorption near edge spectroscopy) [61], NMR spectroscopy (nuclear magnetic resonance spectroscopy) [29, 30], UV-vis spectroscopy [80] or Raman spectroscopy [26] were applied in combination with SAXS. The combined and complementary use of individual characterization techniques facilitates to investigate growth kinetics and particle formation.

2.2 Microflow-reactors

Traditionally, batch reactors are used by chemists to carry out experiments. The volumes of the utilized flasks scale from a few milliliters to liters. The main drawbacks of batch reactors with large volumes are inhomogenous temperature and concentration distribution due to inefficient mixing of the reactants. Additionally, reactants can evaporate from the surface, again leading to inhomogene temperature distribution. This results in non uniform reaction processes. In consequence, this leads to less reproducibility and controllability [65]. To improve reproducibility and controllability the reactor volume must be decreased. However, this leads to scale-up problems in the attempt to establish a high

yielding production of nanoparticles with batch reactors.

One way to overcome those problems is to use microflow reactors. Microreactors are continuous flow reactors where the flow channel dimensions are typically in the sub-millimeter size regime (100 µm).

Mixing of fluid precursors is achieved at a connection of the channels. The mixture is then guided through an additional channel were the reaction is taking place. At a given volume of the reactor the flow speed can be adapted to the reaction time. Ideally, the outcome of the reactor is steady and uniform during the production time as long as the synthesis parameters remain unchanged. Thus, continuously operating microreactors are generally more productive and can help to circumvent the scale-up difficulties of batch reactors [81].

Owing to the small dimensions of the flow channels mass and heat trasport and surface phenomena due to higher surface-to-volume ratio are intensified. For instance, the surface-to-volume ratio of microreactors is $10000\,\mathrm{m^2/m^3}$ to $50000\,\mathrm{m^2/m^3}$, whereas for batch reactors it is typically $100\,\mathrm{m^2/m^3}$ [65]. This results in efficient and fast mixing of the reactans and heat is supplied or carried off faster from the reaction in the reactor.

Another advantage of microflow reactors is that synthesis parameters such as temperature, pressure, flow rates, ratio of reagents can be rapidly changed. Therefore, microreactors offer a tool for fast optimization of the reaction under investigation during flow.

2.3 Simultaneous SAXS and DLS measurements for real-time monitoring of nanoparticle production

Nanoparticle synthesis based on continuous microflow reactors allows to characterize the nanoparticles directly after the synthesis. This can be achieved by guiding the nanoparticle solution in a measurement cell. After the synthesis one is interested in a number of nanoparticle parameters such as size, size distribution, shape, particle number density and interactions. Furthermore, hydrodynamic radius and the diffusion coefficient are important parameters, e.g. for functionalized nanoparticles. To obtain these parameters SAXS and DLS are prevalent, because they are non-invasive and non-distructive. Thus, the nanoparticles can be probed directly inside the measurement cell after the synthesis without sample preparation.

On the one hand, SAXS is a static light scattering technique. In SAXS one measures the time-averaged intensity of the scattered X-rays as a function of the scattering angle. The intensity of the scattered X-rays is sensitive to the electron density contrast between the nanoparticles and the solvent. On the other hand, DLS is based on the temporal analysis of intensity fluctuations of the scattered light caused by the Brownian motion

of the suspended nanoparticles. It gives information on the dynamic properties of the nanoparticles, i.e. diffusion coefficient and average hydrodynamic radius. DLS allows average particle size measurements in a broad range from a few nanometers up to several microns. However, shape information are not easy to obtain. Therefore, a combined use yields broader range of information and more complete picture of the nanoparticle solution under investigation. Furthermore, utilizing both techniques simultaneously and at the same sample position helps to compare and correlate measurement results.

Combined use of SAXS and DLS was demonstrated in some reports [73, 72, 21]. However, the measurements were not performed simultaneously. This is due to the fact that in state-of-the-art DLS devices a cuvette, stationary inside the device, must be filled with the nanoparticle solution. The cuvette is not accessible for the X-ray beam for SAXS measurements. Moreover, real-time monitoring with those DLS devices is hardly practicable. Therefore, in this work a novel DLS device is used where no stationary cuvette is involved. DLS measurements can be performed outside the DLS device.

The aim of the work described in this thesis is to apply SAXS and DLS simultaneously and at the same sample position and perform real-time monitoring of nanoparticle production. In this way trends and correlations between nanoparticle properties and synthesis conditions can be examined. Based on this, forecasts can be made for other synthesis conditions.

Chapter 3

Theoretical Background

By means of light scattering techniques different properties of nanoparticles can be examined. In this work two different techniques are used to characterize the nanoparticles under investigation. The first is small angle X-ray scattering (SAXS), which is used to obtain information on size, size distribution and particle concentration. The second technique is dynamic light scattering (DLS) which is mainly used to determine the hydrodynamic size. The hydrodynamic size is a measure for diffusive properties of the nanoparticles. As both techniques base on the same light scattering principles, in the first section a general theoretical background for light scattering is given. In the second section SAXS is introduced. In the third section the basics of DLS are presented.

3.1 Basics of light scattering from discrete scatterers

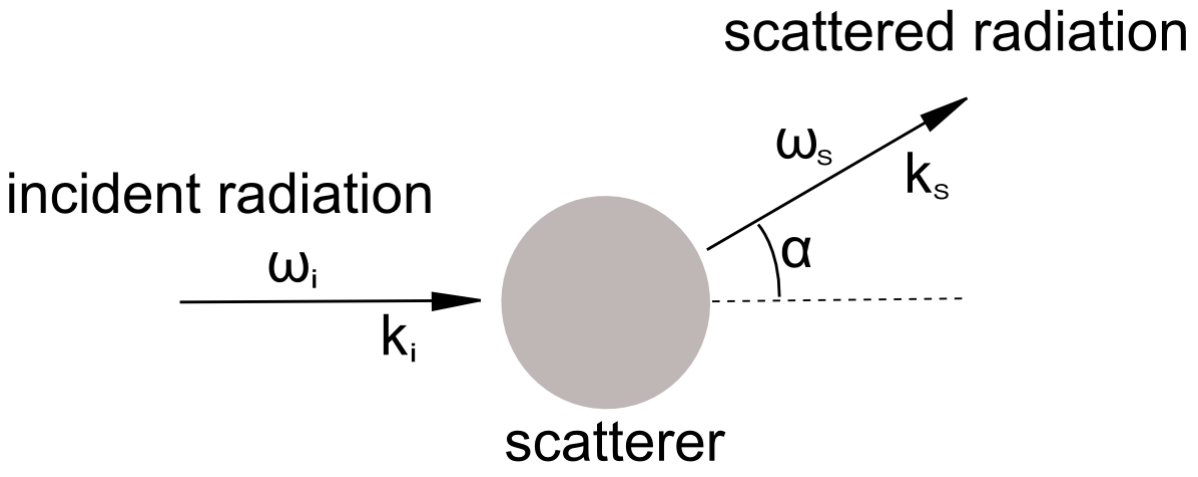

Figure 3.1: Schematics of scattering of radiation from a scatterer.

In Figure 3.1 a schematic illustration of light scattering from a scatterers is shown. The incident light field is characterized by the wavevector $\mathbf{k}_i$ with the magnitude $k_i = |\mathbf{k}_i| = \frac{2\pi}{\lambda_i}$ and angular frequency ω_i. The scattered light has the wavevector $\mathbf{k}_s$ with the magnitude $k_s = |\mathbf{k}_s| = \frac{2\pi}{\lambda_s}$ and angular frequency ω_s. The incident wave is assumed to be a plane

wave:

$$E_i(\mathbf{r}) = \exp\left(i\mathbf{k}_i \cdot \mathbf{r}\right). \tag{3.1}$$

In the following inelastic scattering shall be neglected. This leads to $k = k_i = k_s$ and $\omega = \omega_i = \omega_s$. The so called scattering vector and its magnitude can be writen as

$$\mathbf{q} = \mathbf{k}_s - \mathbf{k}_i \quad \text{and} \quad q = |\mathbf{q}| = \frac{4\pi}{\lambda}\sin\left(\alpha/2\right) \tag{3.2}$$

in the case of elastic scattering [67].

Starting with the wave equation

$$\nabla^2 E(\mathbf{r}) + k^2 n^2(\mathbf{r}) E(\mathbf{r}) = 0 \tag{3.3}$$

and the assumption that the electric field is the sum of the incident and the scattered field $E(\mathbf{r}) = E_i(\mathbf{r}) + E_s(\mathbf{r})$ the electric field of the scattered wave at point $\mathbf{r}$ can be given as

$$E_s(\mathbf{r}) = \int_V F(\mathbf{r}')E(\mathbf{r}')\frac{\exp\left(ik|\mathbf{r}' - \mathbf{r}'|\right)}{|\mathbf{r} - \mathbf{r}'|}d\mathbf{r}', \tag{3.4}$$

with the so called scattering potential

$$F(\mathbf{r}) = \frac{1}{4\pi}k^2(n^2(\mathbf{r}) - 1) \tag{3.5}$$

and the refraction index $n(\mathbf{r})$ [10]. The integration is performed over the volume of the

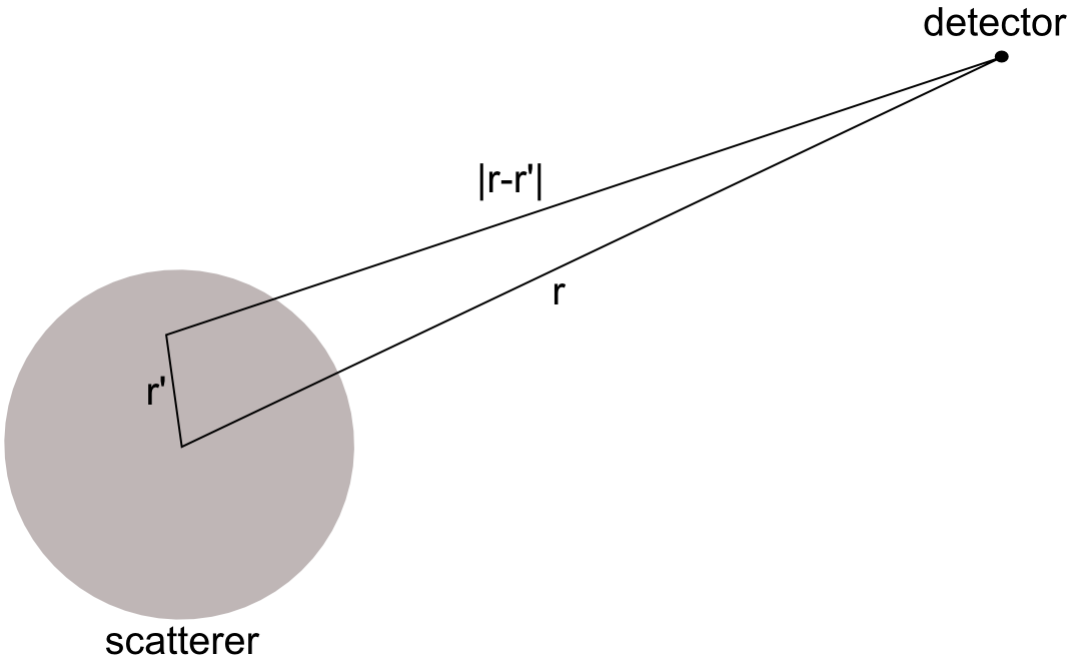

Figure 3.2: Notation of the position vectors.

scatterer. By adding the incoming wave on both sides of the equation leads to

$$E(\mathbf{r}) = \exp\left(i\mathbf{k}_i \cdot \mathbf{r}\right) + \int_V F(\mathbf{r}')E(\mathbf{r}')\frac{\exp\left(ik|\mathbf{r} - \mathbf{r}'|\right)}{|\mathbf{r} - \mathbf{r}'|}d\mathbf{r}'. \tag{3.6}$$

This integral equation can be solved by iteration where the solution $E(\mathbf{r})^{(i)}$ after the ith iteration step is obtained by iserting the previous solution $E(\mathbf{r})^{(i-1)}$. For the initial step $E(\mathbf{r})^{(0)} = E_i(\mathbf{r}) = \exp(i\mathbf{k}_i \cdot \mathbf{r})$ is assumed. If the scattering can be considered as weak so that a light wave is scattered only once, the electric field inside the volume is dominated by the incident field. Therefore, for weak scatterers the iteration can be terminated after the first iteration step. This is referred to as Born approximation. The scattered wave can then be approximated as

$$E_s(\mathbf{r}) = E(\mathbf{r})^{(1)} - \exp(i\mathbf{k}_i \cdot \mathbf{r}) = \int_V F(\mathbf{r}') \exp(i\mathbf{k}_i \cdot \mathbf{r}) \frac{\exp(ik|\mathbf{r} - \mathbf{r}'|)}{|\mathbf{r} - \mathbf{r}'|} d\mathbf{r}' \,. \tag{3.7}$$

A further assumption is that the scatterer is far away from the detection point $\mathbf{r}$. This leads to the far-field approximation. The resulting scattered wave is a spherical wave originating from the discrete scatterer [10]:

$$E_s(r) = f(\mathbf{q}) \frac{\exp(ikr)}{r} \quad \text{with} \quad f(\mathbf{q}) = \int_V F(\mathbf{r}) \exp(-i\mathbf{q}\mathbf{r}') d\mathbf{r}' \,. \tag{3.8}$$

The quantity $f(\mathbf{q})$ is referred to as the scattering amplitude. In the next step, scattering from an assembly of N discrete scatterers is examined. The scatterers may be positioned at locations $\mathbf{R}_j$. The resulting scattered wave is the sum of all scattering contributions and is given as

$$E_s(r) = \frac{\exp(ikr)}{r} \sum_{j=1}^{N} f_j(\mathbf{q}) \exp(i\mathbf{q} \cdot \mathbf{R}_j) \tag{3.9}$$

with the phase factor $\exp(i\mathbf{q} \cdot \mathbf{R}_j)$ [6].

In this thesis X-rays (at $\lambda = 1.34\,\text{Å}$ corresponding to the Ga-K_α line) and red laser light ($\lambda = 658\,\text{nm}$) is applied to characterize nanoparticles in a solution. In the following, equation 3.9 is discussed for the X-ray and the optical wavelength regime. Due to the small wavelength of the X-ray radiation, electrons are considered as independent scatterers. Therefore, the integration in equation 3.8 is performed over the volume of an atom. Consequently, equation 3.9 describes scattering from an assembly of atoms and $\mathbf{R}_j$ are referred to positions of the atom inside a nanoparticle.

In the energy regime of hard X-ray radiation ($\hbar\omega \approx 10\,\text{keV}$) the electrons inside the scatterer are considered to be free as the energy of the X-ray beam is higher then all transition frequencies of the elements involved in this thesis (Si, O, N, C). This gives rise to the fact that the refraction index in the X-ray regime is less than unity and can be writen as

$$n = 1 - \delta \quad \text{with} \quad \delta = \frac{2\pi\rho r_0}{k^2} \,, \tag{3.10}$$

where ρ is the electron density and r_0 is the electron radius or also referred as Thomson scattering length [6]. The quantity δ is on the order of 10^{-5}. Thus, the deviation from

unity is very small. With the approximation $n^2 = 1 - 2\delta$ the scattering amplitude can be writen as

$$f(\mathbf{q}) = -\frac{1}{2\pi}k^2\delta \int_V \exp\left(-i\mathbf{q}\mathbf{r}^{'}\right)d\mathbf{r}^{'} = -\rho r_0 \int_V \exp\left(-i\mathbf{q}\mathbf{r}^{'}\right)d\mathbf{r}^{'}\,. \tag{3.11}$$

Concludingly, the scattering strength depends on the electron density of the particle.

In the optical wavelength regime refraction effects must be taken into account. The equivalent to the Born approximation is the Rayleigh-Gans-Debye approximation and can be represented by the following condition [28]:

$$\frac{4\pi a}{\lambda}(m-1) << 1\,, \tag{3.12}$$

where a is the radius of the scatterer and $m = \frac{n_P}{n_S}$ the ratio between the refractive index of the particle and the solvent. This condition is fulfilled if $n_P \approx n_S$ and the particle is much smaller then the wavelength. For particles which are smaller than the wavelength scattering can be described by Rayleigh scattering. The electrons inside the particle are subject to a homogenous electric field. Therefore, the particle can be considered as an individual dipole emitting a secondary wave. In the far-field approximation the emitted wave is a spherical wave. The Rayleigh intensity of the scattered light is $I_s \propto a^6\lambda^{-4}$.

Consequently, in the optical wavelength regime and for small scatterers compared to the wavelength, equation 3.8 describes scattering from a particle, whereas equation 3.9 the from a particle solution were the discrete scatterers are the particles.

The Rayleigh-Gans-Debye approximation fails if the particles are larger then the wavelength or if the incident wave is refracted at the boundary between the particle and the solvent. Instead, Mie theory must be applied [28]. In Mie theory the field strength variation inside the particle and refraction on the boundary must be taken into account.

In dynamic light scattering the nanoparticles change their position due to Brownian motion [62]. Therefore, their position vectors are time dependent $\mathbf{R}_j(t)$. The intensity of the scattered light from a particle assembly is given as the mean square of the scattered electric field. Consequently, the intensity is also time dependent and it follows

$$I_s(t) \propto \sum_{i,j=1}^{N} \exp\left(i\mathbf{q}\cdot(\mathbf{R}_i(t)) - \mathbf{R}_j(t))\right). \tag{3.13}$$

The intensity fluctuation can be measured to extract the size of the nanoparticles.

3.2 Small Angle X-ray Scattering

SAXS is one among the various applications of X-ray radiation to characterize materials. In most applications one is interested in the scattered intensity as a function of the scattering angle to obtain structural information such as lattice type or atomic distances. At a wavelength on the order of $\lambda = 0.1\,\mathrm{nm}$, this involves measuring the scattered X-rays

at angles of several degrees. These techniques are referred to as wide angle X-ray scattering (WAXS). In contrary, in SAXS one is interested in investigation of larger lengths scales such as the size of nanoparticles or proteins in the nanometer size range. Due to the larger sizes compared to inter-atomic distances the scattered intensity is measured at smaller scattering angles, which gives the technique its name.

3.2.1 Differential scattering cross-section

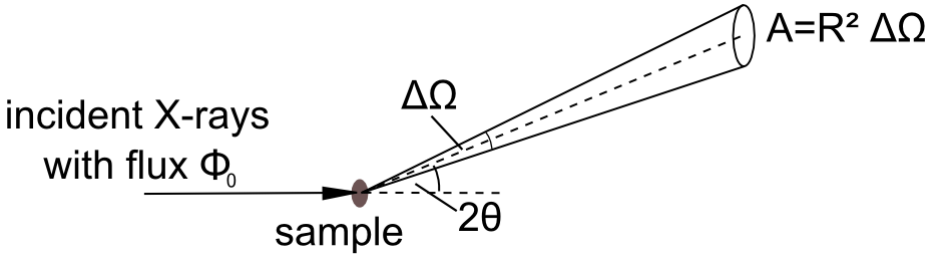

Figure 3.3: Notations and schematics illustration of a scattering experiment to derive the differential scattering cross-section.

Figure 3.3 illustrates schematicaly a scattering experiment where the sample is irradiated with an X-ray beam having flux Φ_0 (number of photons per unit time and unit area). X-rays are scattered at a scattering angle of 2θ in a solid angle of $\Delta\Omega$. The X-rays are then detected in an area of size $A = R^2\Delta\Omega$, where R is the distance to the sample. Only elastic scattering is examined. In such an experiment one is interested in the intensity I_s of the scattered X-ray beam as a function of the scattering vector. The differential scattering cross-section is defined as

$$\frac{d\sigma}{d\Omega} = \frac{I_s}{\Phi_0 \Delta\Omega} = \frac{|E_s|^2 R^2}{|E_i|^2}\,, \tag{3.14}$$

where in the last step $I_s = R^2\Delta\Omega c|E_s|^2/\hbar\omega$ and $\Phi_0 = c|E_i|^2/\hbar\omega$ [6]. If the sample is a free electron both the classic and quantum mechanic picture lead to the same expression for the differential scattering cross section

$$\frac{d\sigma}{d\Omega} = r_0^2 \tag{3.15}$$

where

$$r_0 = \frac{e^2}{4\pi\epsilon_0 mc^2} = 2.82 \cdot 10^{-5}\,\text{Å} \tag{3.16}$$

is the so called Thomson scattering length with e and m being the charge and mass of an electron and ϵ_0 and c the permittivity and speed of light in vacuum [6].

3.2.2 X-ray scattering from an atom

Scattering from many electrons can be discribed as the sum of the contributions from each electron. The resulting quantity is then referred to as scattering amplitude and is

given as

$$A(\mathbf{q}) = -r_0 \sum_j e^{i\mathbf{q}\cdot\mathbf{r}_j}\,, \tag{3.17}$$

where $\mathbf{r}_j$ is the position of an electron with index j with respect to a reference electron at the origin [6]. The minus sign accounts for the phase shift of π of the wave scattered by an electron.

One can consider an atom as being a cloud of free electrons spatialy distributed according to a number distribution function $\rho(\mathbf{r})$. Thus, a volume element $d\mathbf{r}$ at $\mathbf{r}$ contributes an amount of $r_0\rho(\mathbf{r})d\mathbf{r}$ to the scattering amplitude. Furthermore, a photon scattered from $d\mathbf{r}$ at $\mathbf{r}$ has a phase shift of $\mathbf{q}\cdot\mathbf{r}$ with respect to the photon scattered at the origin $\mathbf{r} = 0$. Thus, the total scattering amplitude for an atom can be written as the summation of all contributions multiplied by the Thomson scattering length

$$A(\mathbf{q}) = -r_0 \cdot \int \rho(\mathbf{r}) e^{i\mathbf{q}\cdot\mathbf{r}} d\mathbf{r} = -r_0 \cdot f^0(\mathbf{q})\,. \tag{3.18}$$

$f^0(\mathbf{q})$ is refered to as the form factor of the atom [6]. It is a measure of the scattering strength of the atom and is the Fourier transform of the distribution function. For $q \to 0$ the form factor tends to Z which is the electron number of the atom. For $q \to \infty$ it tends to zero. From quantum mechanics it is known that electrons are bound at certain energy levels in the atom. Consequently, if the energy of the incident X-ray doesn't exceed the binding energy of e.g. the tightest bond electrons (in the K-shell) then these electrons cannot be considered as free and thus don't contribute to the scattering. This effect is accounted for by an additive term $f^{'}(\hbar\omega)$ which is negative and reduces the scattering strength of an atom. Furthermore, if the energy matches a binding energy or is slightly above, the X-ray photon is absorbed rather then scattered. This is accounted for by an imaginary quantity $if^{''}(\hbar\omega)$.

3.2.3 X-ray scattering from an assembly of atoms

Individual atoms are assumed as discrete scatterers. Consequently, the scattered electric field from an atom can be given by equation 3.9. Inserting equation 3.1 and 3.9 in equation 3.14 yields the differential scattering cross-section

$$\frac{d\sigma}{d\Omega} = \left| \sum_j f_j(\mathbf{q}) e^{i\mathbf{q}\cdot\mathbf{R}_j} \right|^2\,, \tag{3.19}$$

where $f_j(\mathbf{q})$ represents the form factor of the atom with index j and position $\mathbf{R}_j$. Further, by introducing the scattering length density function $\beta(\mathbf{R})$ one can obtain a continuum generalization of the scattering cross-section

$$\frac{d\sigma}{d\Omega} = \left| \int \beta(\mathbf{R}) e^{i\mathbf{q}\cdot\mathbf{R}} d\mathbf{R} \right|^2\,. \tag{3.20}$$

The scattering length density means that in a volume $d\mathbf{R}$ at $\mathbf{R}$ a point source with the form factor $f(\mathbf{q}) = \beta(\mathbf{R})d\mathbf{R}$ is located [67].

3.2.4 X-ray scattering at small angles

According to equation 3.2 small scattering angles are associated with small q-values which are in turn reciprocally related to the real space dimensions. The latter is due to the fact that in equation 3.20 the differential scattering cross-section is given by the Fourier transform of the scattering length density. Real space dimensions can be approximated by $a = \frac{2\pi}{q}$. Or for a sphere with diameter $a = 1000\,\text{Å} = 100\,\text{nm}$ the corresponding q-value is estimated to be $q = 0.0063\,\text{Å}^{-1}$. The resulting scattering angle is $2\theta = 0.076\,^\circ$ with $\lambda = 1.34\,\text{Å}$. From the experimental point of view it is a challenging task to reach such small angles. For larger structures the scattering angle gets even smaller. Consequently, it is commonly agreed that roughly 100 nm is the upper size limit to be measured with SAXS. This size regime is around two orders of magnitude larger than a typical bond length of some Ångström. Thus, SAXS can be considered as a low resolution probe technique for structure analysis, but which is capable of providing a view of the overall assembly of atoms: by measuring the scattered intensity which is proportional to the differential scattering cross-section one can determine the morphology, i.e. size and shape, of the scattering object.

Typical samples to be investigated with SAXS are particles or proteins suspended in a solvent. In this case the scattering length density of the solvent must also be taken into account and the scattering length distribution can be writen as

$$\hat{\beta}(\mathbf{R}) = \begin{cases} \beta(\mathbf{R}) - \beta_0 & \text{if } \mathbf{R} \text{ inside solute} \\ 0 & \text{if } \mathbf{R} \text{ in the solvent} \end{cases} , \tag{3.21}$$

where β_0 is the scattering length density of the solvent [67]. Additionally, for the sake of simplicity a constant scattering length density inside the particle is assumed: $\beta(\mathbf{R}) = \beta_1$. In reality the X-ray beam irradiating the sample has a finite size. The X-ray beam and the sample define a scattering volume V, where the included particles number is N. The particles are assumed to have the same sze and shape. The detected scattered intensity is the sum over all particle contributions. To account for this the differential cross section is multiplied by the particle number density $n = \frac{N}{V}$. The scattering cross-section is then given as

$$\frac{d\sigma}{d\Omega} = n \left| (\beta_1 - \beta_0) \int_{V_P} e^{i\mathbf{q}\cdot\mathbf{R}} d\mathbf{R} \right|^2 . \tag{3.22}$$

Introducing the so called particle form factor

$$F(\mathbf{q}) = \left| \int_{V_P} e^{i\mathbf{q}\cdot\mathbf{R}} d\mathbf{R} \right|^2 \tag{3.23}$$

yields the differential scattering cross section as

$$\frac{d\sigma}{d\Omega} = n\Delta\beta^2 F(\mathbf{q}) , \tag{3.24}$$

where $\Delta\beta = \beta_1 - \beta_0$ is the scattering length density contrast between the particle and the solvent. The integration in the particle form factor is performed over the volume of the particle V_P [67].

For spherical particles with radius R the integral from equation 3.23 can be written as [67]:

$$4\pi \int_0^R r^2 \frac{\sin(qr)}{qr} dr = 4\pi \frac{\sin(qR) - qR\cos(qR)}{q^3} \tag{3.25}$$

Consequently, the differential scattering cross section reads as

$$\frac{d\sigma}{d\Omega} = n\Delta\beta^2 V_P^2 F(q,R)\,, \tag{3.26}$$

with the particle volume $V_P = 4/3\pi R^3$ and the form factor is

$$F(q) = \left| 3\left[\frac{\sin(qR) - qR\cos(qR)}{q^3 R^3} \right] \right|^2 . \tag{3.27}$$

In a suspension particles have a size distribution of a certain width. This can be accounted for by a distribution function $D(R)$ which represents the size distribution of the particles. Accordingly, the differential scattering cross-section reads as [59]

$$\frac{d\sigma}{d\Omega} = n\Delta\beta \int_0^\infty F(q,R) D(R) V(R)^2 dR\,. \tag{3.28}$$

To demonstrate the influence of the size distribution, the differential scattering cross-section were calculated numerically according to equation 3.28. The results are illustrated in Figure 3.4.

In this work as size distribution function the Schulz-Zimm function is used, which is given as

$$D(R) = AR^\alpha e^{-\gamma R} \quad \text{with} \quad A = \gamma^{1+\alpha}/\Gamma(1+\alpha) \quad \text{and} \quad \Gamma(x) = \int_0^\infty t^{x-1} e^{-t} dt, \tag{3.29}$$

The mean radius R_m and the standard deviation σ_R are related to the parameters α and γ via

$$R_m = \frac{1+\alpha}{\gamma} \quad \text{and} \quad \text{and} \quad \sigma_R = \frac{1+\alpha}{\gamma^2}\,. \tag{3.30}$$

For the Schulz-Zimm size distribution the integral in equation 3.28 can be solved explicitly. The explicit solution of the integral is given in [44]. In this way the integral can be solved without numerical integration which ensures a short computation time and fast extraction of the mean radius and the standard size distribution from the measured curve.

In a SAXS experiment the measured scattered intensity as function of the modulus of the scattering vector is proportional to the differential scattering cross-section and is given as

$$I_{exp}(q) = \Phi_0 \eta(\lambda) T(\lambda) \frac{d\sigma}{d\Omega} \Delta\Omega + B(q)\,, \tag{3.31}$$

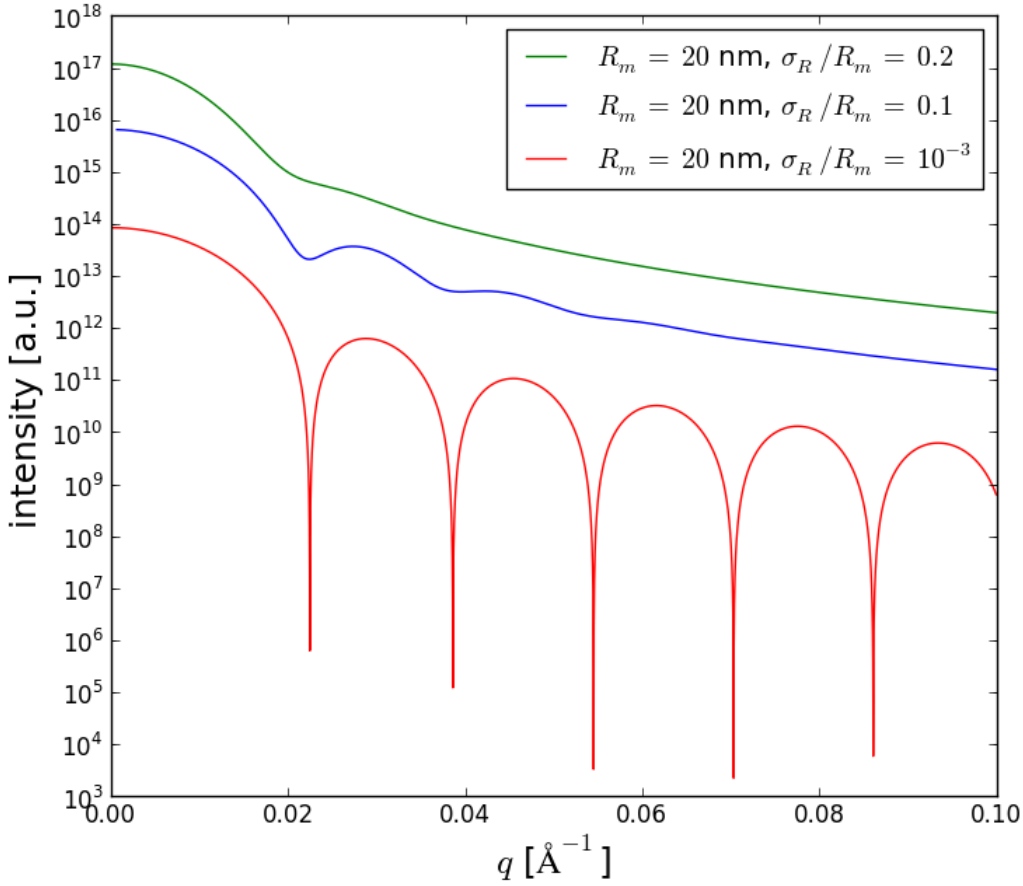

Figure 3.4: Calculated differential scattering cross-section for different widths of the Schulz-Zimm size distribution function. With increasing width the fringes get gradualy smeared.

where η and T denote the detector efficiency and the transmission of the sample, respectively. Both depend on the wavelength λ of the incident X-ray beam. Furthermore, $B(q)$ is a background signal arising from the scattering of the solvent in which the particles are suspended. The information about size and shape are encoded in the differential scattering cross section or in the integral from equation 3.28. Therefore, after subtracting the background the measured intensity is considered as

$$I_{exp}(q, R_m, \sigma_R) = const. \cdot \int_0^\infty F(q, R) D(R, R_m, \sigma_R) V(R)^2 dR \,. \tag{3.32}$$

3.3 Dynamic Light Scattering

In DLS a monochromatic light beam, such as a laser, is irradiating a solution with particles. The particles are in Brownian motion, which causes a Doppler shift of the scattered light. Due to interference of the scattered light waves from different particles, the detected intensity fluctuates in time. An auto-correlation function can be computed from the recorded intensity as function of time. The fluctuation depends on the size of the particles. This makes it possible to extract the size from the auto-correlation function.

3.3.1 Brownian motion and the hydrodynamic radius

Brownian motion of the particles suspended in a solution is caused by collisions due to thermal motion of the solvent molecules. These collisions cause a random motion of the particles.

The diffusion of the particles can be discribed by the diffusion equation

$$\frac{\partial}{\partial t}p(\mathbf{r},t) = D\nabla^2 p(\mathbf{r},t)\,, \tag{3.33}$$

where $p(\mathbf{r},t)$ can be interpreted as the particle concentration at point $\mathbf{r}$ and time t [10]. The diffusion coefficient can be written as

$$D = \frac{k_B T}{\zeta}\,, \tag{3.34}$$

where k_B is the Botzmann constant, T is the temperature and ζ is the friction constant. According to the Stokes approximation the friction constant is $\zeta = 6\pi\eta R_H$, where η is the viscosity of the solvent and R_H is the so called hydrodynamic radius. Concludingly, the hydrodynamic radius is given by the Stokes-Einstein relation:

$$R_H = \frac{k_B T}{6\pi\eta D}\,. \tag{3.35}$$

The hydrodynamic radius discribes the radius of a hard sphere that has the same translational diffusion speed as the particle under investigation [62]. The translational diffusion of the particles depends not only on its "core" size but also on the surface structure. Furthermore, the particle shape and ionic concentration in the solvent influence the diffusion of the particle. Modifying these factors in a way that affects the diffusion will change the apparent hydrodynamic size. For example, functionalysing the particle surface with polimers will decrease diffusion speed of the particle. Consequently, the particle appears to be larger and the hydrodynamic size will increase.

3.3.2 The auto-correlation function

There are to ways to obtain information on the dynamics of the scatterers under investigation. In the first case spectral analysis is utilized to obtain the spectrum (scattered intensity vs. frequency ω) [10]. The frequency shift of a wave scattered at a particle moving with velocity $\mathbf{v}$ is given as $\Delta\omega = \mathbf{q}\cdot\mathbf{v}$. As the detected scattering intensity is the mean square of the sum of all scattered waves from all particles the detected spectrum exhibits a peak at ω_i with a certain width. The broadening of the peak results from the fact that the scattering particles are moving randomly in all directions and their velocity is distributed according to the Maxwell-Boltzmann distribution. This leads to different $\Delta\omega$ values. The FWHM of the peak can be related to the diffusion coefficient $\Delta\omega_{1/2} = Dq^2$.

Alternatively, the diffusion coefficient can be determined by means of DLS. In DLS the intensity of the scattered light is measured resolved in time. The intensity fluctuates

due to the Brownian motion of the scattering particles. From the recorded intensity the auto-correlation function can be calculated according to

$$\langle I(0)I(\tau)\rangle = \lim_{T_{meas}\to 0} \frac{1}{T_{meas}} \int_0^{T_{meas}} I(t)I(t+\tau)dt\,, \tag{3.36}$$

were T_{meas} is the measurement time [10]. The normalized intensity auto-correlation function is defined as

$$g^2(\tau) = \frac{\langle I(0)I(\tau)\rangle}{\langle I(0)^2\rangle}\,. \tag{3.37}$$

To derive a relationship between the diffusion coefficient and the intensity auto-correlation function the electric field auto-correlation function is defined and given as

$$g^1(\tau) = \frac{< E(0)E(\tau) >}{< E(0)^2 >}\,. \tag{3.38}$$

According to equation 3.9 the electic field at a point detector is $E(t) \propto \sum_{i=1}^{N} \exp\left(-i\mathbf{q}\cdot\mathbf{R}_i(t)\right)$. Inserting it into equation 3.38 and 3.37 yields [10]:

$$\begin{aligned} g^1(\tau) &= N^{-1} \sum_{i,j=1}^{N} \langle \exp\left(-i\mathbf{q}\cdot(\mathbf{R}_i(0) - \mathbf{R}_j(\tau))\right)\rangle \\ &= N^{-1} \sum_{j} \langle \exp\left(-i\mathbf{q}\cdot(\mathbf{R}_j(0) - \mathbf{R}_j(\tau))\right)\rangle \\ &= \langle \exp\left(-i\mathbf{q}\cdot(\mathbf{R}(0) - \mathbf{R}(\tau))\right)\rangle \qquad (3.39) \\ & \qquad (3.40) \end{aligned}$$

In the intermediate step it is assumed that for a delute (non-interacting) particle suspension terms with $i \neq j$ are zero since the particles are considered as statistically independent. In the same manner the intensity auto correlation function can be calculated:

$$g^2(\tau) = 1 + \left|\langle \exp\left(-i\mathbf{q}\cdot(\mathbf{R}(0) - \mathbf{R}(\tau))\right)\rangle\right|^2 \tag{3.41}$$

Combining both equations results in the Siegert relation [62]:

$$g^2(\tau) = 1 + |g^1(\tau)|^2\,. \tag{3.42}$$

The summation is performed over all particles. It can be replaced by a time average. This is possible for an ergodic system where a particle can reach each point in the phase space. The field auto-correlation function can then be writen as

$$g^1(\tau) = \int_0^{\infty} \exp\left[i\mathbf{q}\cdot\mathbf{R}\right] p(\mathbf{R},\tau) d\mathbf{R} \tag{3.43}$$

where the integration is performed over all possible displacements $\mathbf{R} = \mathbf{r}(\tau) - \mathbf{r}(0)$ of a particle and $p(\mathbf{R},\tau)$ is a probability distribution which describes the probability that a

particle experiences a displacement $\mathbf{R}$ in time τ [10]. It can be shown that the electrical field auto-correlation function can be writen as:

$$g^1(\tau) = \exp(-Dq^2\tau)\,. \tag{3.44}$$

For monomodal (monodisperse in size and shape) particle solutions the diffusion coefficient can be determined by fitting an exponential function to the measured intensity auto-correlation curve according to

$$g^2(\tau) = 1 + \exp(-2Dq^2\tau)\,. \tag{3.45}$$

For a polydisperse particle solution the field auto-correlation function is assumed to be composed of a sum of several exponential decay functions

$$g^1(\tau) = \sum_n A_n \exp\left(-\Gamma_n \tau\right), \tag{3.46}$$

where A_n is the intensity-weighted contribution to the overall and $\Gamma_n = D_n q^2$ is the decay constant [8, 10]. Each decay constant corresponds to a hydrodynamic radius.

Chapter 4

Instruments

4.1 Bruker AXS NanoSTAR™

4.1.1 Design and components of the NanoSTAR

Desing of the NanoSTAR

The Nanostar is an instrument for 2-dimensional SAXS developed by Bruker AXS. The basic layout of the NanoSTAR is illustrated in Figure 4.1. The X-rays are generated in the X-ray source. Then, an X-ray optics monochromatize and focuses or collimates the X-rays. Subsequently, the beam passes through a pinhole system and illuminates the sample. Finally, the scattered X-rays are detected by a 2D area detector. Additionally, a beam stop is mounted close before the detector to prevent the detector from being exposed to the direct beam. The NanoSTAR can be equipped with different types of

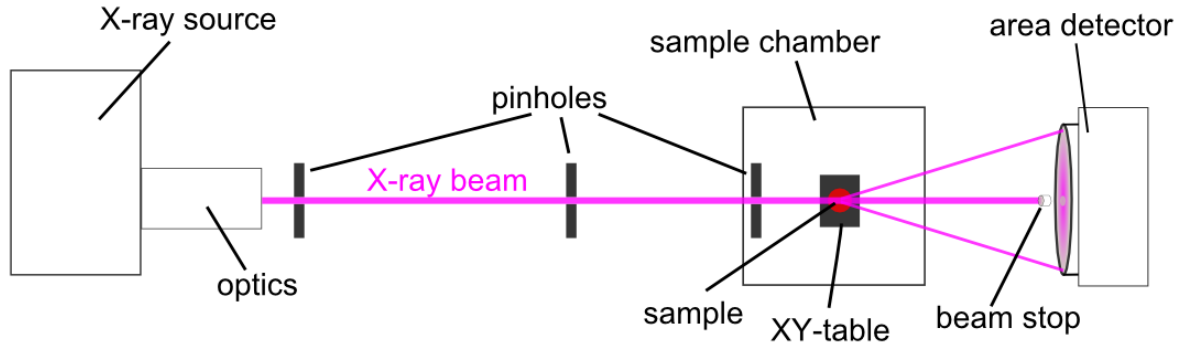

Figure 4.1: Schematic illustration of a Nanostar.

X-ray sources and optics. In particular, in Figure 4.2 the NanoSTAR used in this work is shown. It is equipped with a MetalJet X-ray source and a MONTEL optics. The pinholes are mounted into the pinhole mounts, which are connected via tubes (1. and 2. primary tubes). The third pinhole is located inside the sample chamber. As detector a VÅNTEC-2000™ 2D X-ray detector is used, which is also connected via tubes (1. and 2. secondary tubes) to the sample chamber. This NanoSTAR is located at KU Leuven

at the department for physics and astromony. Detailed descriptions of the components of

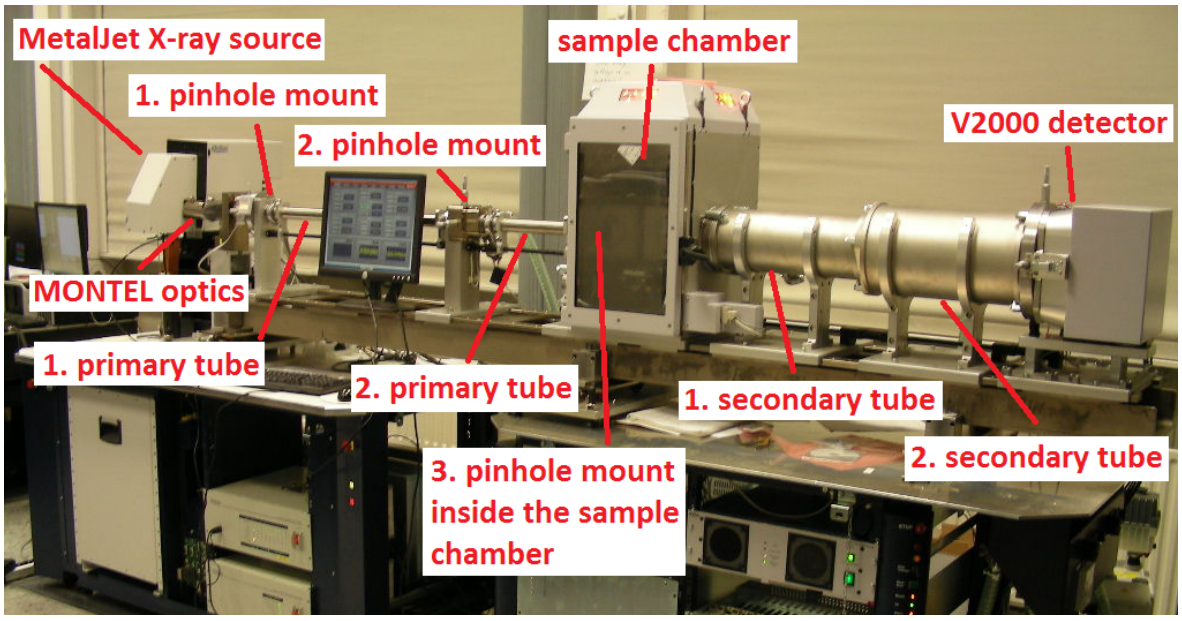

Figure 4.2: NanoSTAR equipped with a MetalJet Xray source, MONTEL X-ray optics and a VÅNTEC-2000 detector.

the NanoSTAR are given in the following sections.

X-ray sources

There is a choice of micro-focus (IμS), high-brilliance rotating anode (RAG), and Metaljet X-ray sources available for the Nanostar. The figure of merit for an X-ray source is the electron power density on the anode. The power density is defined as the electron power devided by the electron spot size on the anode. The spot size determines the system performance in terms of achievable flux density and divergence of the X-ray beam. Heat dissipation from the anode must be optimized to maximize the power density.

In Table 4.1 all X-ray sources and the corresponding quantities such as power, electron spot size and resulting electron power density load on the anode are summarized. The IμS

X-ray source	power [W]	electron spot size on anode [μm^2]	electron power density load on anode [kW/mm^2]
IμS	50	150 × 30	11
RAG	2500	1000 × 100	25
MetalJet	200	80 × 20	125

Table 4.1: Comparative summary of operation power and electron spot sizes for different X-ray sources utilized on a NanoSTAR.

is a sealed tube with a conventional stationary solid metal anode, but with a considerably

smaller electron focus compared to standard sealed tube sources.[1] To reach a small spot size of a few tens of micrometers the electron power must be decreased. Nevertheless, with the IμS a higher power density can be reached compared to the standard sealed tube source. In RAG sources the electron power can be increased while preserving a small electron spot. Therefore, the power density load can be increased considerably.

With the MetalJet X-ray source an even higher power density can be reached. The anode material of the MetalJet is an alloy of gallium and indium which is liquid at room temperature so that it can be conditioned as a jet. This allowes for a further increase of the power density. In section 4.2 a detailed description of the MetalJet X-ray source is given.

X-ray optics

The purpose of the optics is to condition the beam in terms of divergence, beam size and spectral purity. A simple mean to produce a monochromatic X-ray beam is to utilize a crystal monochromator and the Bragg law $\lambda = 2d\sin(\theta)$ [6].[2] With a given lattice constant d (or also referred as d-spacing) and diffraction angle θ only X-rays of a defined wavelength λ are diffracted. In practice, the beam is not perfectly monochromatic and the energy spectrum exhibits a certain bandwidth. The bandwidth of a crystal is given by its Darwin width [6]. Typically, crystal monochromators have a narrow bandwidth of $\Delta E/E \approx 10^{-4}$ [9]. However, the drawback of a crystal monochromator is the low intensity of the diffracted beam due to the low throughput of the narrow bandpass.

As an alternative multilayer mirrors can be used to monochromatize the beam. The basic functionality is the same as for the crystal monochromator. The difference is that alternating layers of a heavy material, such as tungsten, and light material, such as carbon, take over the role of the atomic lattice of the crystal monochromator. The heavy material acts as a reflector whereas the light material is a spacer. Each pair of both materials is referred to as bilayer. The thickness of a bilayer is the d-spacing of the mirror. At the boundary between the heavy and the light material a part of the X-ray beam is reflected and the other part is transmitted. In turn, the transmitted part is partly reflected at the next boundary. If the Bragg condition is fulfilled the reflected waves are added up in phase resulting in an intense monochromatic X-ray beam. Reflectivity values of up to 95 % can be reached. The d-spacing is larger compared to atomic lattice constants of crystal monochromators, typically in the range of 3 - 5 nm [37]. Therefore, θ is only of the order of a few degrees. As the number of layers is much lower then diffraction planes in a crystal the bandwidth of a multilayer mirror is wider compared to crystal monochromators, typically $\Delta E/E \approx 10^{-2}$ [9].

[1] Typical standard sealed tubes operate with 8000-15000 × 200-500 μm^2 spot size at 1000 - 4000 W power.

[2] Here the first diffraction order $n = 1$ is considered

Commonly used mirror shapes are parabolic for collimation and elliptic for focusing. The working principle of curved mirrors is illustrated in Figure 4.3. The X-ray source is situated at the parabola focus or is located in one focus of the ellipse. Additionally, for a curved mirror the d-spacing needs to be graded accordingly in X-ray beam direction because the angle of incidence θ varies along the length of the mirror. In this way the Bragg condition is fulfilled for the selected wavelength at each point along the mirror.

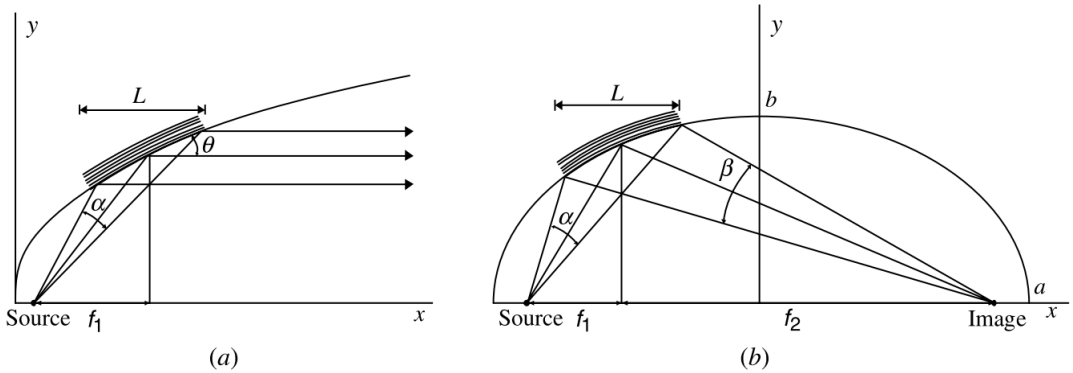

Figure 4.3: Schematic illustration of the working principle of a parabolic (a) and elliptic (b) multilayer mirror. Taken from [33].

A single curved mirror conditions the beam only in one plane. Therefore, a second mirror is added and aligned perpendicular to the first one to achieve conditioning in two planes perpendicular to each other. There are two possibilities to align the mirrors as illustrated in Figure 4.4. In the first cross-coupled or Kirkpatrick-Baez configuration [43] the second mirror is mounted after the first mirror. This configuration has the disadvantage that the second mirror further away from the source captures a smaller angle if assuming both mirrors to be of the same length. Furthermore, as the mirrors have different focal lengths their magnification is different. This leads to different divergences and focal sizes in two planes. To overcome these issues a side-by-side configuration of the two mirrors was proposed M. Montel [53]. Therefore, optics with the side-by-side mirror configuration are also referred to as MONTEL optics. The two mirrors are identical and have the same focal lengths, distance to the source and capture angle. In this mirror configuration the X-ray beam is reflected twice to be collimated or focused in both directions. The double reflected beam is utilized to irradiate the sample. However, there are also beams reflected only once by one of the two mirrors. Additionally, there is also some residual white beam contribution. The single reflected and the white beam can be masked out by a pinhole.

X-ray beam conditioning with pinholes

As the double reflected X-ray beam has the most possible intensity it would be favourable to use the double reflected beam to irradiate the sample. However, in praxis further beam conditioning is required to adjust the size of the beam as not alway a dedicated optics

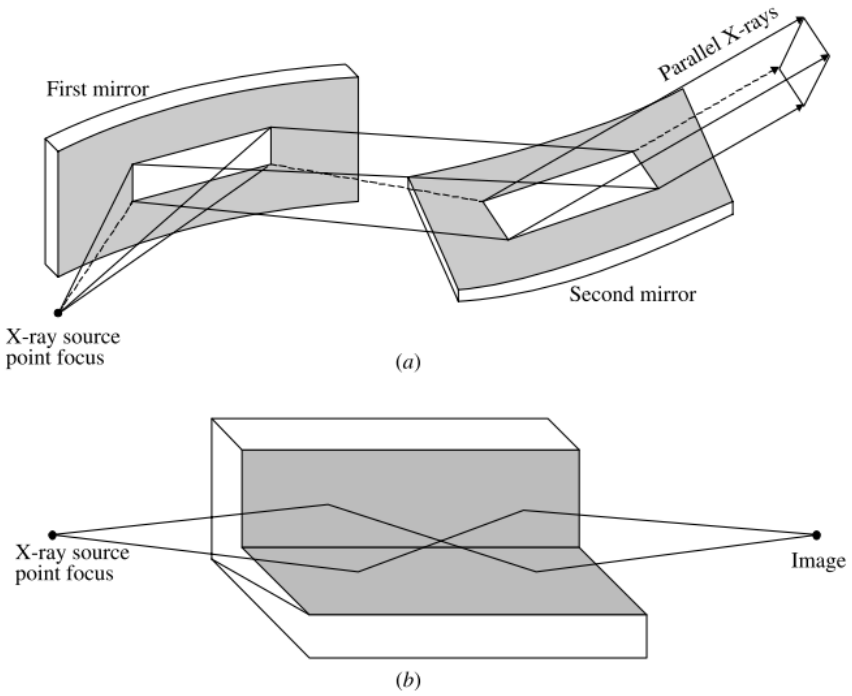

Figure 4.4: Schematic illustration of two multilayer mirrors in the cross-coupled configuration (a) and the side-by-side configuration (b). Taken from [33].

is available providing the desired beam size. Furthermore, the double reflected beam can be distorted due to abberations arising from imperfections of the optics. In Figure 4.5 scattering around the beam stop is shown without and with pinholes. The measurements were performed without sample. The beam stop blocked the double reflected beam. The X-ray around the beam stop are detected by the detector. Without pinholes significant parasitic scattering is observable which is attributed to optics imperfections. Prior to perform sample measurements the parasitic scattering must be removed. After inserting the pinholes the parasitic scattering is blocked, only a corona close to the beam stop is remaining. Typically, it can be neglected when small scattering vectors close to the beam stop are not of interest or if the samples generate a strong scattering signal.

The pinhole setup utilized for the NanoSTAR was developed by J. S. Pedersen [58]. The resulting pinhole system contains three pinholes with different radii R_i and different distances L_i illustrated in Figure 4.6. The first pinhole blocks the single reflected beams. The second pinhole determines the beam size at sample and detector position. Finally, the third pinhole acts as a guard pinhole which cuts the parasitic edge scattering from the second pinhole. The size of the third pinhole must be carefully chosen as it should not cut into the beam defined by the first and second pinholes. On the other hand, if the diameter is too large the parasitic scattering can pass through the pinhole. The used pinhole radii and distances are summarized in Table 4.2. The distance L_3 can be varied by adjusting the detector position with the aid of the secondary tubes which have a length of 400 mm. For maximal distance ($L_3 = 1155\,\text{mm}$) both secondary tubes are used. In the middle

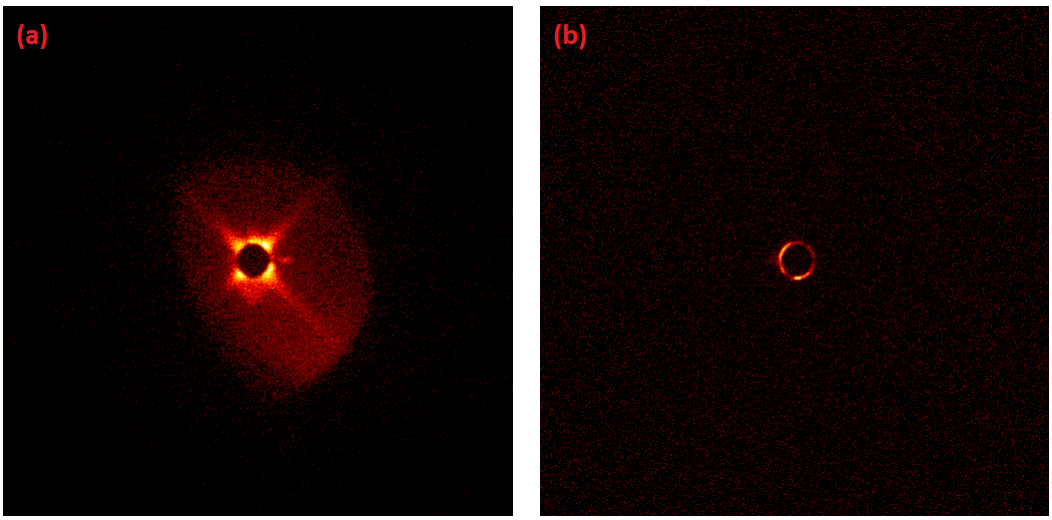

Figure 4.5: Comparison of the parasitic scattering around the beam stop (a) without pinholes and (b) with the standard pinhole setup.

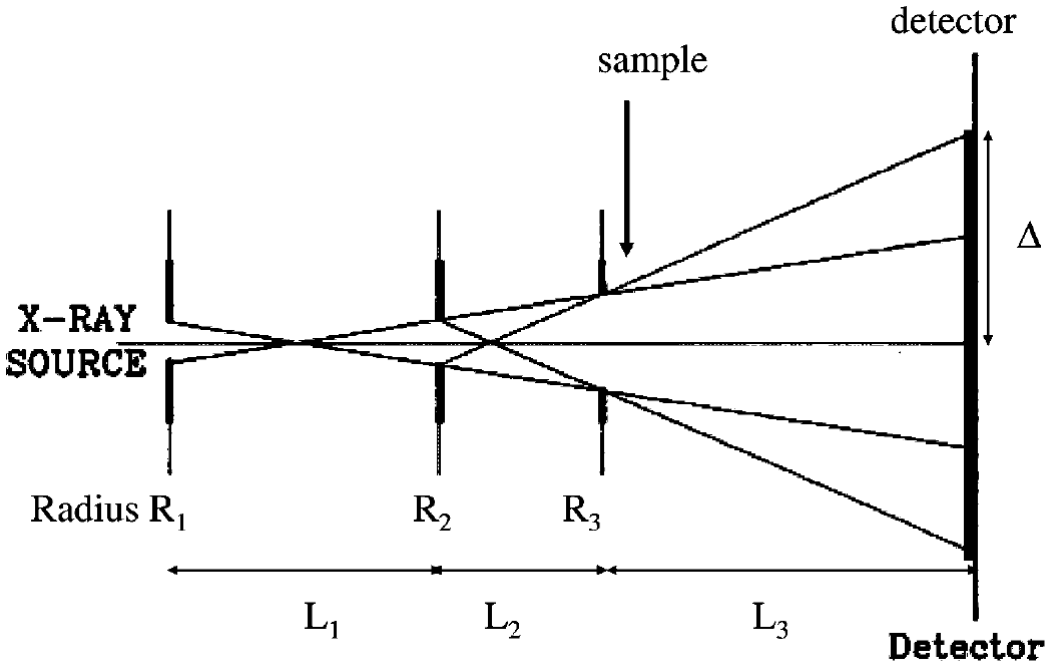

Figure 4.6: Schematic illustration of the X-ream beam conditioning system consisting of 3 pinoles. Modified from [58].

R_1	R_2	R_3
375 µm	225 µm	500 µm
L_1	L_2	L_3
925 mm	485 mm	variable

Table 4.2: Summary of the pinhole radii and distances. The distance between the third pinhole and detector is not fixed but can be varied.

position ($L_3 = 755\,\text{mm}$) one tube is removed. At the shortest distance ($L_3 = 355\,\text{mm}$) both tubes are removed. For each distance a beam stop with an adjusted diameter 2Δ is available (2.04 mm, 3.1 mm, 4.2 mm). In this work largely the middle detector position was used.

The beam stop defines a minimal accessible scattering vector. In the middle position the 3.1 mm beam stop is used. The minimal scattering vector can be determined as $q_{min} = 0.011\,\text{Å}^{-1}$. With the aid of the minimal scattering vector a maximal detectable length $D_{max} = \frac{2\pi}{q_{min}} \approx 570\,\text{Å}$=57 nm can be estimated. It is interpreted as the maximal diameter of a particle which can be detected with the used pinhole and beam stop system.

This concept with three pinholes is referred to as the standard pinhole setup in the following of this thesis. The standard setup is used by Bruker AXS for all NanoSTAR versions irrespective which X-ray tube or optics type is utilized.

NanoSTAR sample chamber

The interior of the NanoSTAR sample chamber is shown in Figure 4.7. The sample chamber includes the pinhole mount for the third pinhole and the motorized XY-table, on which a sample can be mounted. With the aid of the XY-table the sample can be positioned in the X-ray beam. Furthermore, a reference sample arm is situated inside the chamber. Reference samples such as glassy carbon can be mounted on the arm and positioned in the X-ray beam if needed. With the glassy carbon (GC) the transmission T_{sample} of a sample can be determined by positioning the glassy carbon behind the sample. The recorded scattered intensity $I_{sample+GC}$ is then related to the scattered intensity without the sample I_{GC} [33]: $T_{sample} = \frac{I_{sample+GC} - T_{GC} I_{sample}}{I_{GC} - T_{GC} I_0}$, where T_{GC} is the transmission of the GC, I_{sample} is the scattered intensity from the sample without GC and I_0 is a measurement without sample and GC. For measurements the sample chamber, the primary and the secondary tubes are evacuated down to a pressure of typically $2 \cdot 10^{-2}$ mbar.

VÅNTEC-2000 2D X-ray detector

The VÅNTEC-2000 (V2000) is an two-dimensional detector based on the 'MicroGap$^{\text{TM}}$' technology. MicroGap is an improvement of the multiwire proportional chamber (MWPC) concept to obtain higher global (counts s^{-1}) and local (counts $\text{s}^{-1}\,\text{mm}^{-2}$) count rates. The MWPC is a gas filled detector consisting of multiwire grid electrodes. An incoming X-ray photon initiates a charge avalanche by ionizing gas atoms. The maximum count rate is limited by the charge drift to the electrodes, or more exactly, the ion collection time, which depends on the distance between the electrodes, the applied voltage, gas mixture and gas pressure. To reduce the ion collection time, the distance between electrodes can be decreased and the acceleration voltage increased. However, this leads to electrical sparks and discharge.

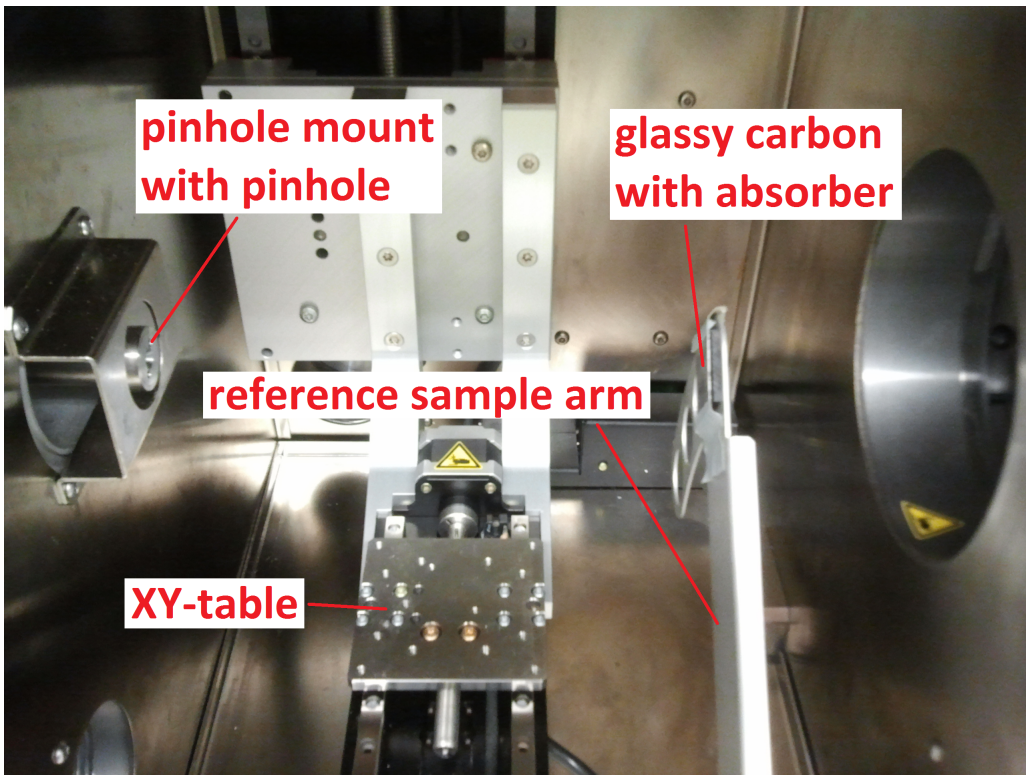

Figure 4.7: Interior of the Nanostar sample chamber. Inside the sample the third pinhole mount, the XY-table for sample mounting and the reference sample arm are located.

In Figure 4.8 a schematic illustration of the MicroGap working principle is shown. After ionization of a gas atom an electron is freed which drifts to the grid. The avalanche process is initiated only in the amplification gap. The amplification gap width is choosen to be very small (about 2 mm) to decrease the ion collection time. The electrons are collected by an anode, which is made of a resistive layer on a ceramic substrat to prevent discharges and extend the life time of the anode. Beneath the substrat, read-out stripes detect the induced charge. The V2000 detector shows linear behaviour for up to a local and global count rate of 2400 cps/pixel and 0.9 Mcps, respectively [4].

The V2000 detector has an active area of 14 cm × 14 cm. In this work the detector was placed in the middle detector position ($L_3 = 755$ mm). In this configuration the maximal accessible scattering angle is $2\theta = 5°$, corresponding to a maximal scattering vector of $q_{max} = 0.4\,\text{Å}^{-1}$.

4.1.2 X-ray beam conditioning with SCATEX pinholes

In the standard pinhole system of the NanoSTAR the third guard pinhole is inevitable to block the edge scattering of the second pinhole. However, the guard pinhole blocks only a part of the parasitic scattering from the second pinhole. A part of the parasitic scattering passes through the third pinhole. The beam stop must be increased to block the parasitic scattering as illustrated in Figure 4.9. Therefore, it is desirable to diminish parasitic

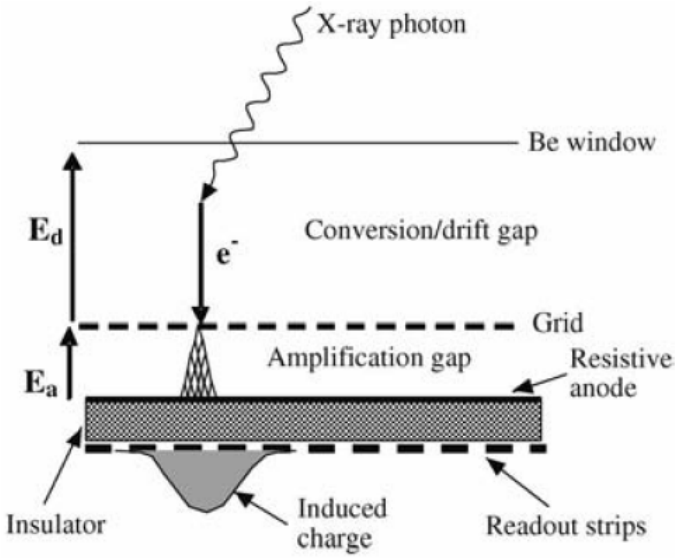

Figure 4.8: Schematic illustration of the MicroGap principle. Taken from [33].

scattering. For this purpose SCATEX pinholes (from incoatec GmbH) can be utilized, which exhibit considerably reduced edge scattering. With SCATEX pinholes X-ray beam conditioning, the third guard pinhole becomes obsolet. Furthermore, the beam stop size can be reduced to reduce the minimal scattering vector. Alternatively, to increase X-ray flux the SCATEX pinhole size can be increased compared to the standard pinholes while maintaining the beam stop size.

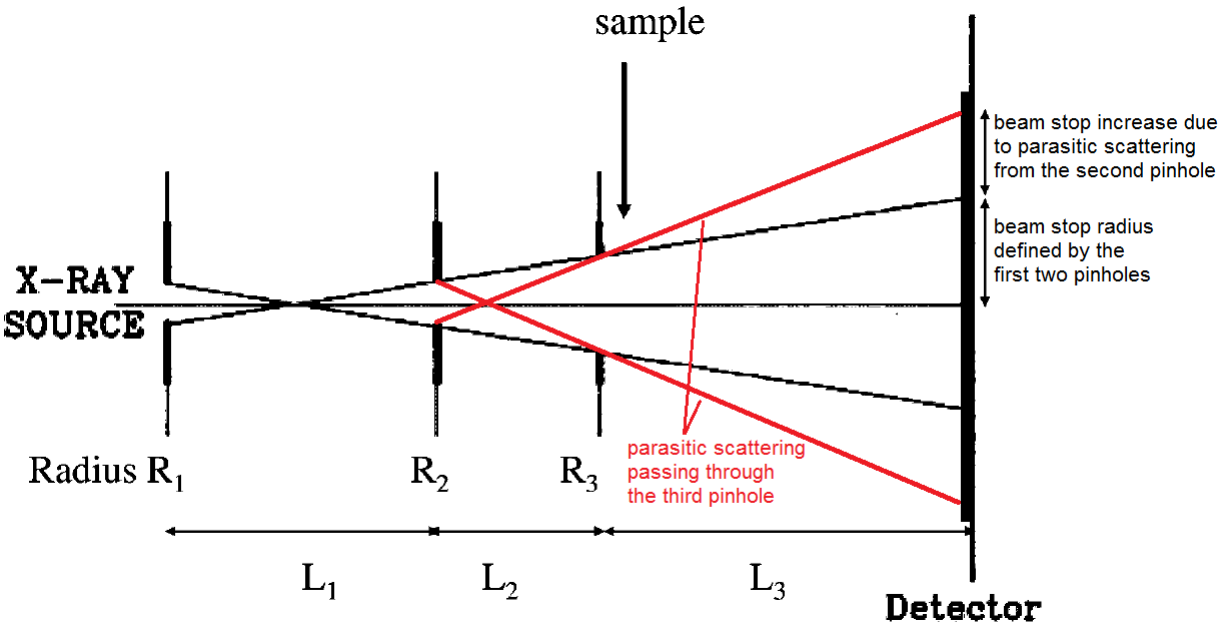

Figure 4.9: Schematic illustration of the X-ream beam conditioning system consisting of 3 pinoles. The beam stop must be increased due to parasitic scattering passing through the third guard pinhole. Modified from [58].

As conditions changed through the availability of the multilayer MONTEL optics, SCATEX pinholes and the MetalJet X-ray source the pinhole conditioning concept must

be reconsidered to take advantage of the novel technologies and increase the X-ray flux at sample position. Especially owing to the small electron foot print on the metal jet target and according to Liouville's theorem in equation 4.2 the focus size is also expected to be small. In turn, a small beam size results in larger flux density at the focus and by choosing pinholes with the right diameter one can maximize the flux through the pinholes. The beam size at the sample position and at the detector are also strongly affected by the beam size and divergence and the choice of the pinholes. In most SAXS applications rather large (around 1 mm in diameter) beam sizes are desirable to irradiate a sample volume of sufficient size. For example when diluted particle suspesions or protein solutions with low scattering length density contrast are investigated. Typically, the liquid samples are injected into a capillary. Therefore, to minimize parasitic scattering from the capillary walls the beam size should not exceed capillary diameters of typically 2 mm. Furthermore, the beam size dictates the size of the beam stop and thus the minimal accessible scattering vector q_{min}. Conclusively, in finding the optimal SCATEX pinholes these constraints must be taken into account.

A set of SCATEX pinholes with diameters of 300 µm, 550 µm and 720 µm and beam stops with diameters of 2.04 mm, 3.1 mm, 4.2 mm were available. To determine the best pinhole and beam stop combination, the double reflected beam must be investigated in terms of convergence/divergence and position and size of the focus. These quantities were determined by measuring the X-ray beam size after the optics as function of the distance with respect to the optics exit window.[3] The resulting beam size as function of the distance is shown in Figure 4.10. At short distances the beam is converging towards its focus point after which it diverges again. The location of the focus point can be estimated by fitting linear functions to the converging and diverging part of the curve. The corresponding fitting results for the slopes m_{conv} and m_{div} of the converging and diverging line and the corresponding intercept values b_{conv} and b_{div} are:

$$\begin{aligned} m_{conv} &= (-0.68 \pm 0.08) \cdot 10^{-3} \\ b_{conv} &= (0.53 \pm 0.03)\,\text{mm} \\ m_{div} &= (0.88 \pm 0.06) \cdot 10^{-3} \\ b_{div} &= (-0.34 \pm 0.05)\,\text{mm} \end{aligned}$$

The crossing point of the linear functions is then assumed to represent the location of the focus. The size of the focus is approximately 150 μm (FWHM).

The slopes of the linear functions correspond to the convergence and divergence angle $\tan^{-1}(m_{conv}) = 0.68\,\text{mrad}$ and $\tan^{-1}(m_{div}) = 0.88\,\text{mrad}$. According to the specifications of the used MONTEL mirror the convergence/divergence angle is given as 1 mrad. This

[3] The size measurements were performed with the aid of a beam measurement pin-diode kit. The pin-diode kit is calibrated by the german authority PTB (Physikalisch-Technische Bundesanstalt)

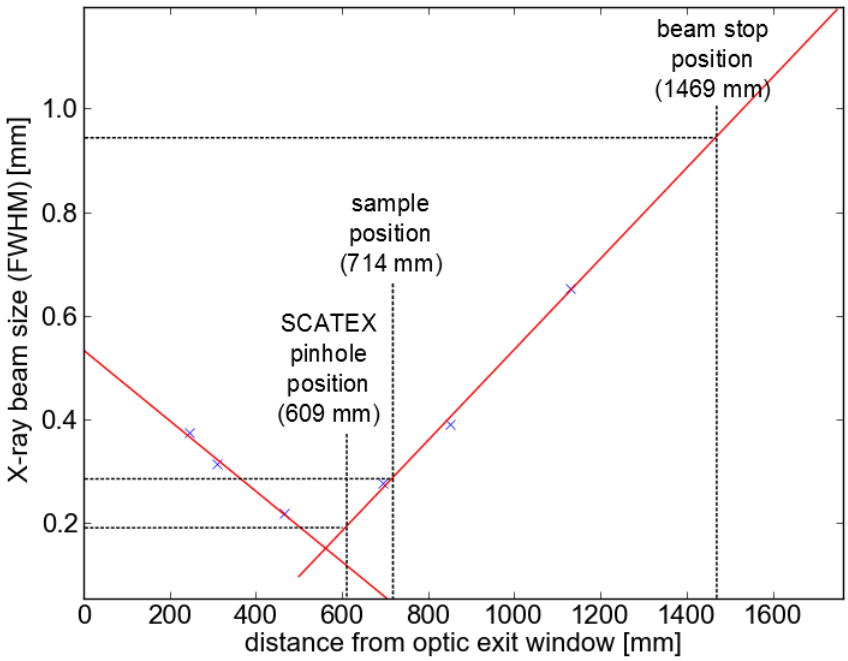

Figure 4.10: X-ray beam size as function of the distance from the optic exit window.

value is beyond the error intervals of the measured values. Additionally, the measured values deviate with respect to each other. This can be attributed to uncertainties in measuring the distance to the optics.

As the SCATEX pinholes exhibit negligible parasitic edge scattering, the third guard pinhole such as in the standard pinhole setup becomes obsolet. Therefore, the SCATEX pinhole can be placed directly before the sample. The simplest way to mount the pinhole is to place it in the sample chamber on the pinhole mount which was originally intended for the third guard pinhole of the standard pinhole setup. The second pinhole mount dedicated for the second standard pinhole was removed.

When choosing the pinhole position and diameter, for maximal flux at sample position it is desired to preserve as much as possible of the double reflected beam. This is achieved if the pinhole diameter matches the width of the beam. There are possible ways to fit the diameter to the X-ray beam. First, at a given pinhole diameter the position of the pinhole along the beam can be adjusted. Secondly, at a given position the pinhole diameter can be fitted to the beam width. In this work the first approach is chosen as a fixed set of three pinholes with different diameters was given. The distribution of the intensity of the beam in the cross section is assumed to have a gaussian shape. This facilitates to approximate the width of the beam to be $w_{beam} \approx 6\sigma$, where $\sigma = \frac{\mathrm{FWHM}}{2\sqrt{(2\ln(2))}}$.[4] The pinhole positions is chosen so that with the corresponding FWHM from Figure 4.10 the beam width matches pinhole diameter $d_{ph} \approx 6\sigma$. The resulting positions are summarized in table 4.3. For example, the 550µm pinhole must be placed in a distance of 636 mm from the optics exit to let through the double recflected beam. According to this procedere no

[4]It is assumed that the range from -3σ to $+3\sigma$ corresponds to 99.7% of the beam intensity.

position for the 300 µm pinhole can be found as it is too small, even in the focus.

d_{ph}	FWHM [µm]	pinhole position [mm]
300	117	—
550	216	636
720	283	712

Table 4.3: Estimated beam size at sample position and beam stop position for different diameters of a SCATEX pinhole.

To tune the distance between the optics exit and the pinhole the two primary tubes can be used (see Figure 4.2). With the short tube (2. primary tube) a pinhole position of 609 mm can be adjusted. This position is around 3 cm off from the estimated position for the 550 µm pinhole. With the long tube (1. primary tube) a pinhole position of 1049 mm is achievable. This position is far away from the estimated positions. Therefore, the short tube was used. The resulting primary beam path of the NanoSTAR is shown in Figure 4.11. The pinhole was mounted inside the sample chamber into the 3. pinhole mount at a distance of 609 mm from the optics.

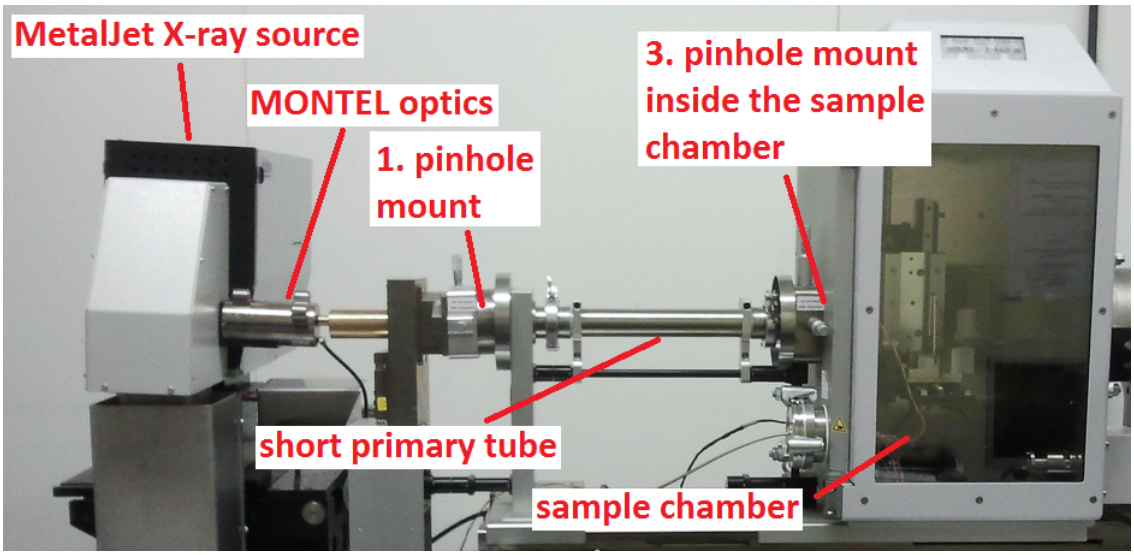

Figure 4.11: Illustration of the resulting primary side of the MetalJet-NanoSTAR after removing the middle pinhole mount and shifting the sample chamber closer to the optics. The SCATEX pinhole is situated in the third pinhole mount inside the sample chamber

With the fitted linear function which represents the diverging beam section the beam width at sample position (714 mm) and beam stop position (1469 mm) can be estimated. The resulting beam width values are summarized in Table 4.4.

A set of beam stop sizes was available with the following diameters: 2.04 mm, 3.1 mm, 4.2 mm. The 2.04 mm and 3.1 mm beam stop were inserted sequentially and a 'blanck' measurement (SAXS frame without sample) was measured for each beam stop size. The

beam size at d_{ph} [µm]	beam size at sample position [mm]	beam size at beam stop position [mm]
550	0.73 ± 0.17	2.48 ± 0.26

Table 4.4: Estimated beam size at sample position and beam stop position for different diameters of a SCATEX pinhole.

frames are shown in Figure 4.12. The 2.04 mm beam stop turn out to be small to block the full direct beam, whereas the 3.1 mm beam stop is sufficient and is larger then the estimated beam size.

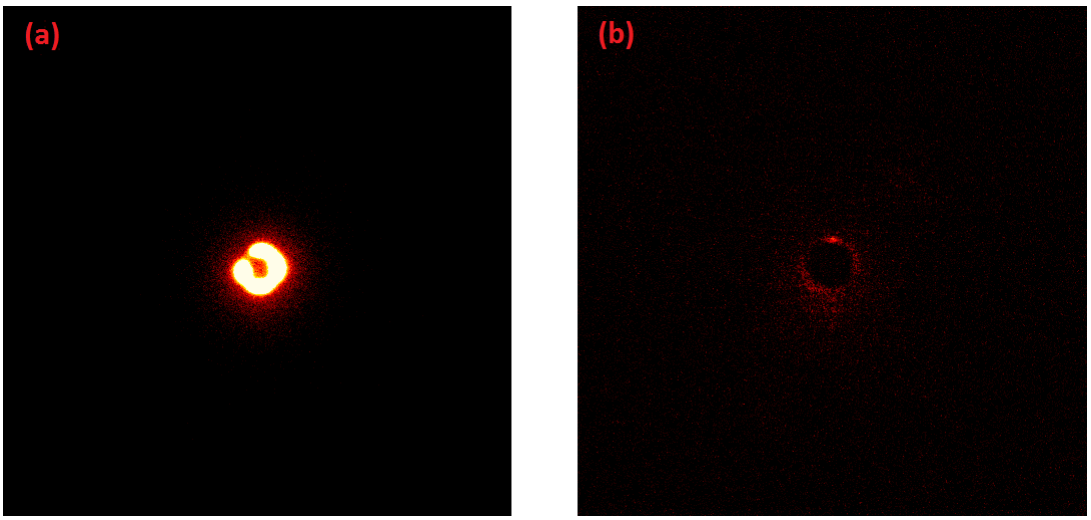

Figure 4.12: Blank measurement with a 550 µm SCATEX pinhole and a beam stop with a diameter of 2.04 mm (a) and 3.1 mm (b).

Concludingly, with the 550 µm pinhole at a position of 609 mm a 3.1 beam stop can be used to block the entire direct beam. A bit of parasitic scattering is still present around the beam stop.

Additionally, a pinhole setup consisting of two pinholes was investigated to decrease the parasitic scattering even further. Thereby, an additional SCATEX pinhole was placed into the first pinhole mount (see Figure 4.11). The resulting distance between the pinholes is 535 mm. As additional pinhole a 550 µm and a 720 µm SCATEX pinholes were testen. In Figure 4.13 a blanck measurement with two 550 µm pinholes is shown, which shows less parasitic scattering around the beam stop.

The single SCATEX pinhole setup and the double SCATEX pinhole setup resulted in an flux increase compared to the standard pinhole setup. The flux increase factors are summarized in Table 4.5. As a conclusion, using SCATEX pinholes under the limiting conditions of given pinhole diameters and given primary tubes the flux at sample position was increased by at least a factor of 2.25. Additionally, the same minimal q-value as in the standard pinhole setup of around $q_{min} = 0.011\,\text{Å}^{-1}$ was preserved. In this work for

real-time monitoring experiments the double pinhole setup with the 720 µm was used.

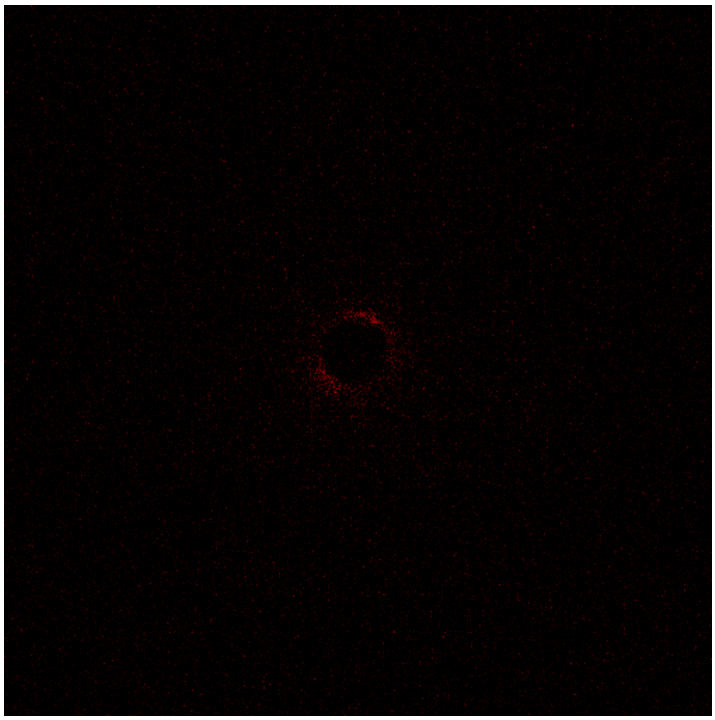

Figure 4.13: Measurement of the beam with 3.1 mm beam stop with a pinhole setup consisting of two 550 µm pinholes.

pinhole setup	flux increase factor
single pinhole 550 µm	3.6
550 µm + 550 µm	2.25
720 µm + 550 µm	2.75

Table 4.5: Flux increase factors with respect to the standard pinhole setup.

4.2 MetalJet, a liquid target X-ray source

4.2.1 Preliminary considerations

In laboratory X-ray sources, X-ray generation is achieved by bombarding a target with electrons. The generated X-rays are composed of the so called bremsstrahlung and characteristic emission lines of the target material. In contrary to synchrotron radiation sources where the beam is inherently well collimated, owing to the forward emitting characteristics of an undulator or a wiggler, X-rays are emitted largely in 4π of solid angle upon electron bombarding. Therefore, to achieve X-ray beam collimation or focusing a dedicated X-ray optics must be utilized. To assess the combined performance of the X-ray source and the

optics the brilliance B is introduced. A common definition is [6]:

$$B = \frac{\text{number of photons per second}}{A_1 \cdot \Omega_1 \cdot (0.1\%\ \text{bandwidth})}\,. \tag{4.1}$$

Here, A_1 is the source size and Ω_1 is the solid angle covered by the optics. After reflection the X-ray beam has a divergence of Ω_2 and the image size is A_2.

Liouville's theorem [7] states that the phase-space volume containing the X-ray photons is constant in time:

$$A_1\Omega_1 = A_2\Omega_2\,. \tag{4.2}$$

In other words, the number of photons at A_1 is the same as at A_2 and at each cross section everywhere along the beam. Therefore, the flux (photons s^{-1}) behind the optics can be given as $F = BA_2\Omega_2$. For most X-ray diffraction applications high X-ray flux density is desired as the beam may further be conditioned with slits or pinholes. Furthermore, a small divergence is useful for high resolution applications. To obtain high flux at small beam size and divergence a high brilliance is required. However, according to Liouville's theorem this implies a small source size A_1. That means that the electrons must be focused on a small targed area, which results in a higher electron power density on the target. Approximately one percent of the incident electron beam energy is converted into X-rays [36]. The rest of the enegry is deposited as heat into the target material. Therefore, increasing the electron power density on the target must be compensated by proper heat management to ensure a reasonable target life time.

In conventional sealed tube sources the electron beam is hitting the anode as line focus to distribute the electron power over a larger anode surface. Under a tack-off angle of typically 6° the apparent souce size seen by the optics is given by the line focus size multiplied by a correction factor $\sin(6°) \approx \frac{1}{10}$. In this manner, the power density load can be decreased but the effective source size remains small. Further heat management improvement can be achieved by the rotating anode technology. In Figure 4.14 a schematic illustration of the working principle of a rotating anode using the line focus is depicted. The temperature rise of the anode can be given as

$$\Delta T = \frac{2P}{2ld}\sqrt{\frac{d}{\pi^2 f R \mu \rho c_p}} \tag{4.3}$$

where P is the electron beam power, l is the length and $2d$ the width of the electron spot, f the rotation frequency, R distance between the anode axis and the center of the electron spot, μ is the thermal conductivity and ρ and c_p are the density and specific heat capacity of the anode material [45]. For a given admissible temperature increase and assuming even unrealistic values for R and f (R=1 m and f=1 kHz) the power density would increase only by a factor of approximately 6 [27]. Therefore, it seems unlikely that a considerable heat dissipation improvement, and thus brillance increase, can be realised for compact laboratory rotating anode X-ray sources. Hence, to overcome these restrictions

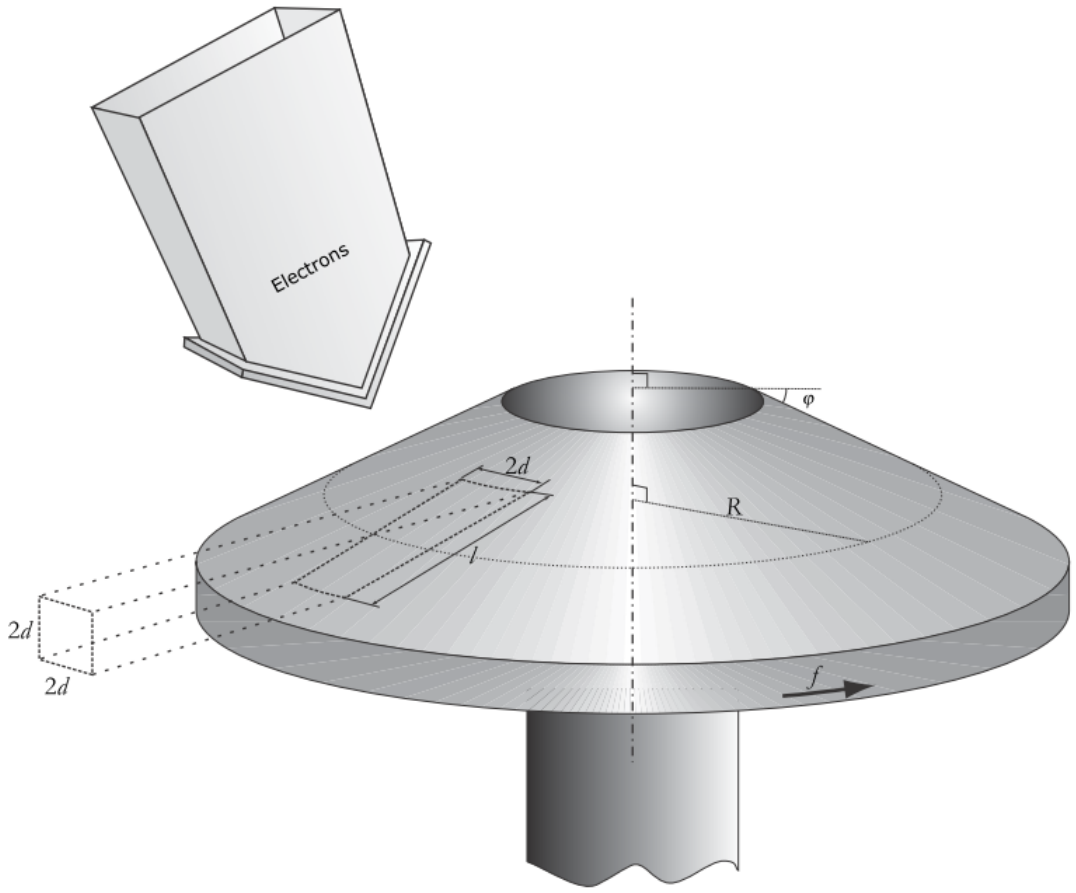

Figure 4.14: Schematic illustration of a rotating anode irradiated by an electron beam with line focus. Taken from [35].

which limit the maximal electron power density load a novel X-ray source concept must be developed. The new concept must allow for a higher power density load on the target compared to state of the art rotating anode X-ray sources. This can be achieved by applying a jet of liquid material as target. In this manner a high flow speed of the jet results in sufficient renewal of the target material and heat removal.

The first liquid target X-ray source is provided by Excillum AB. The source is refered as MetalJet X-ray source. The target material is a gallium-indium alloy (Alloy77: 95 % Ga, 5 % In, % in mass)) which is liquid at room temperature. In the following the basic working principle of the MetalJet X-ray source is described.

4.2.2 Working principle of the MetalJet X-ray source

The working principle of the MetalJet X-ray source is illustrated schematicaly in Figure 4.15. The core component of the MetalJet X-ray source is the liquid metal loop system, composed of a liquid metal pump and a dedicated nozzle which produces a metal jet to be bombarded with electrons. By generating a pressure of up to 190 bars the liquid metal pump maintains a continous circulation of the metal and consequently assures a renewable target. The liquid metal is pressed through the nozzle which is specialy designed

to produce the high-speed jet. The major challenges in designing the nozzle are associated with achieving a laminar metal flow, reasonable breakup length (length after which the jet breaks up into droplets) and position stability of the jet [55, 56]. The diameter of the jet is around 180 µm. To produce X-rays the jet is irradiated with an electron beam. The

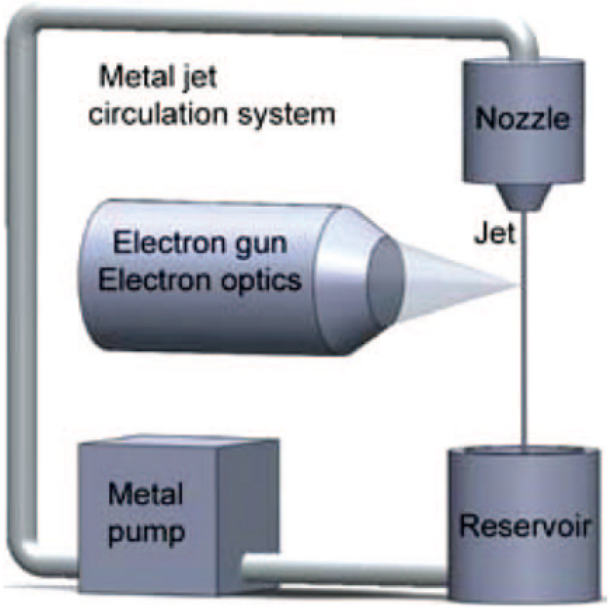

Figure 4.15: Schematic illustration of the components of the MetalJet X-ray source. Taken from [47].

electrons are generated with a LaB_6 cathode. In standard operation mode the high voltage is 70 kV. The cathode is heated by a current so that by thermal field emission electrons are emitted out of the cathode. The emitted electron current is 2.857 mA. Consequently, the source operates with 200 W. The electrons are then focused with the aid of magnetic coils onto the jet. Excillum's control software provides electron beam size values. The intensity profile of the electron beam is assumed to be gaussian. The electron beam size at jet position is given as FWHM in horizontal and vertical direction as 80 µm x 20 µm as indicated in Figure 4.16.

Excillum's control software enables the user to adjust the horizontal position of the electron beam on the jet. By this means one can modify the shape and size of the X-ray source by moving the electron beam horizontaly along the x-direction, whereas size and shape are largely translationary invariant regarding movements along the y-direction. The impact of shifting horizontally the electron beam on the jet is twofold: first, as shown in Figure 4.17 with increasing displacement from the x=0 position the horizontal size of the X-ray source increases. Therefore, more X-rays are emitted on the side of the jet facing the optic. Secondly, as electrons penetrate the jet, X-rays are also produced inside the jet. Therefore, X-rays produced closer to the jet surface will transit less distance through the jet. Hence, shifting the electron beam towards larger horizontal positions reduces self-absorption effects. Both effects lead to an increase of the generated X-rays.

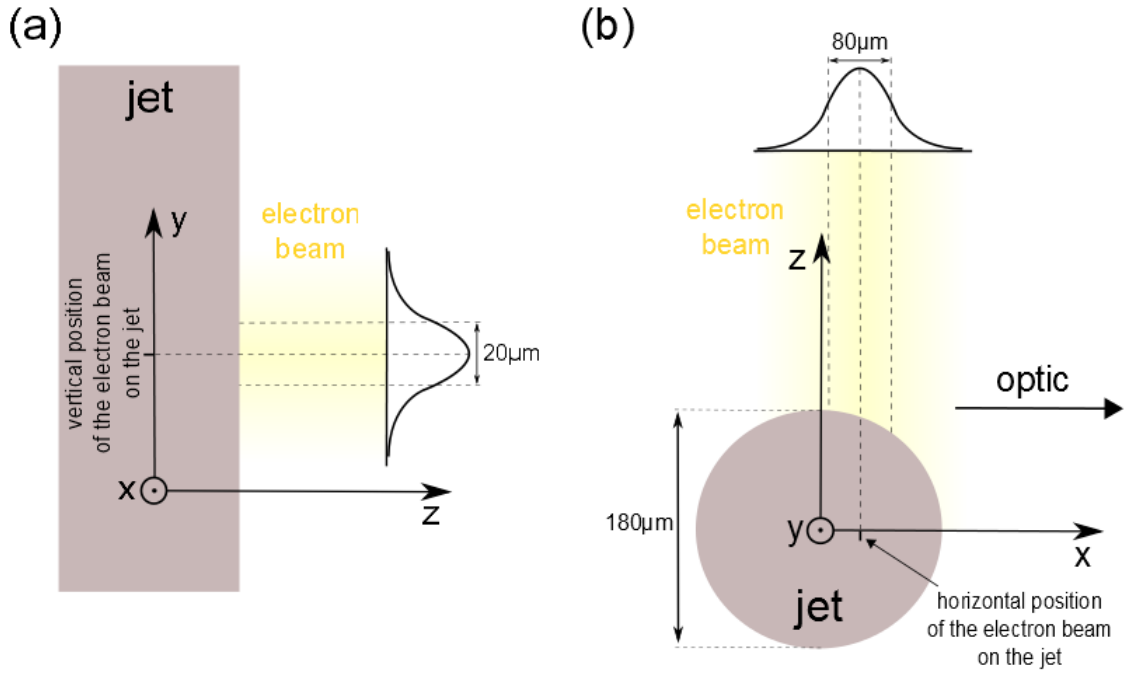

Figure 4.16: Vertical (a) and horizontal (b) position and size of the electron beam.

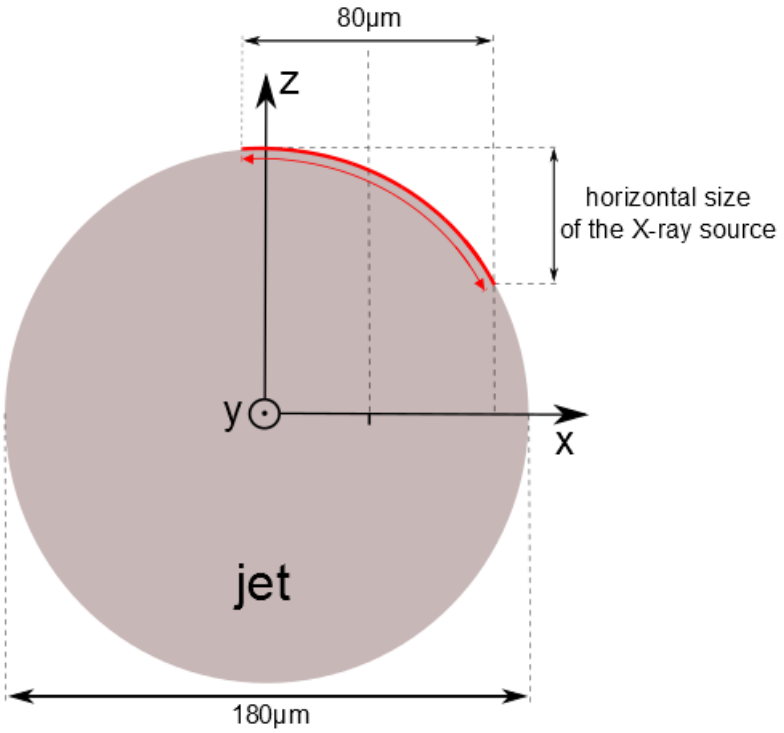

Figure 4.17: Projection of the electron beam profile on the cylindric jet. The resulting X-ray source is indicated by the red segment.

However, with increasing horizontal position the irradiated surface on the jet increases. This leads to a decrase of the electron power density. The optics accepts only a certain effective source size. The catched X-rays by the optics originate from this effectiv source. Therefore, if the horizontal source size exceeds the effective source size, the caught X-ray

flux decreases due to the decreasing electron power density. Consequently, finding the optimal electron beam position is a trade-off between self-absorption and source size.

The influence of the electron beam position is investigated by measuring the X-ray flux behind the optics. The resulting normalized X-ray flux as function of the horizontal position of the electron beam on the jet is displayed in Figure 4.18. The maximal flux value is found at a horizontal position of x=20 µm. A gain of approximately 10 % of flux is observable with respect to x=0 µm position. This result indicates that the brilliance value also increases at given effective source size A_1 and capture angle Ω_1 of the optics. [5]

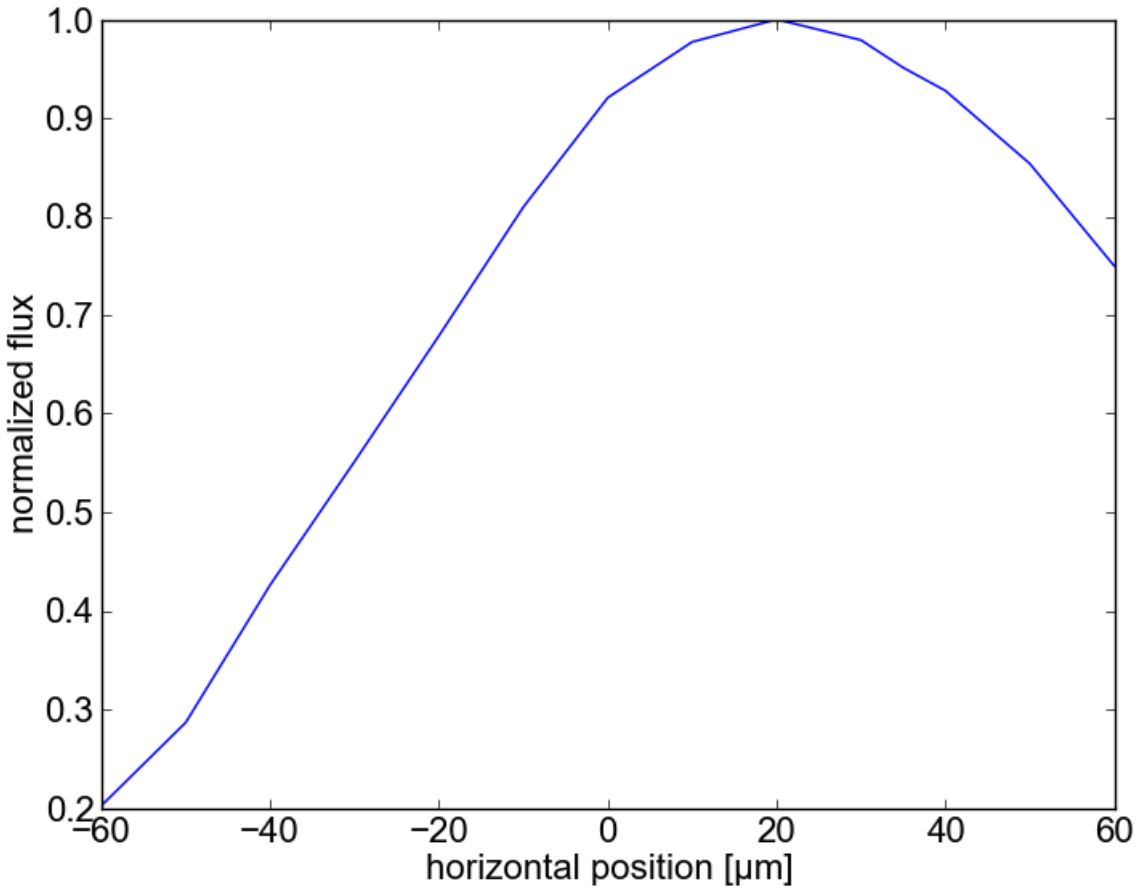

Figure 4.18: Flux (normalized on the maximal flux value) behind the optic as function of the horizontal position of the electron beam on the jet.

[5] It can be assumed that for another type of optics the maximal flux is at a different electron beam position.

4.2.3 Summarized overview of the performance of the MetalJet-NanoSTAR compared to IμS- and RAG- NanoSTAR systems

Comparison of the performance of X-ray sources is a debatable issue as the performance depends also on the optics which determines the beam size and divergence. For different application different aspects of beam conditioning play an important role. In case of applying SAXS on nanoparticle solutions high flux at sample position is of importance to obtain a reasonable exposure time. Furthermore, the X-ray beam may also be further conditioned with slits or pinholes. Therefore, it is more convenient to compare the performance of the system composed of the source, optic and pinholes. In particular, the flux of the actual beam which is used to irradiate the sample is of interest. In Table 4.6 flux values for the IμS, RAG and the MetalJet source are summarized. The flux was measure with the V2000 detector. As the MetalJet source operates with the Ga-K_α ($\lambda = 1.34\,\text{nm}$) emission line, the wavelenght differs from Cu-K_α sources ($\lambda = 1.54\,\text{nm}$). Therefore, glassy carbon (GC) scattering intensities were also measured. For all NanoSTAR systems the standard pinhole setup was utilized. As can be inferred from Table 4.6 the flux increases significantely when using the MetalJet-source. The flux increases by a factor of 3 compared to the RAG-NanoSTAR and by a factor of 12 compared to the IμS-NanoSTAR system. The GC intensity increases by a factor of 4 and 19, respectively.

X-ray source	flux of actual X-ray beam [cps]	GC intensity [cps]
IμS (focusing optics)	$0.17 \cdot 10^8$	$0.15 \cdot 10^6$
RAG (collimating optics)	$0.7 \cdot 10^8$	$0.7 \cdot 10^6$
MetalJet (focusing optics)	$2.1 \cdot 10^8$	$2.9 \cdot 10^6$

Table 4.6: Comparative summary of beam flux and GC intensity values measured after the standard pinhole setup with the V2000 detector.

The GC intensity increase factors are larger compared to the flux increase factors. This can be attributed to the fact that the X-ray beam from the MetalJet source has a higher energy and the scattered X-rays are attenuated less inside the GC sample. Therefore, the actual scattered intensity compared to Cu X-ray sources will depend on the sample under investigation. In Table 4.7 increase factors of the scattered intensity compared to a RAG NanoSTAR system are summarized for two standard samples collagen and silver behenate.

Additionally, MetalJet- and IμS -NanoSTAR are compared when both are equipped with the double SCATEX pinhole setup ($2 \times 550\,\mu\text{m}$ pinholes). The SCATEX setup is

sample	increase factor
collagen from rat tail tendon	2.7
silver behenate ($AgC_{22}H_{43}O_2$)	2.4

Table 4.7: Increase factors of the scattered intensity from collagen and silver behenate compared to a RAG-NanoStar system.

descibed in section 4.1.2.[6] Similarly, here a considerable flux (GC intensity) increase by a factor of 12 (28) is also observable as shown in Table 4.8.

X-ray source	flux of actual X-ray beam [cps]	GC intensity [cps]
IμS	$0.32 \cdot 10^8$	$0.26 \cdot 10^6$
MetalJet	$3.7 \cdot 10^8$	$7.2 \cdot 10^6$

Table 4.8: Comparative summary of beam flux and GC intensity values measured after the SCATEX pinhole setup with the V2000 detector.

All in all, using the MetalJet X-ray source provides a higher beam flux at sample position and higher intensity of the scattered X-rays. In the view of real-time monitoring of nanoparticle production this allows for a higher sampling rate.

4.3 VascoFLEX Particle Size Analyzer

In standard DLS devices the liquid sample is injected into a cuvette placed inside the instrument before measurement. This configuration is appropriate for many laboratory applications, but it cannot be coupled with other particle characterization techniques. Thus, simultaneous measurements within the same sample volume are not possible. Therefore, a DLS device was developed by Cordouan Technologies and named as VascoFLEX Particle Size Analyser. The VascoFLEX DLS device can be integrated into the NanoSTAR sample chamber for simultaneous measurements.

The VascoFLEX DLS system is based on the Optical Fiber Remote Head (OFRH). A schematic drawing is shown in Figure 4.19. The OFRH integrates into the same case housing both the sample illumination optical system and the scattered light collector with its optical axis set at an angle of 165° with respect to the incident laser beam. The working distance of the probe (i.e. the distance between the OFRH and the sample capillary) is set to 70 mm. The illumination and the collector systems are made of two optical collimators, one used as focuser and the other as a condenser. Furthermore a temperature sensor (PT100). The temperature sensor and the optics are linked to a

[6]No flux data on RAG-NanoSTAR with SCATEX pinholes are available.

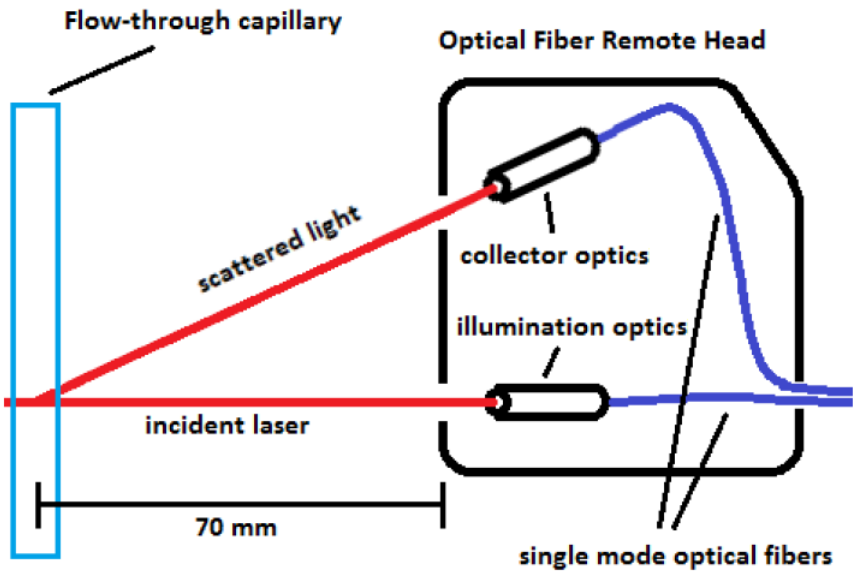

Figure 4.19: Schematic illustration of the Optical Fiber Remote Head (OFRH) placed 70 mm from the flow-through capillary. The (OFRH) contains the illumination and the collectoin optics.

central unit. In the central unit a 60 mW laser diode emitting at a wavelength of 658 nm and an avalanche photo diode (APD) are situated. One polarization maintaining fiber is used to connect the illumination optics with the laser diode. The APD is connected to the collector optics via a standard single mode fiber.

The polarization of the laser beam is aligned in a direction perpendicular to the plane of incidence defined by the laser and the collecting beams. The laser beam diameter in the measurement area is about 200 µm.

Furthermore, in the central unit a linear correlator is integrated. The collerater has 1000 channels and calculates the auto-correlation function which is then further processed by Cordouan's software.

The DLS OFRH was integrated inside the SAXS sample chamber. It is mounted on the XY-stage together with a capillary holder as shown in Figure 4.20. To prevent the X-ray beam from being blocked by the DLS head housing, the OFRH was turned aside by an angle of 35° with respect to the X-ray beam where the center of rotation was the sample position.

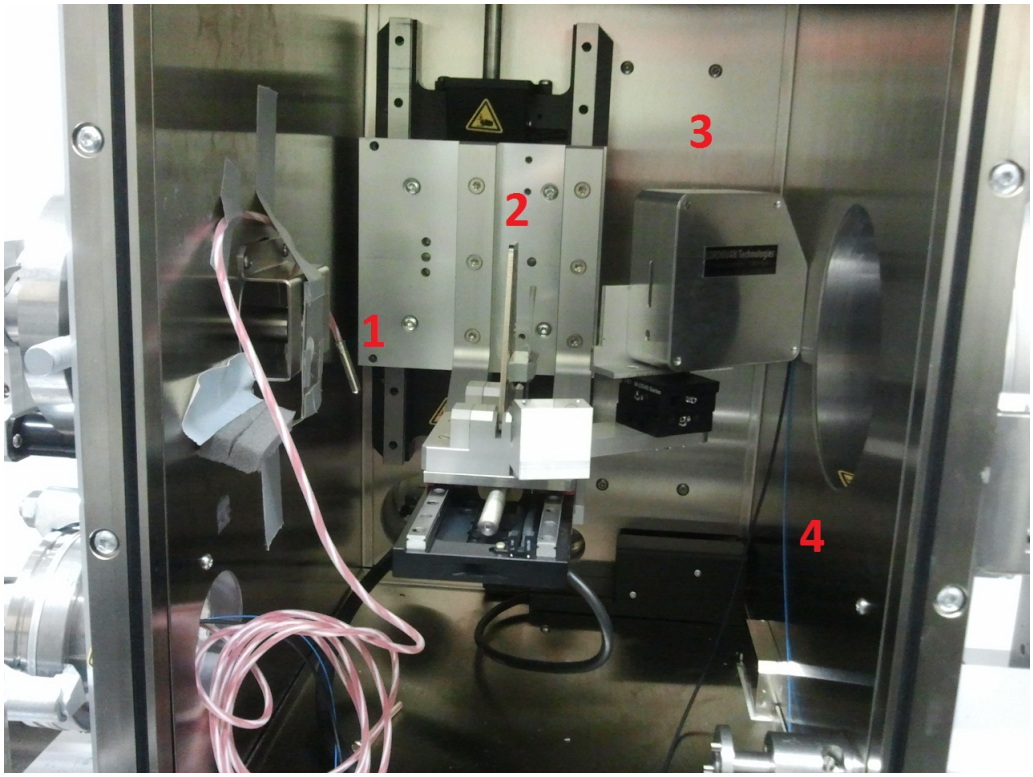

Figure 4.20: VASCO Flex DLS device (3) integrated into the Nanostar sample chamber. Furthermore, the temperature sensor (1), the sample holder (2) and the opticle fibers (4) are shown.

Chapter 5

Silica nanoparticle production and monitoring

In this chapter all aspects related to nanoparticle production and characterization are discussed. First, the experimental setups are introduced, which comprise the synthesis system, flow-through capillary and integration of SAXS and DLS. Finally, the measurement procedure and the analysis software are explained.

5.1 Synthesis of silica nanoparticles

In this work silica (SiO_2) NPs serve as the model system. The sol-gel process is the most prominent way of generating silica NPs . It involves the hydrolysis of tetraethylorthosilicate (TEOS or $Si(OR)_4$ with R=C_2H_5) and condensation of the hydrolysed species. It is known as the Stöber method [68]. The conversion of TEOS into SiO_2 can be described by the following reaction equation [29]:

$$Si(OR)_4 + 2H_2O \rightarrow SiO_2 + 4ROH \tag{5.1}$$

Here, ROH is ethanol. Hydrolysis and condensation can be specified as:

$$Si(OR)_{4-x} + xH_2O \xrightarrow{\text{hydrolysis}} OH_xSi(OR)_{4-x} + xROH \tag{5.2}$$

$$Si(OR)_4 + (OH)Si(OR)_3 \xrightarrow{\text{alcohol condensation}} (OR)_3Si - O - Si(OR)_3 + ROH \tag{5.3}$$

$$(OR)_3Si(OH) + (OH)Si(OR)_3 \xrightarrow{\text{water condensation}} (OR)_3Si - O - Si(OR)_3 + H_2O \tag{5.4}$$

Generally, a base catalyst such as ammonia is used to promote hydrolysis and condensation. The first step of NP formation is the hydrolysis of TEOS which yields the hydrolysed species. As the reaction progresses, the concentration of the species increases. According to the LaMer-Dinegar theory [46] the concentration reaches a level where condensation

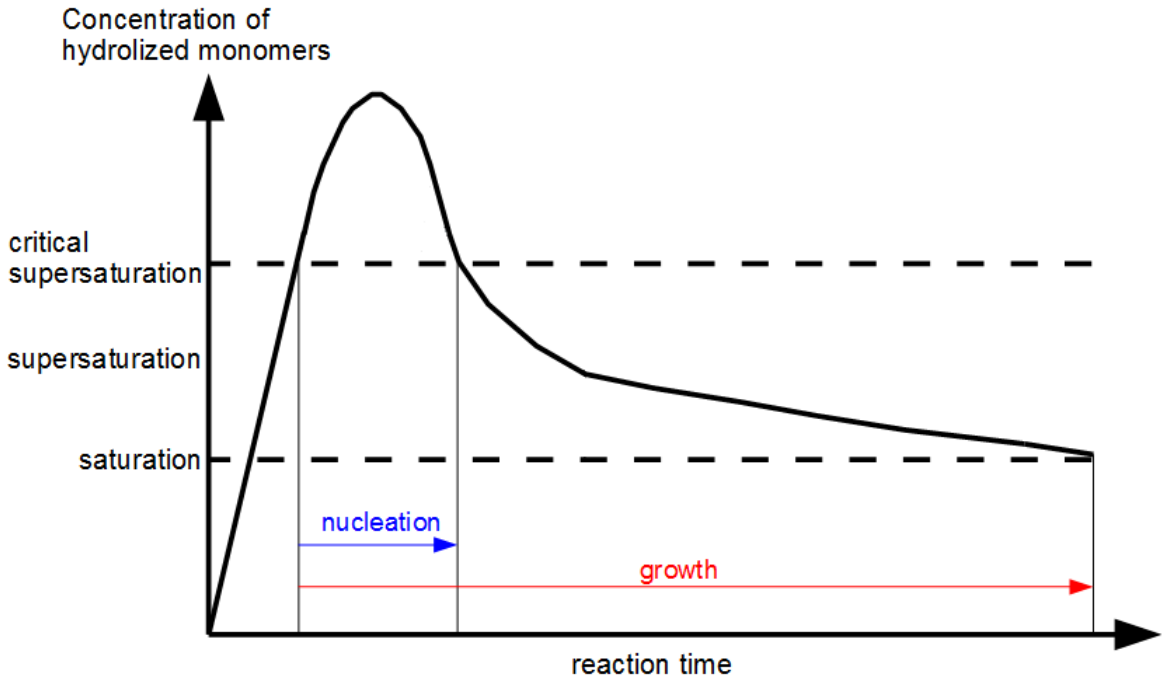

Figure 5.1: Evolution of the monomer concentration according to the LaMer-Dinegar theory [46].

starts upon reaching a critical supersaturation as shown in Figure 5.1. The hydrolyzed species are considered as monomers which form dimers and oligomers. As a consequence, the first nuclei are produced which serve as nucleation sites for further particle growth. After initiation of the nucleation the monomers are used for further growth of the nuclei. The consumption of the monomers inhibits the concentration increase till it reaches its maximum value. While the concentration is above the critical supersaturation level nucleation and growth coexist. If the concentration falls under the supersaturation level production of new nuclei is stopped. However, growth is still persisting owing to contineous condensation of monomers to the particle surface and supply of new monomers due to the hydrolysis reaction. This growth mechanism is denoted as the monomer-addition model [52]. Additionally, it was reported that particles can also grow by aggregation of the nuclei. This is denoted as the aggregative growth model [12] and was observed at high water concentrations [57].

In the monomer addition model nucleation and growth are coexisting. Consequently, nuclei produced first will be the largerst at the end of the growth process. Therefore, the key to produce monodispersed NPs is to separate the nucleation phase from the growth phase. This can be achieved by retarding the monomer supply rate so that the concentration remains much shorter above the critical supersaturation level and growth of nuclei in this time slot is negligible. Consequently, the nuclei are nearly uniform in size after nucleation and the following growth phase will yield monodispersed NPs. The monomer supply rate can be controlled by using different alcohols such as ethanol, methanol or propanol [30, 48]. Furthermore, reaction temperature, ammonia and water

with respect to the TEOS concentration are important parameters to control the monomer supply rate. These synthesis conditions are specified in a great number of reports for batch and semi-batch reactions and in some reports for microfluidic synthesis [40, 18, 31].

5.2 Silica nanoparticle production

5.2.1 Assembling the nanoparticle production line

Nanoparticle production with Syrris' Asia flow-chemistry system

For the silica NPs synthesis a flow-chemistry system from Syrris was used (Asia Flow-Chemistry system). The Asia system is shown in Figure 5.2. It features two syringe pumps, which are designed to provide a uniform pressure-driven flow. The flow speed of each pump can be adjusted between 10 μl/min and 2.5 ml/min. The main component of the system is the micro-flow reactor chip. The reactor can be cooled or heated in a temperature range from -15°C to 150°C. Syrris provides reactor chips with different sizes. In this work two reactors were used having volumes of 250 μl and 1000 μl, respectively.

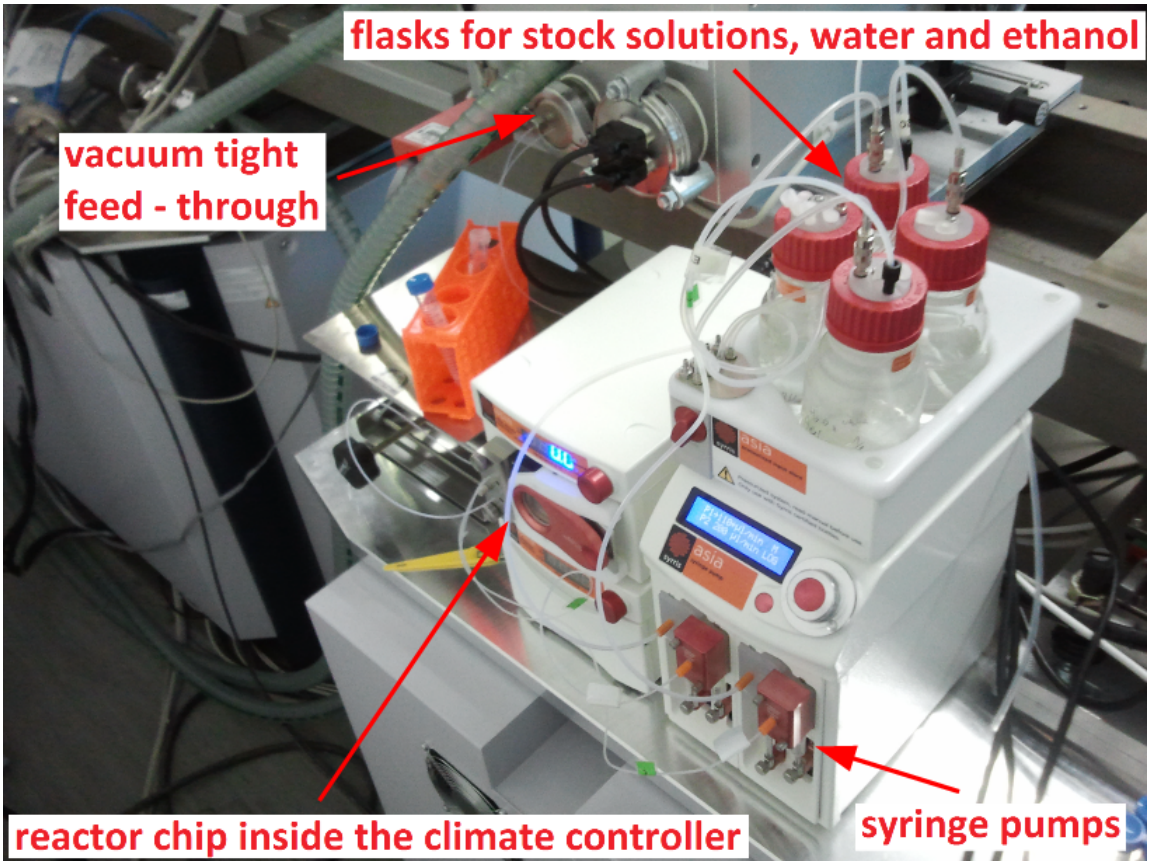

Figure 5.2: Asia flow chemistry system from Syrris placed at the back side of the Nanostar.

Prior to each synthesis run two precursor solutions were prepared. The first solution was ammonia in water with a concentration of 747 mM[1]. The concentration of the first

[1] 1 M = 1 mol/l

solution was kept constant for all experimental runs. The second solution was TEOS in ethanol. In the course of the project different TEOS concentrations were tested in a range from 60 mM to 224 mM. Upon injection of both solutions into the reactor chip, mixing occured and the reactions according to equations 5.2, 5.3 and 5.4 started. The influence of the reactor temperature T, the overall flow rate $F_1 + F_2$ and the flow rate ratio F_1/F_2 on the size and size distribution were investigated. F_1 and F_2 denote the flow rate of ammonia from the first pump and TEOS from the second pump.

In this work two setups were tested. Both are illustrated schematically in Figure 5.3. The two flasks with the precursor solutions were connected to the pumps. The first setup involves one microreactor of the size of 1000 μl. The reactor is situated in the climate controller so that the temperature can be manipulated during the experiment. The inlets of the reactor are connected to the two pumps, whereas the outlet is connected to the flow-through capillary. Thus, the working principle of the production process can be described as following: the pumps inject the two precursor solutions into the reactor where the mixing and the reaction take place. Under appropriate synthesis conditions particles are formed during the tranfer through the reactor chip. Then the particles are guided into the flow-through capillary to be characterized with SAXS and DLS. The first setup is referred as R1-setup in the following of the thesis.

In the second setup two reactors were used; the 250 μl reactor was placed inside the climate controller, whereas the 1000 μl reactor was at room temperature. The second reactor acted as an extended delay to let the particles grow longer before reaching the capillary. The second setup is referred as R2-setup in the following of the thesis.

PTFE (Polytetrafluoroethylene) pipes were used for all pump-reactor, reactor-reactor and reactor-capillary connections. The pipes have an inner diameter of 0.8 mm. As the capillary was located inside whereas the reactor was located outside the SAXS sample chamber the produced particles were characterized after some delay time. The time delay depends on the overall flow rate. In the R1-setup the length of this connection was kept as short as possible but left some freedom to release tension from the pipe. The length of the pipe was then chosen to be 900 mm. The resulting volume of the pipe between reactor and capillary was approximately 450 μl. In this work a of maximal flow rate of 120 µl/min was used, which corresponds to a delay time of 3.7 min. In the R2-setup the first reactor had a volume of 250 µl. The delay line was composed of two pipes with a volume of 250 µl and 450 µl, respectively, and a second reactor with a volume of 1000 µl. The resulting overall volume of the delay line was 1700 µl resulting in a delay time of approximately 14 min.

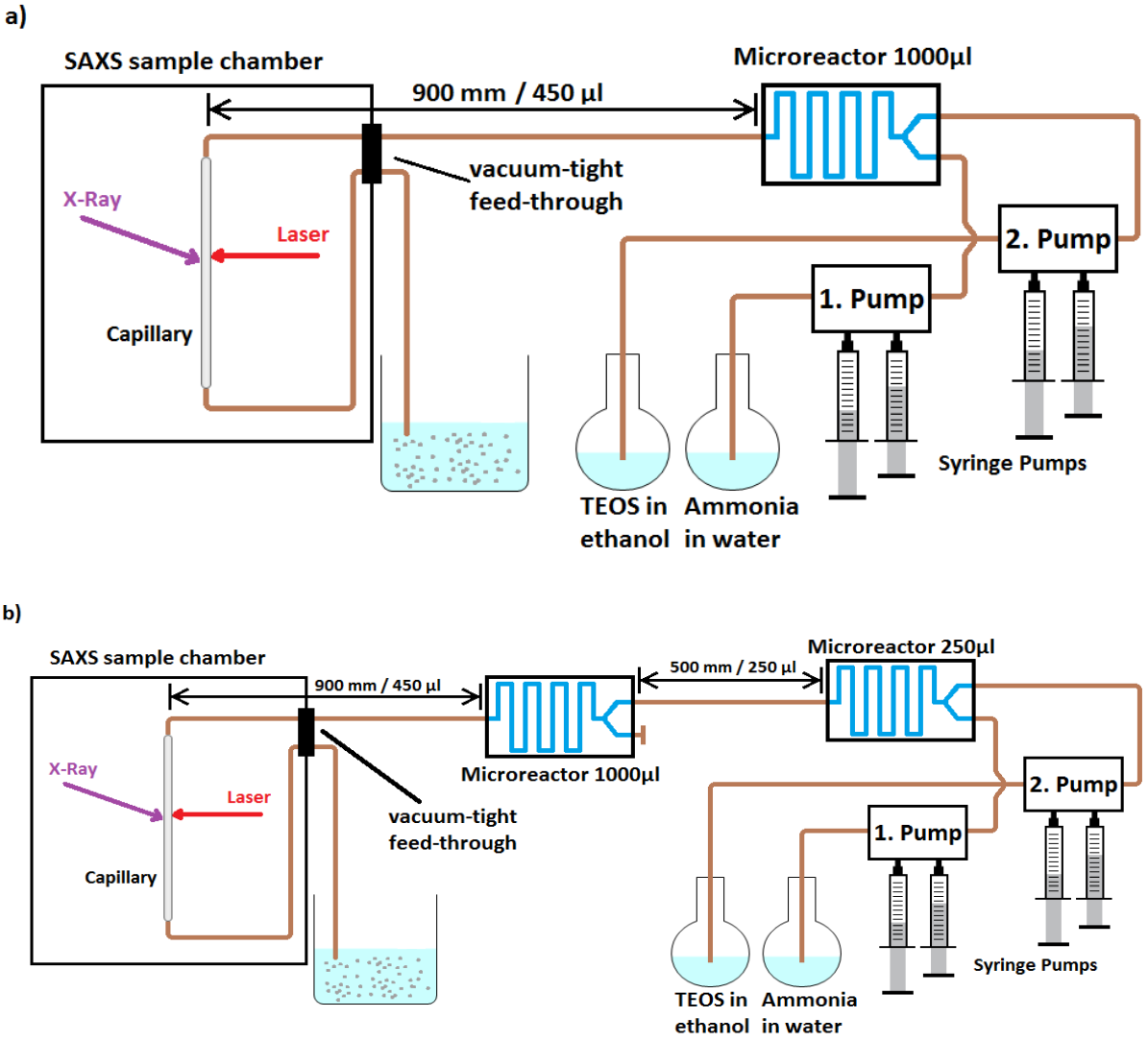

Figure 5.3: Schematic illustration of the two experimental setups. In a) the R1-setup is sketched. This setup involves one reactor with a volume of 1000 µl. The delay line between the reactor has approximatelly a volume of 450 µl. In b) the R2-setup is illustrated. In the first reactor with a volume of 250 µl the reaction and nucleation is initiated. The particles are then guided through a delay line consisting of two tubes and a second flow reactor. The overall volume of the delay line is 1700 µl.

Flow-through capillary

There are two main requirements for a flow-through capillary being used for SAXS measurements. Firstly, the capillary must be vaccum tight, i.e. the pipes leading the particles to be measured must be connected to the capillary in a vacuum-tight manner as the SAXS sample chamber is evacuated in advance of each experimental run. Secondly, the walls of the capillary are desired to be as thin and uniform as possible to ensure high transmission and to reduce parasitic scattering from the capillary. The wall thickness of capillaries used for X-ray transmission experiments is typically around 10 μm. This makes the capillaries very fragile and the fabrication of proper flow-through capillaries becomes a challenging

task when using these kind of standard capillaries. The capillaries must be embbeded in a firm frame due to their fragility. On the other hand, the pipes leading the NP solution to be measured must be connected to both ends of the capillary and sealed against air. Bruker AXS provides flow-through capillaries where the sealing is accomplished with the aid of union nuts. However, those turned out to be not suitable to be used for simultaneous SAXS and DLS measurements. The main reason is that the windows are too small and the capillary is not accessable for DLS. Thus, Bruker's flow-through capillaries can only be used for SAXS measurements. Hence, a capillary had to be designed dedicated to experiments where simultaneous SAXS and DLS measurements are involved. The main requirement for the new capillary is that it must be applicable for SAXS and DLS simultaneously. A first series of capillaries was fabricated in the glas blowing workshop at KU Leuven. The capillaries were made of glass and turned out to be more robust then the commercial ones due to a larger wall thickness.[2]. Owing to their robustness the capillaries were withstanding the cleaning processes.[3] The capillaries had a length of 8 cm and an inner diameter of approximately 2 mm. This facilitated to connect the capillary's ends to the pipes having an outer diameter of 1.6 mm. The pipes were inserted into the capillary on both ends after a two-component glue was applied at the outer walls of the pipe's ends as shown in Figure 5.4. By this means the glue fixed the pipes inside the capillary and sealed the capillary against air.

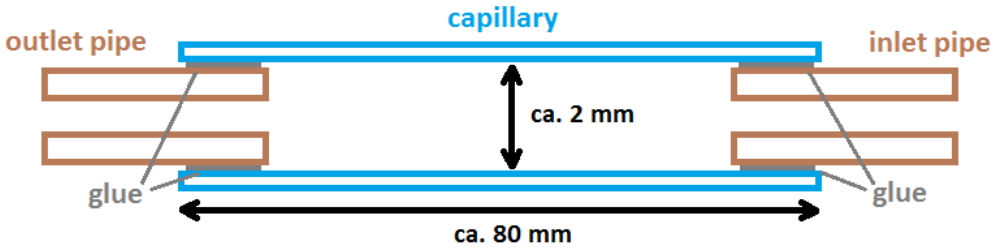

Figure 5.4: Cross-section of the capillary connected to pipes on both ends. The pipes are glued to the capillary for fixation and vacuum-tight sealing.

The width of the X-ray beam was approximately 1 mm and consequently smaller then the inner diameter of the capillary. The transmission of the capillary was determined to be 17 %. On the one hand, this is a rather low transmission value. On the other hand, in preliminary test measurements the measured scattering intensity was sufficient. Furthermore, the fabrication approach turned out to be feasible and the resulting flow-through capillary was vacuum tight and could be used for nanoparticle production monitoring.

For first experiments the capillary was mounted vertically (perpendicular to the XY-table) as shown in Figure 5.5. This alignment allowed for simultaneous SAXS and DLS

[2]The wall thickness is estimated to be 100 μm - 200 μm.

[3]Cleaning in an ultrasonic bath was inevitable and frequently performed to free the capillary from contaminations arising from sticking particles or partially hydrolized or polymerized species.

measurements. However, for DLS measurements the flow must be stopped as in this alignment the flowing particles would give rise to Doppler frequency shifts of the scattered light. In turn, this would lead to faulty auto-correlation functions. To minimize the

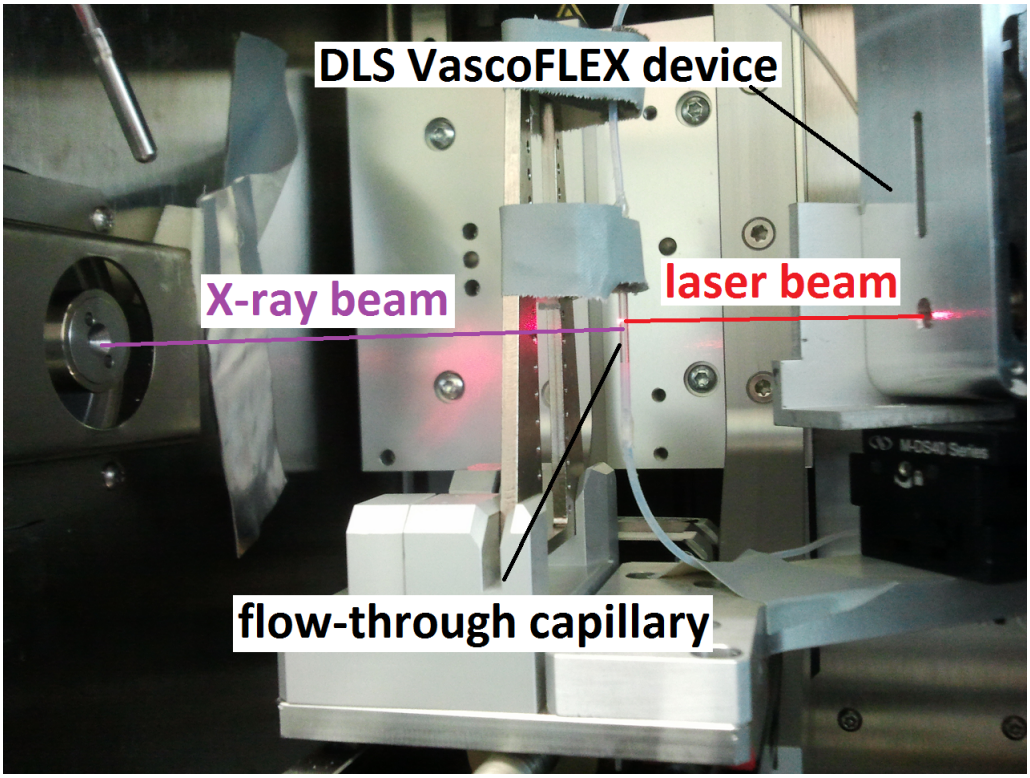

Figure 5.5: Dedicated flow-through capillary integrated inside the Nanostar sample chamber. Owing to the large window inside the plastic framework the capillary is accessible by the X-ray and laser beam simultaneously.

Doppler frequency shift the capillary was aligned horizontally (parallel to the XY-table). Additionally, the capillary was tilted with respect to the X-ray beam by an angle of 55°. In this way the capillary was aligned perpendicular to the incident and the scattered laser beam. Thus, the flow velocity and scattering vector were almost perpendicular within the alignment accuracy: $\mathbf{q} \cdot \mathbf{v} \approx \mathbf{0}$. The capillary was integrated into a plastic frame and mounted on the sample holder. The plastic frame was fabricated in the mechanical workshop at the KU Leuven. In Figure 5.6 the capillary is shown inside the SAXS sample chamber. Owing to the large window in the frame the capillary was accessible by both the X-ray and the laser beam allowing for simultaneous measurements with SAXS and DLS.

5.2.2 Measurement and analysis software for SAXS

The raw 2D SAXS frames were recorded using Bruker's SAXS(TM) software. The software integrates the 2D frames to obtain the 1D intensity-vs.-q curve. An example of a recorded 2D frame is illustrated in Figure 5.7. In the center of the frame the shadow

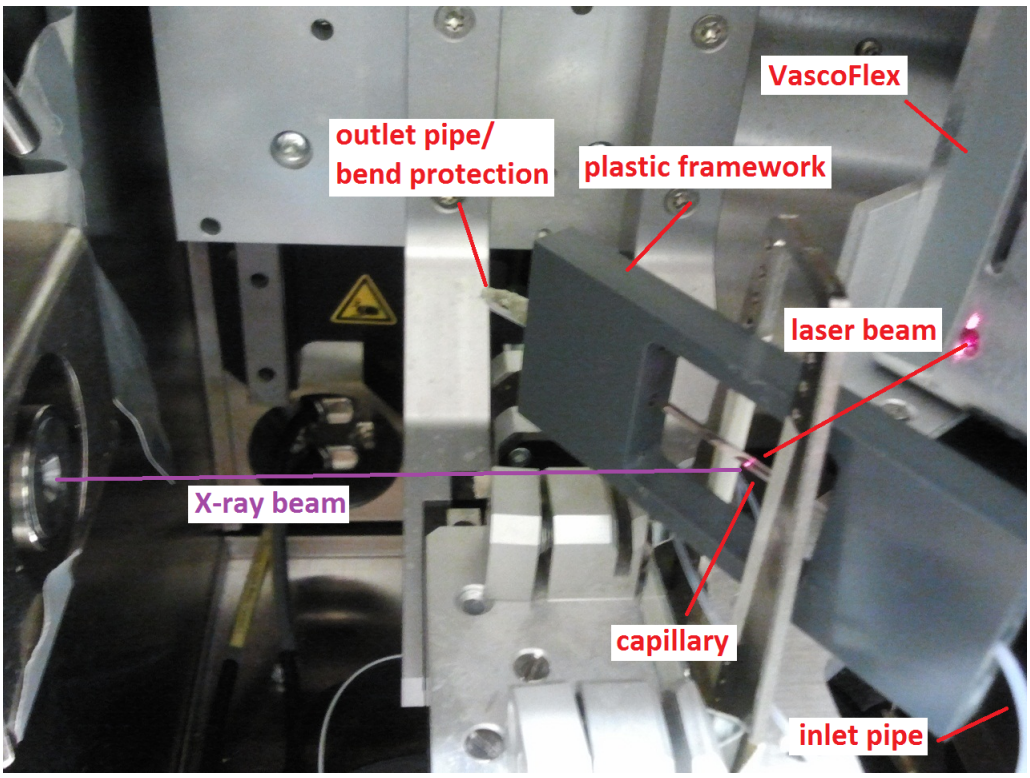

Figure 5.6: Flow-through capillary integrated into a frame and mounted on a sample holder inside the Nanostar sample chamber. Owing to the large window inside the plastic framework the capillary is accessible by the X-ray and laser beam simultaneously.

of the beam stop is visible, around which the SAXS signal of the particles is detected. Prior to the integration, the SAXS software performes spatial and floodfield corrections.[4] Further reduction of the raw data, background correction and model function fitting were performed with scripts written in Python.

Raw data reduction

Generally, the measured intensity I_m must be corrected for detector noise I_{dn} and polarization. Moreover, the measured intensity is normalized on the measurement time. All corrections can be summarized as [33]

$$I = (I_m/t_m - I_{dn}/t_{dn})\frac{1+\cos^2(2\theta)}{2}\,, \tag{5.5}$$

where t_m and t_{dn} are the sample measurement time and the detector background measurement time, respectively. The detector noise is measured without X-ray beam. The detector background of the V2000 can be neglected as it is below 5 cps[5] uniformly distributed over the detector area.

[4] The spatial correction accounts for the fact that the detector surface is conic. The floodfield correction corrects for possible non-uniform sensitivity distribution over the detector area.

[5] count rate: counts/s = cps

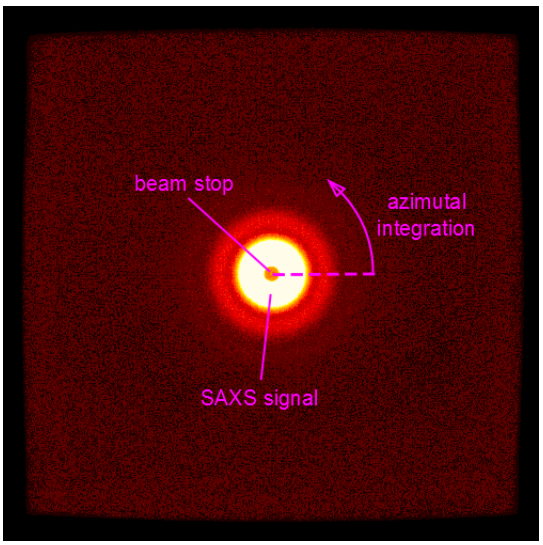

Figure 5.7: Illustration of a 2D SAXS frame recorded using SAXS(TM) software from Bruker.

In the experiments performed in this work typical values for the local and total count rate are 2 cps/pixel and 45 kcps , respectively. These values are within the linearity range of the detector.

There are some other corrections for e.g. finite X-ray beam size and multiple scattering. Both give rise to smearing of the true scattering profile. Smearing effects can be tremendous, for example when slit collimation is used to shape the X-ray beam. Multiple scattering occures if strongly scattering and thick samples are under investigation. Nevertheless, these corrections are neglected in this work as pinhole collimation is used which results in a circular beam shape. The beam diameter is approximately 1 mm which is sufficiently small so that smearing effect due to finite beam size can be neglected. Furthermore, multiple scattering effects were not observed during the work.

Background correction

To extract information about the sample under investigation from the scattering curve it is unavoidable to perform a thorough background correction. There are several contributions to the background comprising air scattering, scattering from the capillary and scattering from the solvent.

Prior to executing the background correction both the background and the sample data need to be corrected for absorption effects. The absorption is described by the Lambert-Beer equation:

$$I(d) = I_0 e^{-\mu d} \,. \tag{5.6}$$

The transmitted intensity $I(d)$ depends on the thickness d and the linear attenuation coefficient μ of the sample. The fraction of the transmitted intensity with respect to the

incident intensity I_0 can then be defined as

$$T = \frac{I(d)}{I_0}\,. \tag{5.7}$$

The intensity $I_{sample}(q)$ obtained from the sample is defined by both the particles and the buffer, in which the particles are suspended. The buffer gives rise to the background signal. Thus, the measurement of the buffer and determination of the transmission of the buffer must be performed separately from the measurement of the sample. Consequently, absorption in the background correction procedure can be taken into account according to

$$I_{corr}(q) = \frac{1}{T_S} I_{sample}(q) - \frac{1}{T_B} I_{buffer}(q) \tag{5.8}$$

where $I_{corr}(q)$ contains solely scattering from the particles.

In a real-time monitoring experiment as presented in this work a change of synthesis parameters such as the flow rate ratio leads to a change of the composition of the buffer as the ethanol-water ratio is changed. Consequently, this results in a change of the transmission value T_B. Furthermore, the transmission of the sample depends on the particle size and particle number density which are highly affected by synthesis temperature and flow rates. This causes T_S to be a varying parameter, too. In Table 5.1 transmission values T_S for some sets of synthesis parameters are summarized. One can see that changing the overall flow speed and the flow rate ratio influences the transmission value. In contrary, temperature changes seem to have less influence. As a consequence, when using fixed

$F_1 + F_2\,[\mu\mathrm{l/min}]$	$\frac{F_1}{F_2}$	$T\,[^\circ\mathrm{C}]$	T_S
120	1/2	55	0.17
110	1/2	55	0.24
100	1/2	55	0.27
100	1/2	50	0.27
100	1/2	60	0.27
100	1/3	60	0.23

Table 5.1: Summary of some synthesis parameters such as the overall flow rate $F_1 + F_2$, flow rate ratio $\frac{F_1}{F_2}$ and the reactor temperature T and corresponding transmission values T_S.

transmission values the background correction would be insufficient for certain synthesis parameters where flow rate changes are involved. In turn, this would cause faulty size determination or a failure of a model fitting procedure.

To overcome this problem the transmission values must be adapted dynamicaly to the current synthesis conditions during the experiment. To achieve this, the following

approaches can be considered: the transmission value T_S is determined directly after the SAXS measurement. Whereas, all T_B values are determined for each synthesis parameter set before the monitoring experiment. The disadvantage of this approach is that it limits the flexibility during the experiment as only a limited amount of flow rate values (namely those used for the determination of T_B) are available for a proper background correction. Additionally, a manual input of the T_B values would be required for the background correction whenever the flow rate (ratio) changes during the experiment. However, this is not in accordance with the idea of an automated monitoring process without user intervention, even though a sufficient background correction for any combination of the synthesis parameters is necessary.

Alternatively, to establish an automated background correction and minimize users intervention a second approach is proposed in this work. This approach doesn't require an explicite use of the transmission values T_S and T_B. Scattering from the buffer is considered to be composed of ethanol and water:

$$I_{buffer}(q) = aI_{ethanol}(q) + bI_{water}(q)\,. \tag{5.9}$$

The ethanol and water intensities are corrected for capillary scattering according

$$I_{ethanol}(q) = \frac{1}{T_e}\frac{1}{T_c}I_{ethanol+cap}(q) - \frac{1}{T_c}I_{cap}(q) \tag{5.10}$$

$$I_{water}(q) = \frac{1}{T_w}\frac{1}{T_c}I_{water+cap}(q) - \frac{1}{T_c}I_{cap}(q) \tag{5.11}$$

where T_e, T_w and T_c are the transmission values of ethanol, water and the capillary. In Figure 5.8 the scattering profiles of ethanol and water are shown. The scattered intensity from water is constant as it is independent from the scattering vector q in the investigated q-range. In contrary, the scattered intensity from ethanol $I_{ethanol}$ increases with increasing q-value. Scattering from the sample which is a nanoparticle solution can be divided into two parts; in the low q region the SAXS profile is clearly dominated by the scattering from the nanoparticles, whereas at high q-values scattering from the buffer is dominating. Due to the ethanol contribution the scattered intensity from the particle solution is also increasing with increasing scattering vector q. However, the slope of the increase depends on the water-ethanol ratio in the solution. The scattered intensity is considered to be linear in the q interval $0.25\,\text{Å}^{-1} - 0.4\,\text{Å}^{-1}$ and a linear function is fitted to determine the slope of the intensity increase. This is illustrated in Figure 5.9 for different flow rate ratios F_1/F_2, reflecting the water-ethanol ratio. It is assumed that the scattering from the particles in this q-range is neglected. The slope decreases with decreasing ethanol amount with respect to water. In fact, this circumstance can be exploited to determine the weighting factors a and b. To do so, first the slope of the intensity increase of the sample measurement is determined. Then the factors a and b are determined so that the slope of I_{buffer} matches the slope of the sample measurement. The determination of the

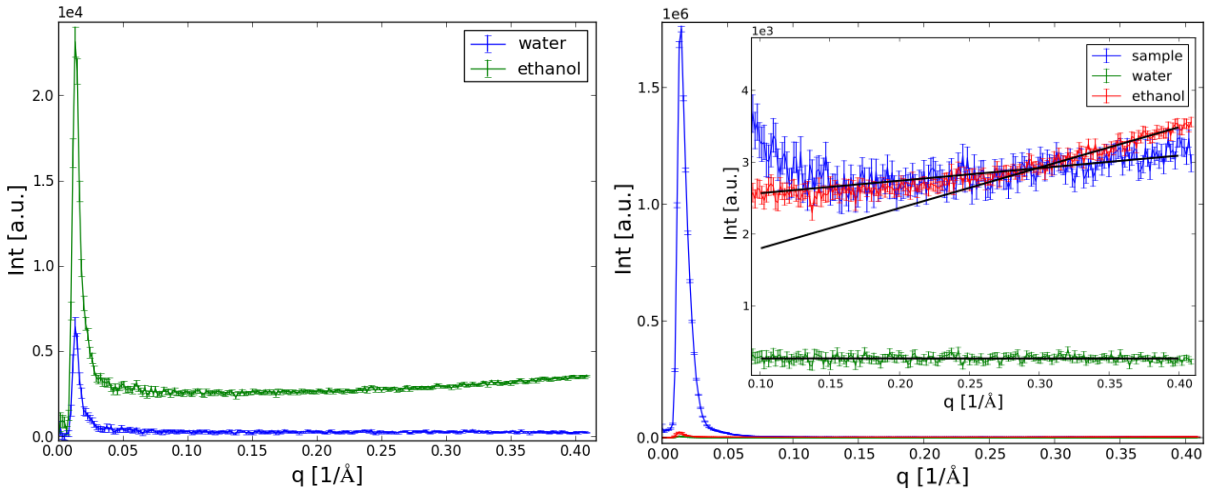

Figure 5.8: SAXS profiles from ethanol and water (left) and additionally from the sample containing nanoparticles (right) shown on linear intensity axis. Scattering intensity from water is constant throughout the observed q range, whereas for ethanol the intensity increases with increasing scattering vector. The scattering intensity from the sample also increases due to ethanol as shown in the insertion. The black lines represent fits of linear functions.

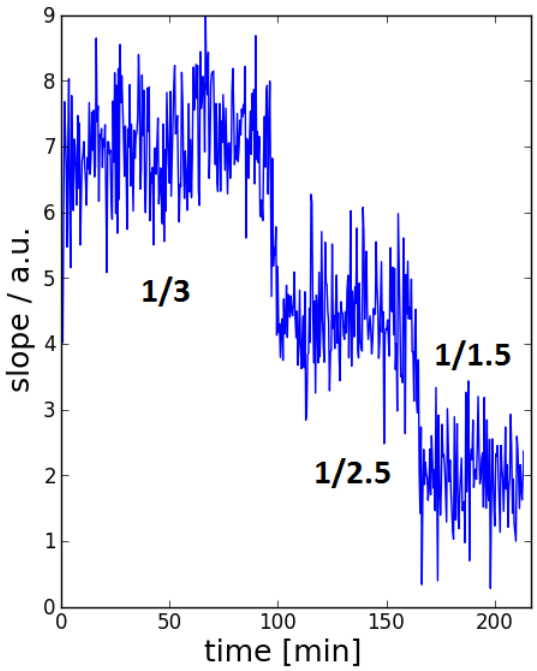

Figure 5.9: Slope of the sample measurement in the q range mentioned in the text for different flow rate ratios $F1/F2$. The procedure to obtain the slope in a time resolved manner is described in section 5.2.3.

factors is achieved by minimizing the square of the difference of the slopes. Finally, when the weighting factors are determined the background correction is performed according

to

$$I_{corr} = I_{sample} - (aI_{ethanol} + bI_{water})\,. \tag{5.12}$$

In Figure 5.10 the resulting corrected sample measurement is shown. After background correction the scattering from the particles is clearly predominant in the q range between $0.014\,\text{Å}^{-1}$ and $0.1\,\text{Å}^{-1}$. By fitting a model function in this q range it is possible to extract the mean radius and the standard deviation of the size distribution. Above $q = 0.1\,\text{Å}^{-1}$ the particle scattering contributon is negligible. Instead, a flat residual background signal is remaining. This backgroud correction method was performed in all real-time monitoring experiments with the aid of self-written Python scripts. However, it is worth noting that

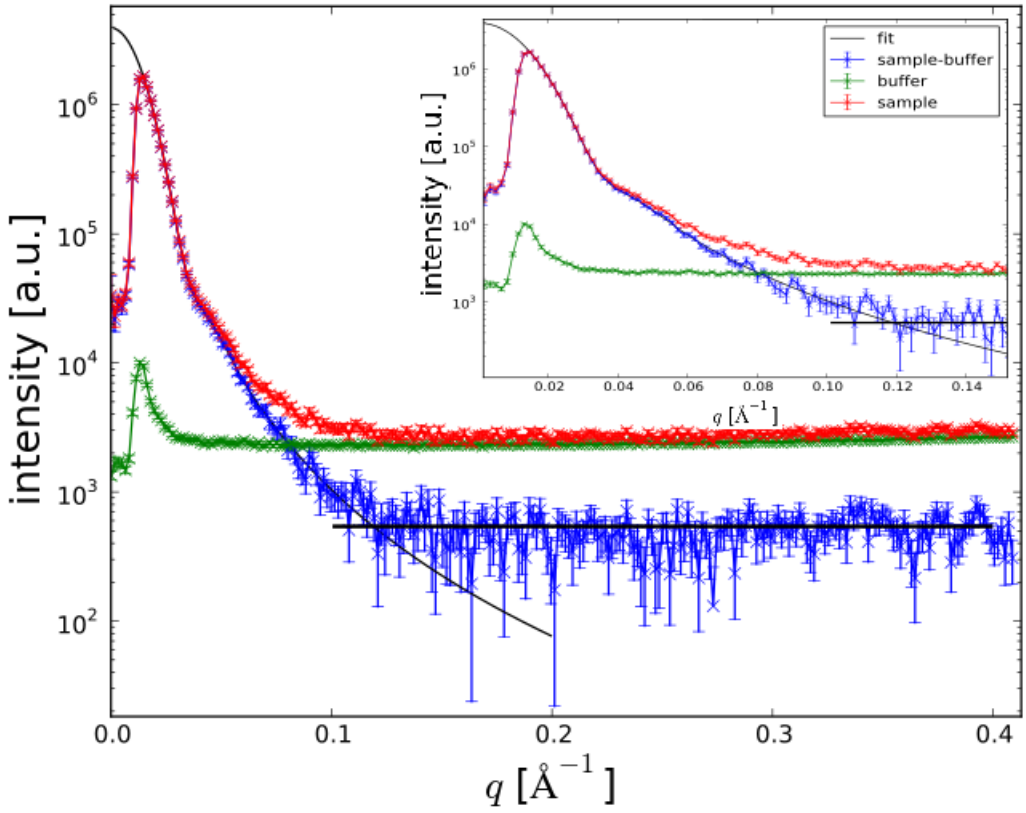

Figure 5.10: Illustration of the background corrected sample measurement.

this method can only be applied if the size and standard deviation of the size distribution are of interest. If however the particle density or the total scattering volume needs to be monitored, a precise knowledge of the transmission values is required, along with the knowledge of the scattering length density contrast between particle and buffer, flux of the direct beam, detector quantum efficiency and the calibration factor for scaling the intensity on the absolute scale.

Data fitting with the least-square method

The fitting of a theoretical model function to the experimental data is achieved by minimizing the chi-squared function χ^2 which represents the mismatch between the model

and the measured data and is given as

$$\chi^2 = \sum_j \left(\frac{\log(I^j_{corr}) - \log(I_{model}(q_j))}{\sigma_j} \right)^2 , \tag{5.13}$$

where I^j_{corr} is the jth measurement point of the background corrected intensity $I_{corr}(q)$ and σ_j the error of $\log(I^j_{corr})$. The model function is given as

$$\log(I_{model}(q)) = c_1 \log(I(R_m, \sigma)) + c_2 , \tag{5.14}$$

where c_1 is a scaling factor and c_2 a offset value. To minimize the χ^2-function the mean radius R_m, the standard deviation σ_R, c_1 and c_2 were varied. In this way the mean radius R_m of the particles in the solution and the standard deviation σ_R of the size distribution were determined. The model function is a non-linear function of R_m and σ_R. To minimize the χ^2-function the Levenberg-Marquard algorithm (LMA) was utilized. In this work an implementation of the LMA algorithm in the programming language Python was used [5].

Validation of the fitting algorithm

To validate the implemented fitting algorithm standard gold nanoparticles with different sizes of R=5 nm, 7.5 nm and 10 nm were purchased from Cytodiagnostics. The three nanoparticle solutions were measured with SAXS. The background correction was performed manually by measuring the transmission values. Model curves with the form factor of a sphere and the Schulz-Zimm size distribution were fitted to the measured data. The corresponding measured curves and the fitted model curves are shown in Figure 5.11. In Table 5.2 the fitting results are summarized for the three measurements. The obtained

give radius [nm]	R_m [nm]	σ_R [nm]
5	5.2	1.0
7.5	7.1	0.7
10	9.4	1.2

Table 5.2: Summary and comparison of the SAXS results to validate the fitting algorithm.

fitting results are in good agreement with the given size values. This shows that the implemented fitting algorithm works correctly and can be used for real-time monitoring. Moreover, significant smearing of the SAXS curve due to finite beam size and multiple scattering is not observable. Therefore, smearing due to finite beam size is neglected in this work. Although multiple scattering is dependent on the sample under investigation it will also be considered as negligible.

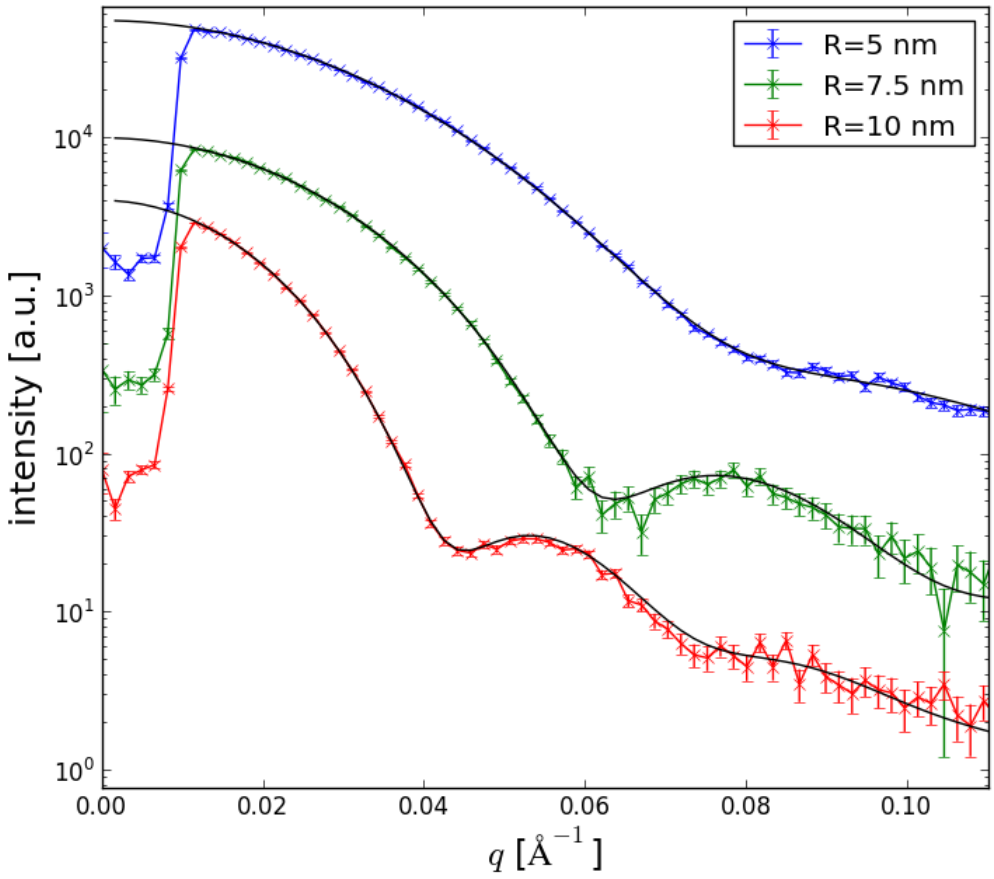

Figure 5.11: SAXS measurement results of standard gold nanoparticles of different sizes of R=5 nm, 7.5 nm and 10 nm.

5.2.3 Production monitoring with SAXS

To achieve real-time monitoring of nanoparticle production, the determination of particle properties such as R_m and σ must be accomplished repetitively in time. While particles transit through the capillary SAXS measurements are performed in time intervals of a certain length. The length of the time interval is determined by the sum of the exposure time and the computing time. The latter is associated with integration of the 2D frame and is approximately 3 s. Typical exposure times in this work are 10 s and 20 s. The process of production monitoring can be divided into the following two major steps:

1. **Generating the raw scattering profile.** Record the 2D frame, perform spatial and floodfield correction, integrate the 2D frame and store the resulting 1D intensity-vs.-q scattering profile in a file.

2. **Determination of particle parameters.** A self-written Python programm opens the latest stored file and performs data reduction according to the procedures described in section 5.2.2. After corrections, a model function is fitted to the measured data to extract information on particle size.

The overall process composed of these two steps is iterated so that acquisition of particle size is performed repetitively. In Figure 5.12 an example of the development of R_m is illustrated. The plot is composed of points $(x, y) = (\text{time}, R_m)$, where each point corresponds to an individual SAXS measurement. The mean radius R_m for each point is obtained by fitting a model function to the corresponding SAXS data. The time difference between two neighbouring points is given by the exposure time plus the computation time. The software allows to monitor additional parameters such as the slope of the intensity increase at higher q values (as illustrated in Figure 5.9). As long as the synthesis conditions remain unchanged the microreactor continuously produces particles of constant size and size distribution. Particle evolution is then represented by a horizontal line. If synthesis parameters are changed, the size will also change. This is indicated by an clear increase or decrease of the R_m evolution curve.

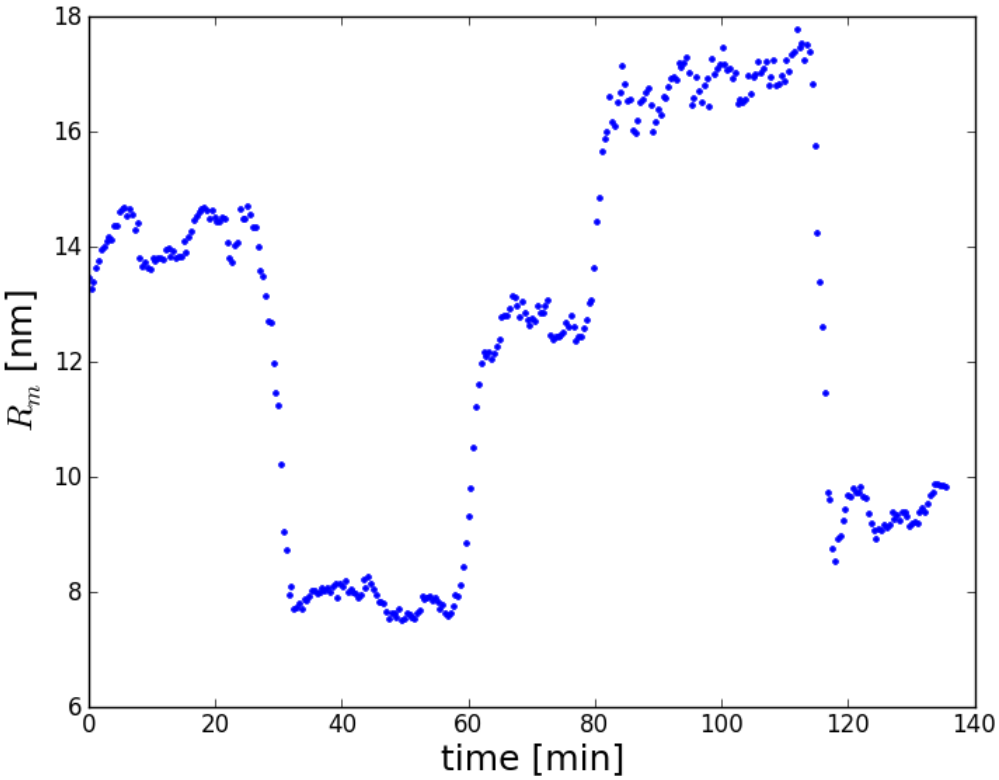

Figure 5.12: Illustration of the developement of the mean radius R_m as a function of time. Upon changing synthesis parameters the size increases or decreases.

During a monitoring experiment it is favourable to see the current particle properties such as size and size distribution inside the capillary in real-time. This was achieved by using a self-implemented graphical user interface (GUI) shown in Figure 5.13. The main feature of the GUI is to display the evolution of the mean radius and the standard deviation of the size distribution in R_m-vs.-time and σ-vs.-time diagrams, respectively. The diagrams are updated each time the two steps are finished and new R_m and σ values are available. The corresponding time value is determined by the creation time of the latest stored 1D data file, from which the new R_m and σ values are determined, minus

the creation time of the first stored file. By this mean the user is able to follow the nanoparticle production nearly in real-time. It enables the user to see effects of synthesis conditions changes during the experiment.

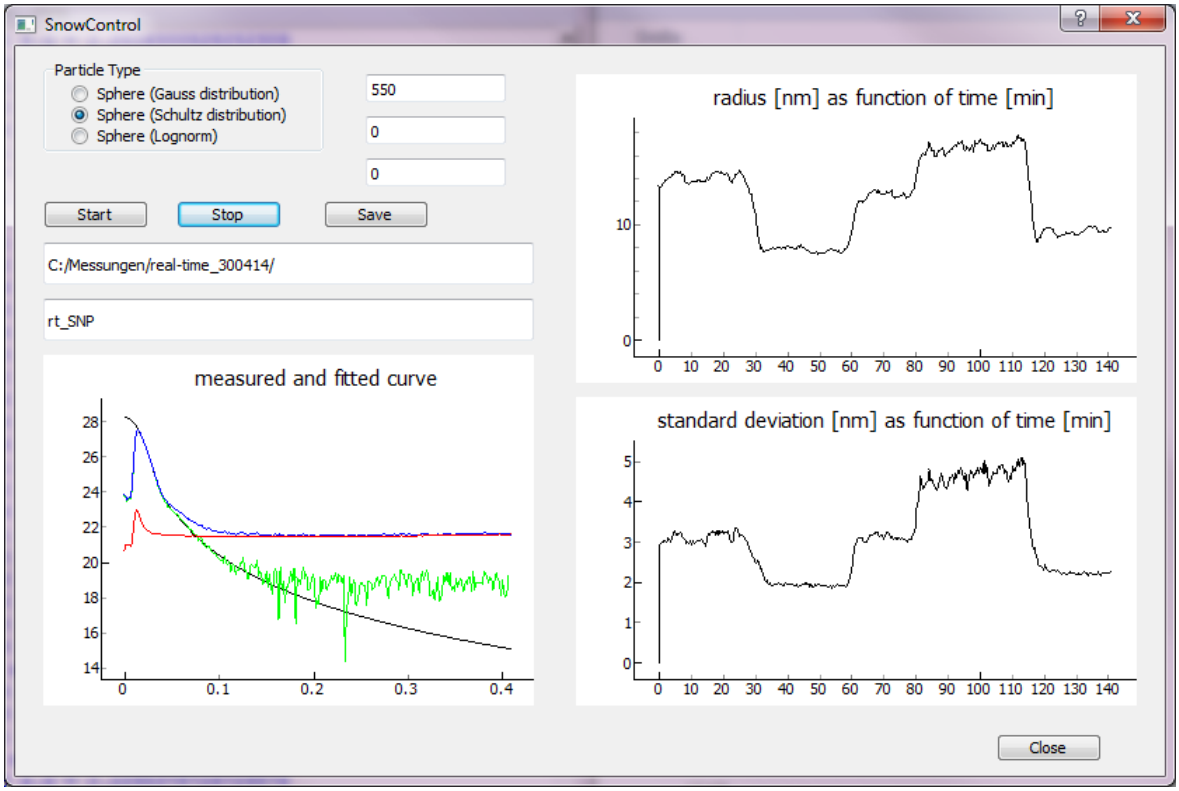

Figure 5.13: Graphical user interface showing the developement of the mean radius and standard deviation. Furthermore, the latest SAXS measurement is displayed including the raw SAXS measurement, the background measurement and the background corrected curve. Furthermore, the user can select between different size distribution functions.

5.3 DLS measurement software

DLS measurements were performed with the aid of Cordouans proprietary software called NanoQ™. All measurements were performed in the so called multiple acquisition mode. This means that a measurement is composed of several single acquisitions. The result of one acquisition is an auto-correlation decay curve and the average over several acquisitions resulst in the so called master curve. The main advantage of performing a multiple acquisition measurement is to increase the signal to noise ratio. However, this method yields reasonable results if the sample remains stable during the entire measurement sequence. If one of the acquisitions is affected by an unstability such as a contamination passing through the capillary, this acquisition can be discarded manually and it doesn't

contribute to the master curve.[6] To obtain the hydrodynamic radius from the measured auto-correlation function the Padé-Laplace algorithm (PLA) [8] is implemented in the software. A function according to equation 3.42 and equation 3.46 is fitted to the measured auto-correlation function by varying the decay rates and weighting factors Γ_n and A_n. To obtain the best fit, the PLA takes into account n exponential decay functions. The decision for the number of decay functions is performed automatically by the software. To each decay rate a corresponding hydrodynamic radius is associated. In all DLS measurements in this work the PLA gave always two hydrodynamic size values.

For illustration, a gold and a silica nanoparticle suspension were measured with DLS and additionally with SAXS. The gold nanoparticles were synthsized in a common batch reaction and provided by KU Leuven. The silica nanoparticles were synthesized with a microflow reactor. In both measurements the DLS fitting procedure of the master curves gave two hydrodynamic diameter. The results are summarized in Table 5.3. Moreover, in both cases the first hydrodynamic diameter value is closer to the mean diameter D_m obtained with SAXS. The deviations of around 8 nm are attributed to the fact that the particles are suspended in water (in case of gold) and in a water-ethanol solution (in case of silica). Therefore, the DLS results also account for the hydration shell around the particles.

particle type	1. D_h [nm]	2. D_h [nm]	D_m [nm]
gold	25.7	177.9	17.2
silica	33.9	102.4	25.8

Table 5.3: Summary of obtained hydrodynamic diameter D_h from the PLA fitting procedure and additional SAXS measurements for comparison.

The lower value is considered to represent the actual hydrodynamic size. The larger value is attributed to larger aggregates or an inaccuracy of the fitting procedure due to noise.

During the experiments in this work it turned out that approximately a measurement time of 1 min for a single acquisition was sufficient in order to obtain a reasonable noise level and good quality of the fit. The measurement time should also not be too long to minimize the risk for falsification of the measured auto-correlation curve due to contaminations flowing through the capillary. In all DLS measurements in this work 5 acquisitions were performed resulting in an overall measurement time of 5 min. Frequently, one single acquisition needed to be discarded due to faulty auto-correlation curve.

[6] As the scattered intensity is proportional to R^6, where R is the radius, even a small amount of aggregated particles could distort the auto-correlation function.

Chapter 6

Experimental results

In this chapter the experimental results are presented and discussed. In the first part of this chapter the influence of different synthesis parameters such as TEOS concentration, flow rate ratio, overall flow rate and reactor temperature on the size, size distribution and particle number density are investigated with SAXS and DLS. A summary and discussion of the results is given at the end of the first part. In the second part of this chapter simultaneous SAXS and DLS measurements are presented.

6.1 Parameters for silica nanoparticle synthesis with the Asia flow chemistry system

Prior to start investigations on the influence of the synthesis parameters, initial parameters must be found. The synthesis parameters are: reactor temperature, TEOS concentration, ammonia concentration, flow rate ratio and the summed flow rate of both pumps. The latter parameter determines the residence time inside the microflow reactor. Then, the initial parameters were used as starting point for further variation and optimization of the parameters. To find a first guess for the initial parameters existing reports on silica nanoparticle synthesis based on the Stöber method were examined.

In [40] silica nanoparticles were synthesized with a self-made microflow reactor. The reactor had two inlets, where in the first inlet a solution of TEOS in ethanol and in the second inlet a solution of ammonia and water in ethanol was injected. The flow rate ratio was fixed at 1/1. The concentrations were [TEOS]=200 mM, [NH_3]=2 M and [H_2O]=26 M. Moreover, the synthesis was performed at room temperature. The resulting particle size was around 750 nm. However, particles of this size are not suitable for SAXS measurements. In batch or semi-batch synthesis of silica nanoparticles it was reported that the particle size decreases with increasing temperature with given concentrations [57, 31].

Ideally, a setup containing three pumps would be preferable to investigate the [H_2O]/[TEOS]

ratio and the $[NH_3]$/[TEOS] ratio by adjusting the flow rates of the three pumps separately. In this work the setup contains two pumps. Therefore, as the first precurser a solution of ammonia in water (ammoniahydroxid NH_4OH) and as the second precursor a solution of TEOS in ethanol was used.

A concentration of $[NH_4OH]$=727 mM of ammonia in water was used and kept constant for all experiment. For preliminary measurements a TEOS concentration of [TEOS]=224 mM was used. Moreover, to increase the chance of getting smaller particles the synthesis was performed at an elevated reactor temperature of 60°C.

In [40] was reported that particles reach their final size after around 30 min. However, a residence time of 30 min is not practicable for finding the right synthesis condition in reasonable time. Therefore, the overall flow rate was chosen to be $F_1 + F_2 = 120\,\mu l\,min^{-1}$. Consequently, the resulting residence time inside the 1000 µl reactor was 8.3 min. This residence time is sufficient as the particles reach around 80 % of the final size after around 8 min according to [40].

For the investigations mostly SAXS measurements were performed. DLS measurements were used to complement the SAXS results. Additional TEM measurements were conducted to support the SAXS and DLS results. The important nanoparticle properties are the mean radius R_m and the standard deviation of the size distribution σ_R. These quantities can be obtained with SAXS and TEM. Furthermore, the relative standard deviation $\frac{\sigma_R}{R_m}$ is used to assess the degree of polydispersity [11]. Additionally, the hydrodynamic radius obtained with DLS is also used.

TEM measurements were performed with a transmission electron microscopy (CM 200FEG Philips) operating at 200 kV. The TEM grids were prepared by placing 8 - 10 µl of particle solution on a carbon-coated copper grid and dried under ambient conditions. No purification was performed before application to the grids. The mean radius and the standard deviation were determined from at least $N = 100$ particles according to $R_m^{TEM} = \frac{1}{N}\sum_i^N R_i$ and $\sigma^{TEM} = \sqrt{\frac{1}{N-1}\sum_i^N (R_i - R_m^{TEM})^2}$, where R_i is the radius of an individual particle.

6.1.1 Influence of TEOS concentration and flow rate ratio

It was reported that in batch reactions the ratio between $[NH_4OH]$ and [TEOS] has an influence on the size of the synthezised nanoparticles [57]. In microflow reactor based synthesis the ratio $[NH_4OH]$/[TEOS] can simply be adjusted by the ratio between the flow rate of the first (ammonia-water solution) and the flow rate of the second pump (TEOS-ethanol solution). Therefore, the flow rate ratio (frr) was varied to investigate the influence on the nanoparticle size.

In this experiment the R1-setup was used. The TEOS concentration was [TEOS]=224 mM. For each frr value the solution was guided from the reactor into the flow-through capillary

and SAXS measurements were performed. The resulting SAXS measurement curves are summarized in Figure 6.1. One can see that the form of the SAXS curves strongly depends

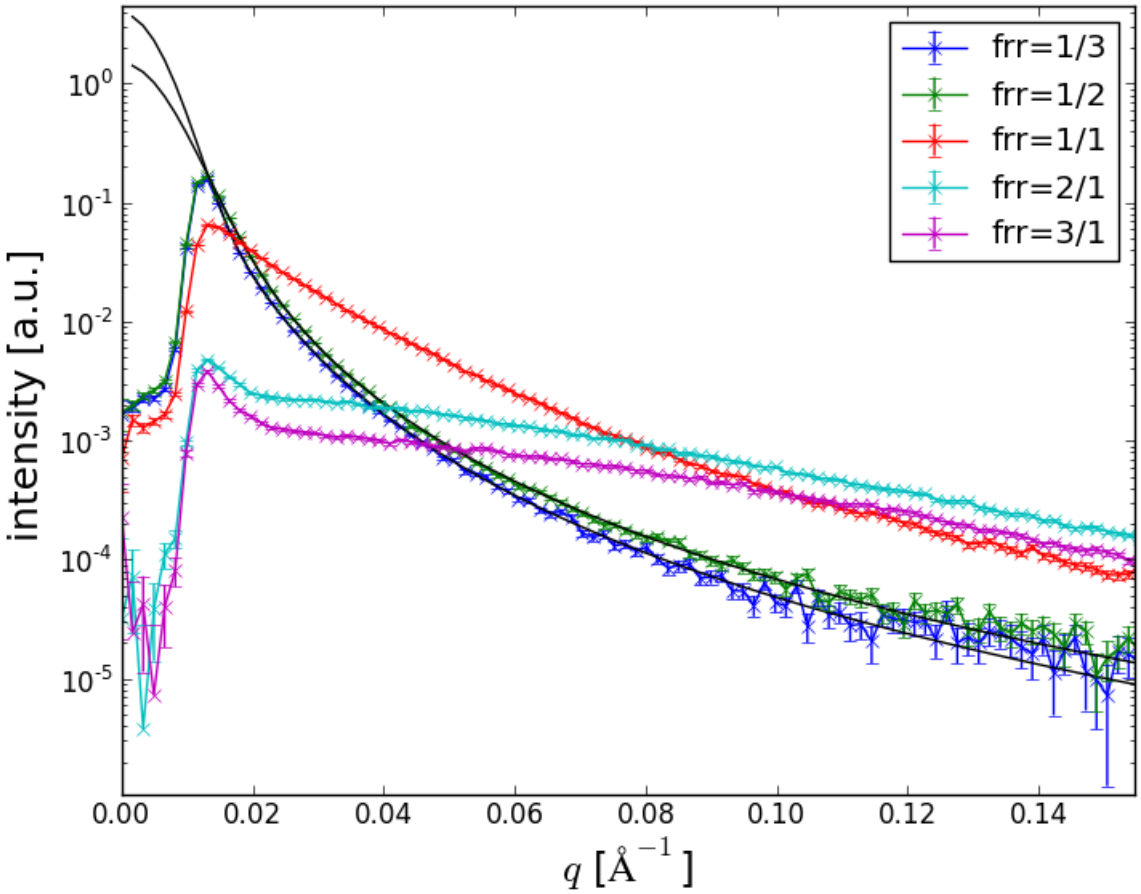

Figure 6.1: SAXS measurements for different frr values with a TEOS concentration of 224 mM and a reactor temperature of 60 °C. For frr values of 1/3 and 1/2 model functions can be fitted assuming a spherical form factor and the Schulz-Zimm size distribution. This indicates particle formation. In contrary, for the other frr values model function with spherical form factor cannot be fitted.

on the frr value. However, only for the frr values of 1/3 and 1/2 a proper model curve can be fitted. In the model a spherical particle shape and a Schulz-Zimm size distribution were assumed. For the other frr values, a spherical form factor with the Schulz-Zimm distribution could not be fitted. This indicates, that for the given reactor temperature and TEOS and ammonia concentrations particles form only for the frr values of 1/3 and 1/2. To verify this SAXS results, additional TEM measurements were performed. For each frr value the nanoparticle solution was guided into an flask. For TEM measurements a few microliters were taken from each flask and applied on a TEM grid, respectively. The TEM measurements were conducted 48 hours after the synthesis. The TEM results are illustrated in Figure 6.2. Indeed, the TEM images show that particles were formed for the frr values 1/3 and 1/2. The TEM images for the other frr values don't indicate nanoparticle formation. Instead, formation of a gel like network is visible. Individual

particles are not formed.

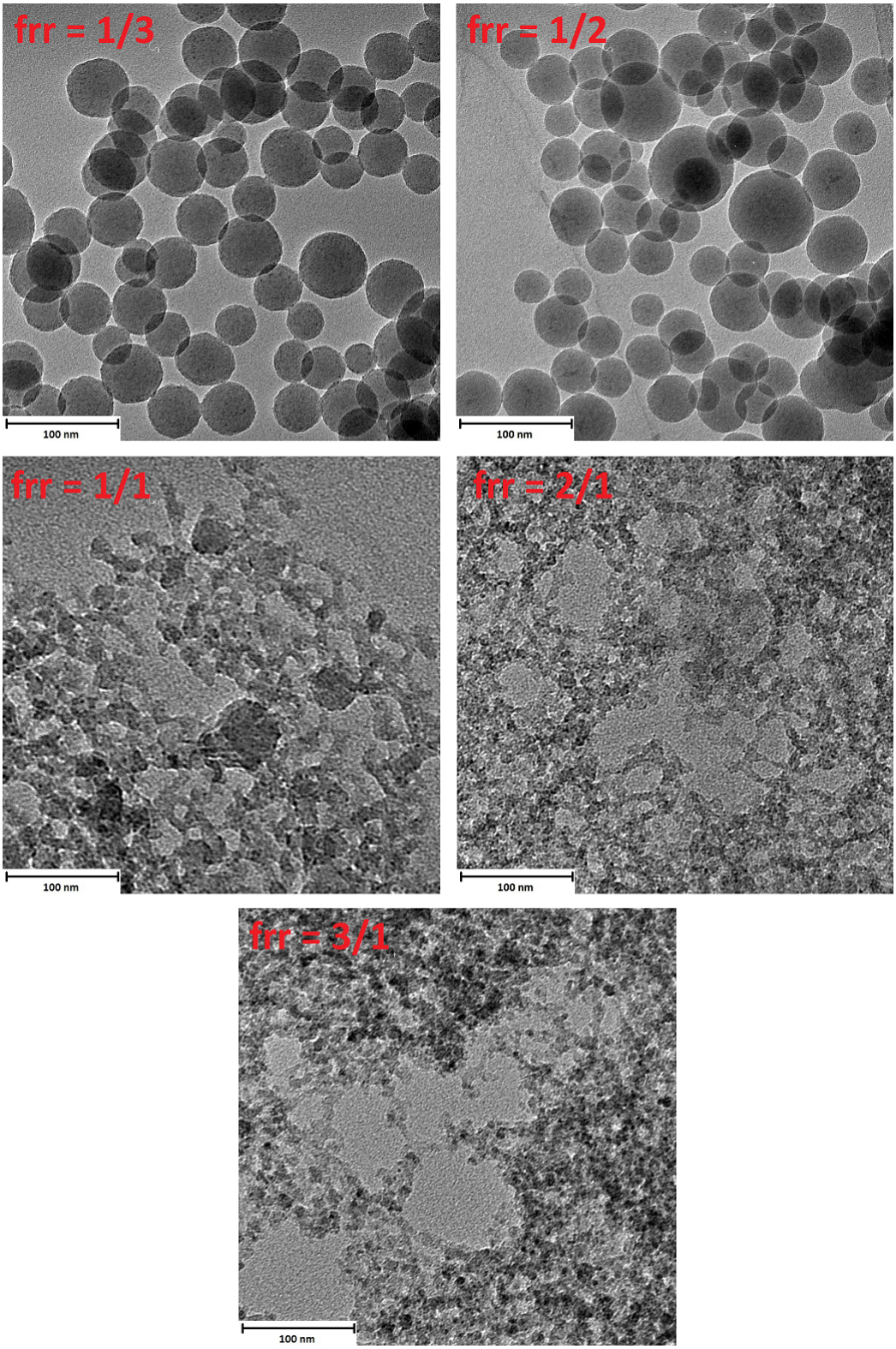

Figure 6.2: Additional TEM measurements of solutions produced with TEOS concentration of 224 mM, reactor temperature of 60 °C and frr values of 1/3, 1/2, 1/1, 2/1 and 3/1, respectively.

Therefore, for further investigations and nanoparticle synthesis only 1/3 and 1/2 as frr values were used. The size results obtained with SAXS and TEM are summarized in Table

6.1. The comparison of the SAXS and TEM results indicates that particles continued to grow after the synthesis. Additionally, it was investigated whether the particle size

	SAXS		TEM	
frr	R_m [nm]	σ_R [nm]	R_m^{TEM} [nm]	σ^{TEM} [nm]
1/3	20.1	6.5	33.0	6.4
1/2	13.2	5.7	31.1	8.8

Table 6.1: Summary of mean radius and corresponding standard deviation values obtained by SAXS directly after the synthesis and TEM after 48 hours after the synthesis.

can be decreased by decreasing the TEOS concentration. For this purpose the TEOS concentration in the TEOS-ethanol solution was lowered from 224 mM to 100 mM, 75 mM and finally 60 mM. The ammonia concentration, reactor temperature and the residence time were kept constant at $[NH_4OH]$=727 mM, 60°C and 8.3 min, respectively. For each TEOS concentration and frr value of 1/3 and 1/2, respectively, SAXS measurements were performed. In Table 6.2 all measurement results are summarized.

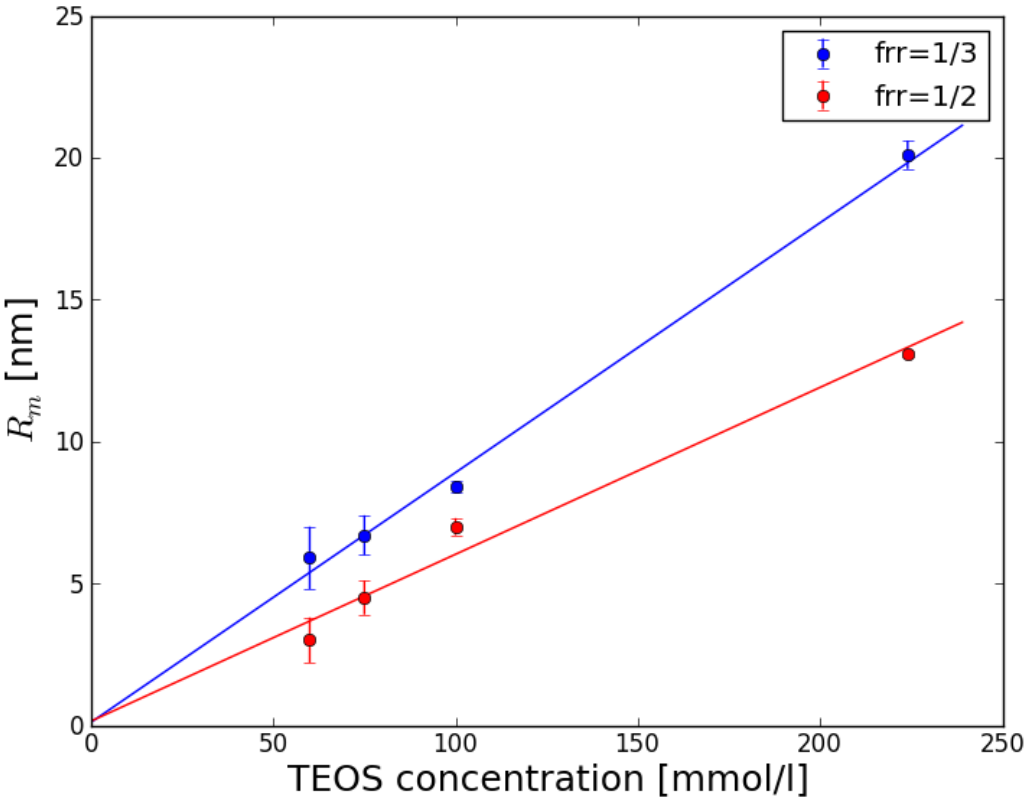

Figure 6.3: The mean radius as function of the TEOS concentration and frr values 1/3 (blue) and 1/2 (red). The mean radius increases with increasing TEOS concentration and increasing TEOS flow rate with respect to the ammonia flow rate.

	frr=1/3			frr=1/2		
TEOS conc. [mmol l^{-1}]	R_m [nm]	σ_R [nm]	$\frac{\sigma_R}{R_m}$	R_m [nm]	σ_R [nm]	$\frac{\sigma_R}{R_m}$
60	5.9	3.5	0.60	2.9	2.3	0.80
75	6.7	3.7	0.47	4.5	3.4	0.76
100	8.4	3.5	0.42	7.0	3.7	0.52
224	20.1	6.4	0.32	13.1	6.1	0.47

Table 6.2: Summary of mean radius, the corresponding standard deviation and the relative standard deviation values obtained by SAXS directly after the synthesis.

In Figure 6.3 the obtained mean radius values as function of the TEOS concentration for the frr values 1/3 and 1/2 are shown. Additionally, linear functions were fitted to the measured values. According to the fitting results the mean radius can be given as function of the TEOS concentration as:

$$R_m^{1/3} = (0.089 \pm 0.004)\frac{\text{nm}}{\text{mmol l}^{-1}} \cdot [\text{TEOS}] + (0.106 \pm 0.545)\,\text{nm}$$
$$R_m^{1/2} = (0.06 \pm 0.01)\frac{\text{nm}}{\text{mmol l}^{-1}} \cdot [\text{TEOS}] + (0.14 \pm 0.87)\,\text{nm}$$

Additional TEM measurements were made from nanoparticle solutions synthesized with [TEOS]=75 mM and frr values of 1/3 and 1/2, respectively. The resulting TEM images are illustrated in Figure 6.4.The size of the nanoparticles were determined from the TEM images in the same manner as in the case of [TEOS]=224 mM. The obtained TEM results are summarized in Table 6.3.

frr	R_m^{TEM} [nm]	σ^{TEM} [nm]
1/3	13.5	4.5
1/2	8.6	2.9

Table 6.3: Mean radius and corresponding standard deviation for [TEOS]=75 mM obtained with TEM.

All in all, with the performed experiments the impact of the frr and TEOS concentration on nanoparticle size were investigated. In the experiments SAXS measurements were performed directly after the nanoparticle synthesis. The obtained SAXS results can be summarized by: the mean radius increases/decreases when the TEOS concentration is increased/decreased. Additionally, the mean radius can be adjusted by varying the flow rate ratio, i.e., by increasing/decreasing the TEOS flow rate with respect to the ammonia flow rate the mean radius can be increased/decreased. By these means, in this experiments the radius was adjusted in a range from approximately 3 nm to 20 nm. Furthermore, the radius values obtained with TEM for [TEOS]=75 mM and [TEOS]=224 mM are larger by around 60 % - 70 % compared to the SAXS results. This indicates a post-reactor growth of

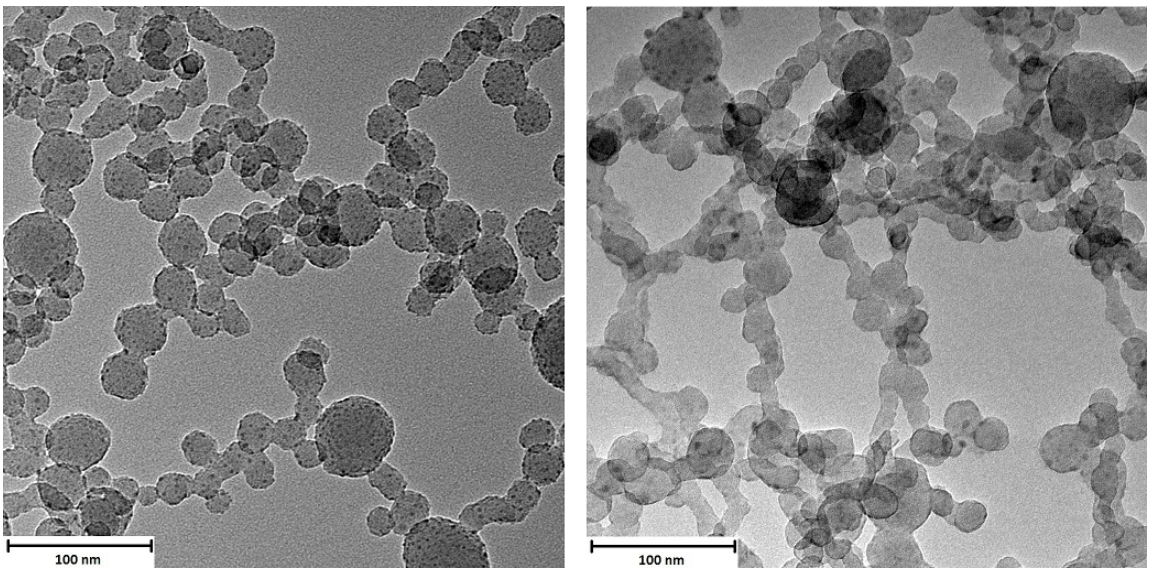

Figure 6.4: TEM measurements of solutions produced with TEOS concentration of 75 mM, reactor temperature of 60 °C and frr values of 1/3 (left) and 1/2 (right)

the nanoparticles. According to this, the expected final mean radii range between around 5 nm and 33 nm.

6.1.2 Influence of temperature

To investigate the influence of the reactor temperature on nanoparticle size, SAXS measurements were performed for several reactor temperature values 60 °C, 55 °C, 50 °C, 40 °C, 30 °C and 25 °C. In this experiment the R1-setup was used. The other synthesis conditions were kept constant at [TEOS]=60 mM, [NH_4OH]=727 mM, $F_1/F_2 = 1/3$ and $F_1 + F_2 = 120\,\mu l\ min^{-1}$. The SAXS measurements are summarized in Figure 6.5. For the SAXS curves measured at 60 °C, 55 °C and 50 °C reactor temperature, a model function could be fitted. In the model a spherical form factor and a Schulz-Zimm size distribution is assumed. The resulting mean radius and standard deviation values are summarized in Table 6.4. However, size values could not be extracted from SAXS measurements performed at 40 °C, 30 °C and 25 °C reactor temperature. Consequently, with increasing size the form factor shifts to smaller q-values. Due to the beam stop, not enough data points at low q-values are available to perfom a proper fit of a model function. However, as the SAXS results from Table 6.4 indicate a size increase with decreasing temperature, it can be assumed that the particle size increases further upon temperature decrease. At 25 °C the mean radius would reach the maximum value in the investigated temperature range. To investigate this, a second experiment was performed. In the experiment DLS measuremets were performed with the VascoFLEX device on the flowing nanoparticle solution for reactor temperatures of 60 °C, 55 °C and 25 °C. More details on simultaneous use and DLS measurements on flowing particles are given in section 6.2.

reactor temp. [°C]	R_m [nm]	σ_R [nm]	$\frac{\sigma_R}{R_m}$
60	6.4	2.7	0.42
55	8.2	3.1	0.38
50	10.8	3.2	0.30

Table 6.4: Summary of the size results obtained with SAXS for the temperatures 60 °C, 55 °C and 50 °C.

Additionaly, TEM measurements were conducted. For TEM measurements for each temperature value the solution was collected in extra flasks after the solution passed through the flow-through capillary.

The obtained auto-correlation functions from the DLS measurements are shown in Figure 6.5. The auto-correlation functions decrease exponentially, which indicates the presence of nanoparticles in the solutions at elevated temperatures as well as at 25 °C. According to the flatter descent of the correlation function at 25 °C, it can be concluded that larger particles are formed at 25 °C. The resulting TEM images are illustrated in Figure 6.6. The TEM images show that particles were formed at 60 °C, 55 °C as well as at 25 °C. A summary of the size values determined with DLS and TEM are summarized in Table 6.5. One can observe a discripancy between the SAXS and DLS results, which results from the fact that DLS measures the hydrodynamic radius as outlined in section 3.3.1. Nevertheless, as a conclusion one can say that nanoparticles were formed for all reactor temperatures in the investigated temperature range 25 °C - 60 °C. Thereby, it was found that a temperature decrease leads to an increase of the nanoparticle size.

	DLS VascoFLEX	TEM	
reactor temp. [°C]	R_h [nm]	R_m^{TEM} [nm]	σ^{TEM} [nm]
60	27.2	12.3	3.1
55	28.3	13.1	3.6
25	115.3	46.1	12.4

Table 6.5: Summary of hydrodynamic radii obtained with the VascoFLEX DLS device and the mean radii and the corresponding standard deviation values obtained with DLS.

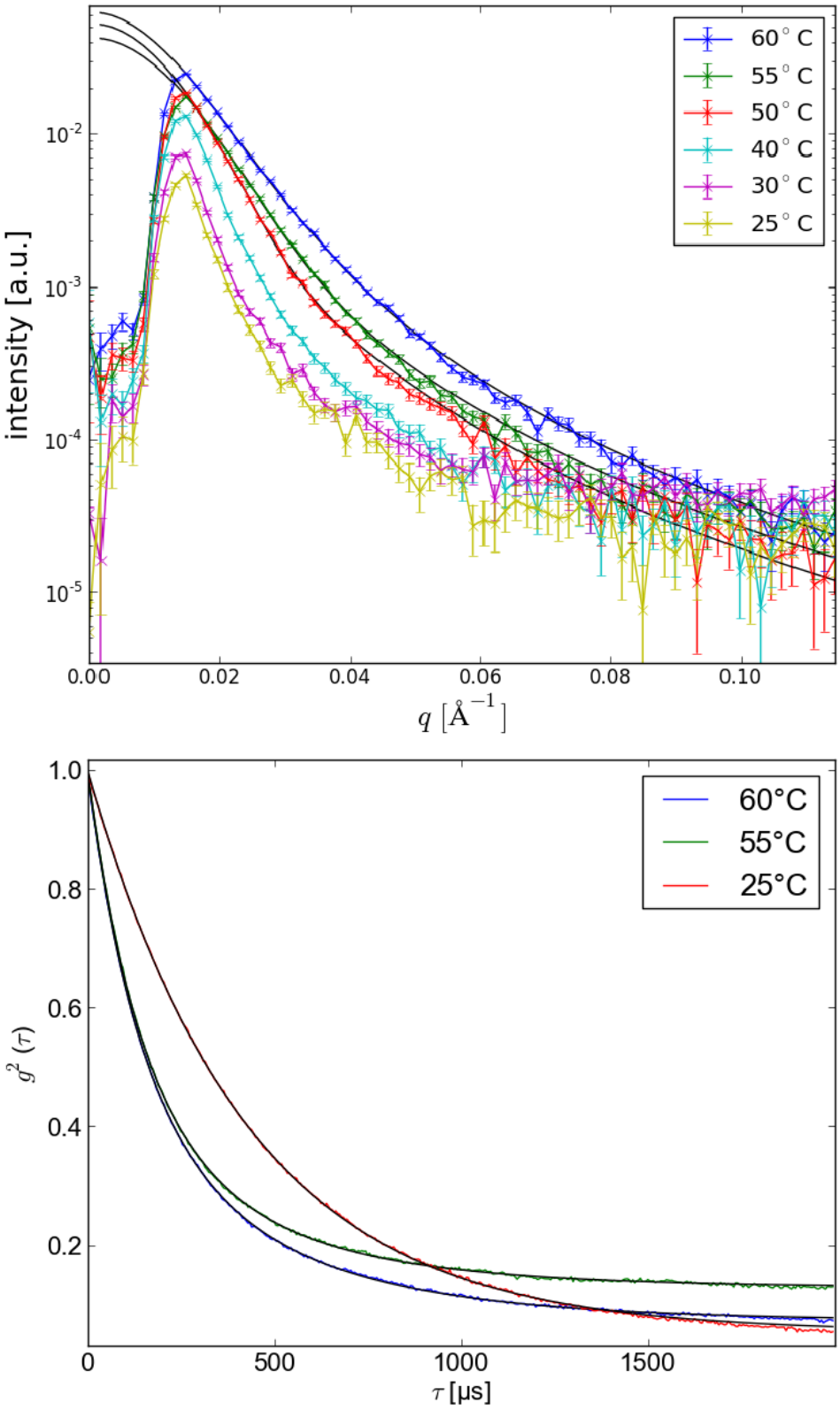

Figure 6.5: Top: SAXS measurements of nanoparticles synthezised with a TEOS concentration of 60 mM, frr values of 1/3 and reactor temperatures in a range from 25 °C to 60 °C. The black lines are the fitted functions. Only for the SAXS measurements at 60 °C, 55 °C and 50 °C functions could be fitted. Bottom: DLS measurements of solutions produced with a TEOS concentration of 60 mM, frr value of 1/3 and reactor temperatures of 60 °C, 55 °C and 25 °C. The black lines are the fitted functions.

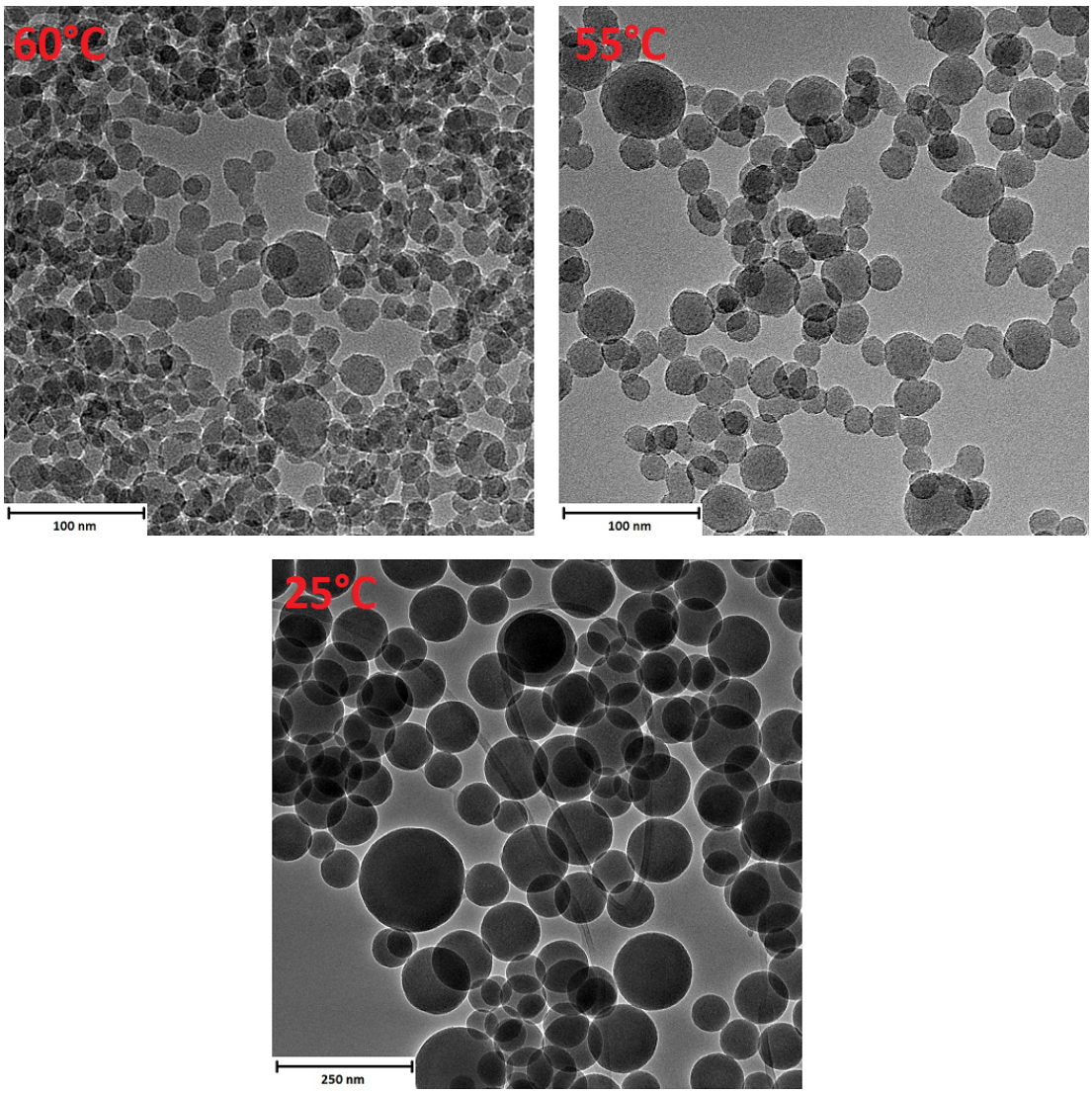

Figure 6.6: TEM measurements on nanoparticles synthesized with [TEOS]=60 mM and different reactor temperatures of 60°C, 55°C and 25°C

6.1.3 Influence of the overall flow rate

As the microflow reactor can be heated one can distinguish between two regions of different temperature: The first is the reactor at elevated temperature and the second is the delay line which is at room temperature. The influence of the residence time inside the heated reactor was investigated. Especially, a shorter residence time compared to the R1-setup (8.3 min) is of interest. For this purpose three experiments were performed.

In the first experiment the overall flow rate was increased to 450 µl min^{-1} to yield a residence time of 2.2 min inside the 1000 µl reactor. The flow rate ratio was set to 1/2 and the reactor temperature to 60 °C. The flow was stopped when the solution reached the capillary. In this way the particle growth was monitored time-resolved and in-situ inside the capillary by performing a SAXS measurement every 20 s with an exposure time of 20 s. The resulting evolution of the mean radius and the standard deviation of the

size distribution are shown in Figure 6.7. As one can see, the mean radius increases with time. In the beginning of the growth process the mean radius rapidly increases. The maximal mean radius of around 12.8 nm is reached after approximately 40 min. The particle growth is accompanied by an initial steep descent of the standard deviation. After 15 min the standard deviation reaches its minimal value of approximately 2.6 nm. After that, the standard deviation slightly increases again by around 0.1 nm till the end of the monitoring process. Consequently, at the end of the growth the relative standard deviation is $\frac{\sigma_R}{R_m} = 0.21$. Indeed, this result is considerably smaller compared to results summarized in Table 6.1 and obtained with the higher residence time of 8.3 min. However, the evolution of R_m and σ_R indicate that the relative standard deviation isn't constant during the growth, but it starts at around 0.57 and decreases to 0.21 at the end of the growth.

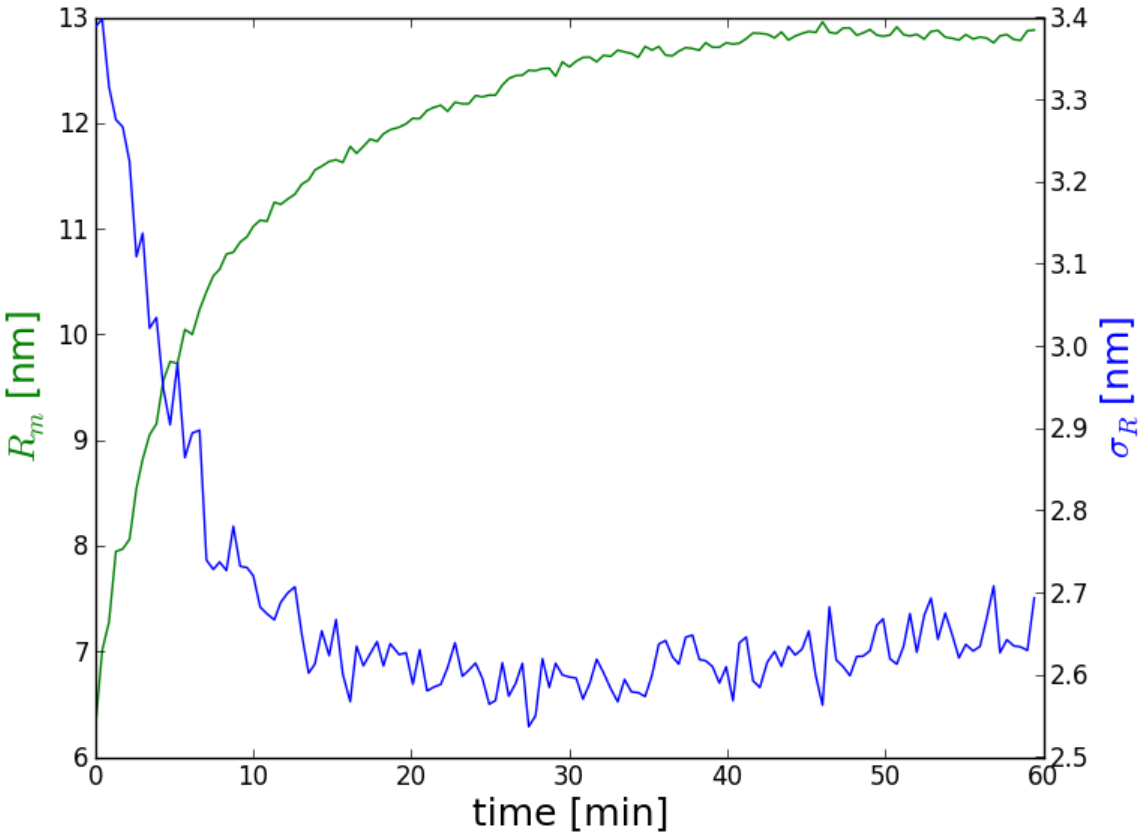

Figure 6.7: Mean radius R_m and standard deviation σ_R as a function of reaction time.

For further investigations on the influence of the residence time the R2-setup was used. The overall flow rate was varied between 72 µl min^{-1} and 125 µl min^{-1}. In this way the resindence time could be adjusted in a range from 2 min to 3.1 min. The delay line served as aging line. As the flow rate was varied to adjust the residence time, the aging time also varied in a range from 14 min to 24 min. Particles arriving in the capillary were considered to be almost grown and the influence of the variation of the aging time on the final size is neglected. From the first experiment, describing the growth inside the capillary, it can

be assumed that after 14 min the mean radius reaches around 90 % of the final size.

In the second experiment a TEOS concentration of 60 mM was used. Different synthesis parameters were used to investigate the influence of the shorter residence time (compared to the R1-setup with 8.3 min residence time) under different synthesis conditions. The synthesis parameters are summarized in Table 6.6. In Figure 6.8 the evolution of the mean radius and the standard deviation determined with SAXS are illustrated. Clear changes of the size and size distribution can be observed due to synthesis parameter changes. In the parameter change sequence $1 \rightarrow 2 \rightarrow 4$ the TEOS flow rate was lowered with respect to the ammonia flow rate. This results in an decrease of the mean radius from approximately 16.5 nm to 11 nm and finally 8 nm. The decrease of the mean radius is accompanied by a decrease of the standard deviation. In the sequence $2 \rightarrow 3$ a temperature decrease from 55 °C to 50 °C is involved, which results in an increase of the mean radius from 11 nm to 14 nm. In the sequence $4 \rightarrow 5$ an increase of the overall flow rate is performed (decrease of the residence time). This results in an increase of the mean radius from 8 nm to 12 nm. In the sequence $6 \rightarrow 7$ the flow rate is lowered again which decreases the mean radius from 17 nm to 9 nm. The relative standard deviation $\frac{\sigma_R}{R_m}$ ranges from approximately 2.0 to 3.0 within the used parameter sets.

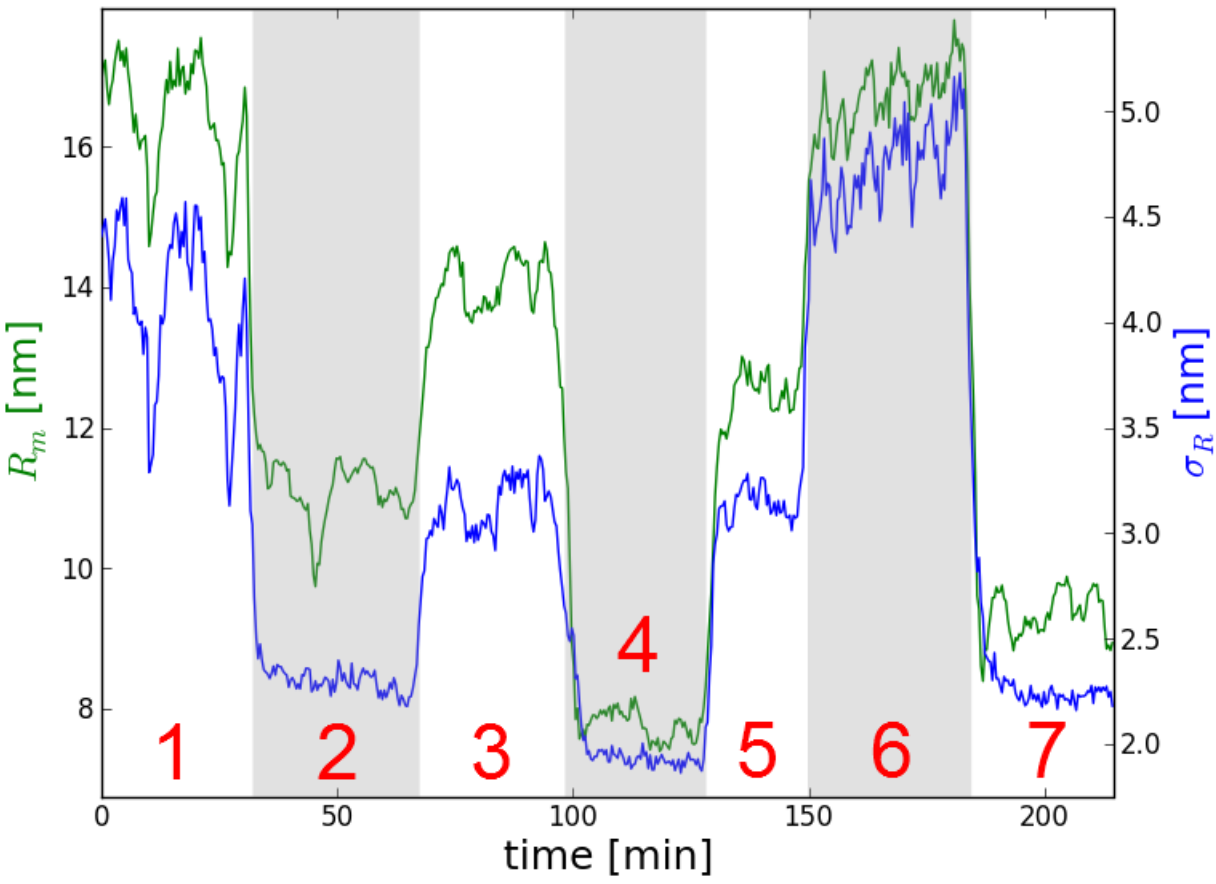

Figure 6.8: Mean radius R_m and standard deviation σ_R as a function of time and different synthesis conditions for a TEOS concentration of 60 mM.

synthesis parameter set number	overall flow rate F_1+F_2 [µl min^{-1}]	frr	reactor temperature [°C]
1	80	1/3	55
2	80	1/2.5	55
3	80	1/2.5	50
4	80	1/1.5	55
5	125	1/1.5	55
6	125	1/2	55
7	72	1/2	55

Table 6.6: Summary of synthesis parameters for silica nanoparticle production with a 250 µl microflow reactor and a TEOS concentration of 60 mM.

In Figure 6.9 TEM images of nanoparticles synthesized with the parameter set number 3 are shown. The images indicate a narrower size distribution compared to the synthesis results with the R1-setup and 8.3 min residence time shown in Figure 6.2, Figure 6.4 and Figure 6.6. The mean radius and the standard deviation of the size distribution were determined form the TEM images resulting in $R_m^{TEM} = 12.6\,\text{nm}$ and $\sigma^{TEM} = 2.1\,\text{nm}$ and a relative standard deviation of $\frac{\sigma^{TEM}}{R_m^{TEM}} = 0.17$.

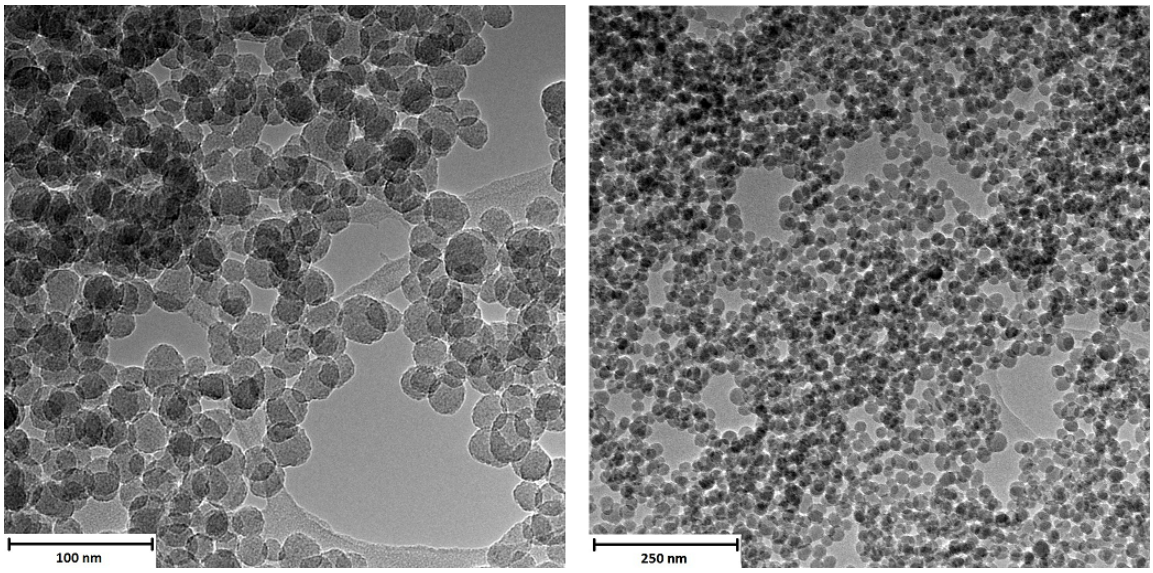

Figure 6.9: TEM images of nanoparticles synthesized with the synthesis parameter set with number 2 and TEOS concentration of 60 mM (left) and a zoom out (right).

In the third experiment the TEOS concentration was 80 mM. Moreover, an exposure time of 10 s for each SAXS measurement was used. In the first part of the experiment the flow rate was continously increased in small steps. In the second part the influence of the reactor temperature and the frr was investigated. The corresponding synthesis parameters are summarized in Table 6.7. The resulting evolution of the mean radius and the standard

deviation is illustrated in Figure 6.10. In the parameter change sequence $1 \rightarrow 7$ the flow rate was systematically increased from 60 µl min^{-1} to 120 µl min^{-1}, whereas the frr value and the reactor temperature were kept constant at 1/2 and 55 °C, respectively. Upon increasing the flow rate up to 110 µl min^{-1} only a slight increase of the mean radius is observable. A further flow rate increase to 120 µl min^{-1} leads to a sharp increase of the mean radius. In the parameter change sequence $8 \rightarrow 9 \rightarrow 10$ the reactor temperature was increased which resulted in a decrease of the mean radius. In the last step $10 \rightarrow 11$ the flow rate of TEOS with respect to the ammonia flow rate is increased, which results in an increase of the mean radius. The relative standard deviation is approximately $\frac{\sigma_R}{R_m} = 0.3$ within the investigated synthesis parameter.

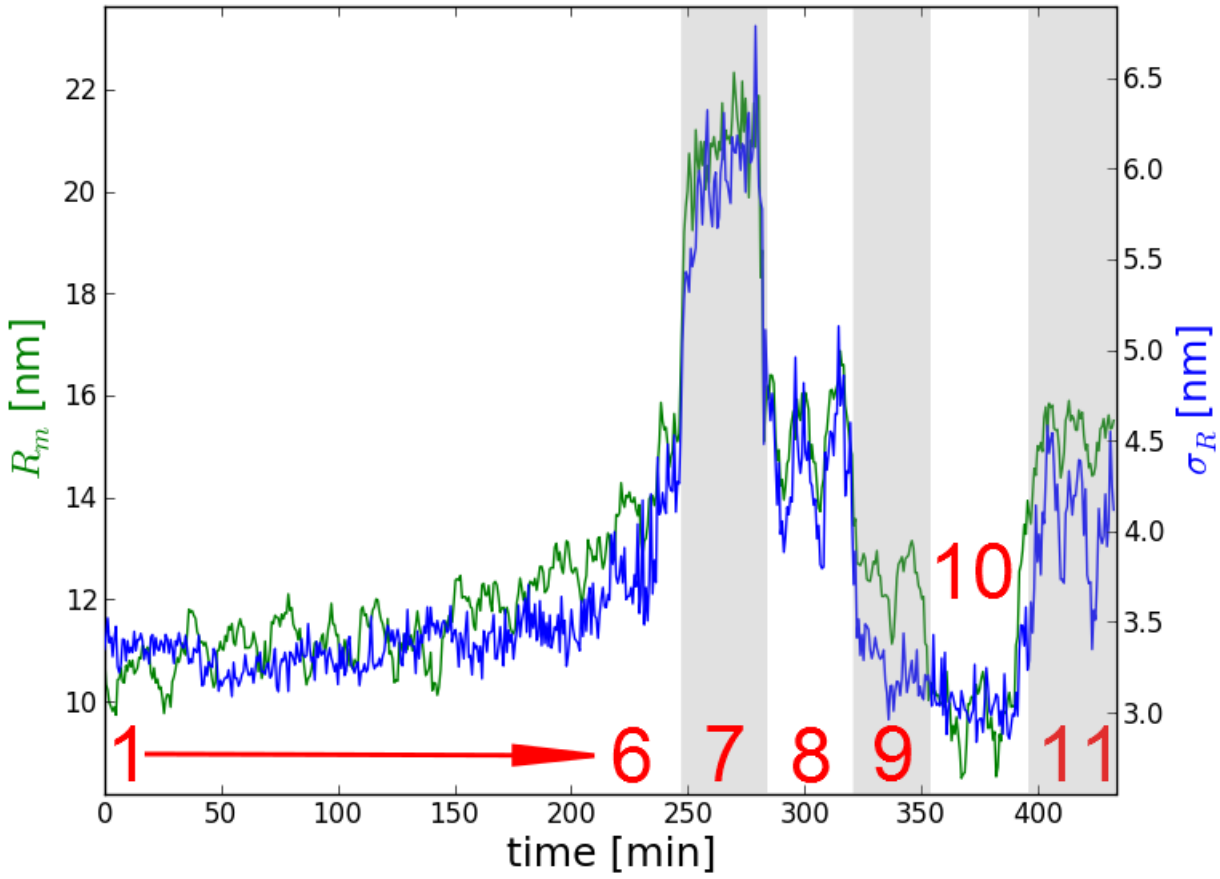

Figure 6.10: Mean radius R_m and standard deviation σ_R as a function of time and different synthesis conditions for a TEOS concentration of 80 mM.

synthesis parameter set number	overall flow rate F_1+F_2 [µl min^{-1}]	frr	reactor temperature [°C]
1	60	1/2	55
2	72	1/2	55
3	80	1/2	55
4	90	1/2	55
5	100	1/2	55
6	110	1/2	55
7	120	1/2	55
8	100	1/2	50
9	100	1/2	55
10	100	1/2	60
11	100	1/3	60

Table 6.7: Summary of synthesis parameters for silica nanoparticle production with a 250 µl microflow reactor and a TEOS concentration of 80 mM.

6.1.4 Impact of the synthesis parameters on particle number density

With the aid of SAXS it is possible to discuss the influence of different synthesis conditions on the particle number density. This will be investigated for the synthesis parameter summarized in Table 6.7. The forward scattering intensity is given as

$$I_0 = I(q \to 0\,\text{Å}^{-1}) = c \cdot \frac{d\sigma}{d\Omega}(q \to 0\,\text{Å}^{-1})\,. \tag{6.1}$$

In the c factor the incident flux, the transmission value and thickness of the sample and the quantum efficiency of the detector are included.[1] Furthermore, for a monodisperse particle solution where each particle has the volume V the differential scattering cross section can be written as [67]:

$$\frac{d\sigma}{d\Omega}(q \to 0\,\text{Å}^{-1}) = nV^2\Delta\beta^2\,. \tag{6.2}$$

However, as the factor c was not determined in this experiment and the scattering length density contrast is unknown, the absolute value of the number density n cannot be calculated. Nevertheless, as long as the flow rate ratio remains unchanged, the scattering length density contrast can be considered as constant. This is the case for the synthesis parameter set numbers 1 - 10. Consequently, the number density is proportional to the quantity $I_0\bar{V}^{-2}$. Moreover, it is

$$\bar{V}^2 = \int_0^\infty D(R, R_m, \sigma_R)V(R)^2 dR\,,$$

[1] The factor c can be determined with the aid of water as reference sample [22].

where $D(R, R_m, \sigma_R)$ is the Schulz-Zimm size distribution. Prior to calculate I_0 the SAXS measurements must be corrected for absorption. To do so, after each SAXS measurement the transmission value was determined. In Figure 6.11 the transmission value T as function of time and different synthesis parameters from Table 6.7 is shown. It can be observed that the transmission value changes when synthesis conditions are varied. For example, when the flow rate is increased (set numbers 1 - 7) the transmission value decreases. In contrary, when the reactor temperature is increased (set numbers 8 - 10) the transmission value remains constant. Finally, when the flow rate ratio is decreased the transmission is also decreasing. In analogy, due to the proportionality of the number density to the quantity $I_0\bar{V}^{-2}$, the number density will follow the same behaviour as $I_0\bar{V}^{-2}$. Therefore, after correcting each SAXS curve for absorption by dividing by the corresponding transmission value the quantity $I_0\bar{V}^{-2}$ was calculated. In Figure 6.12 the quantity $I_0\bar{V}^{-2}$ together with the mean radius as a function of time is illustrated. $I_0\bar{V}^{-2}$ decreases with increasing flow rate (decreasing residence time) and it increases with increasing temperature.

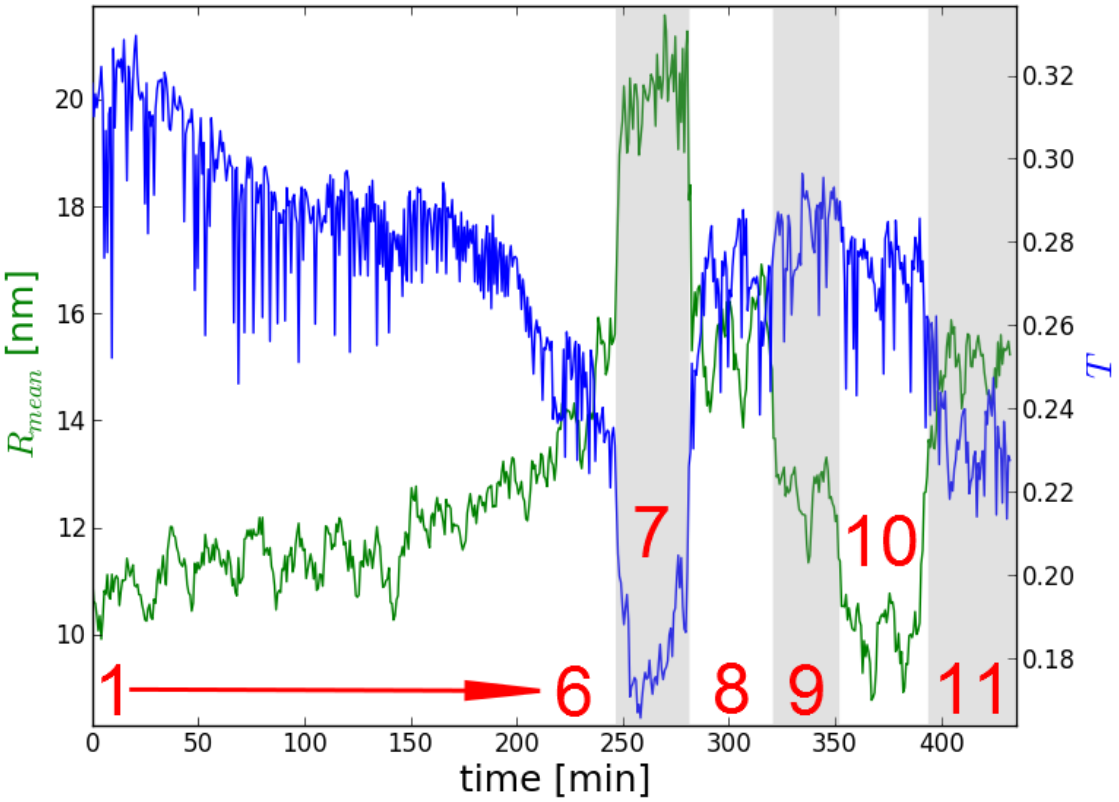

Figure 6.11: Mean radius R_m and the transmission value T as a function of time and different synthesis conditions for a TEOS concentration of 80 mM.

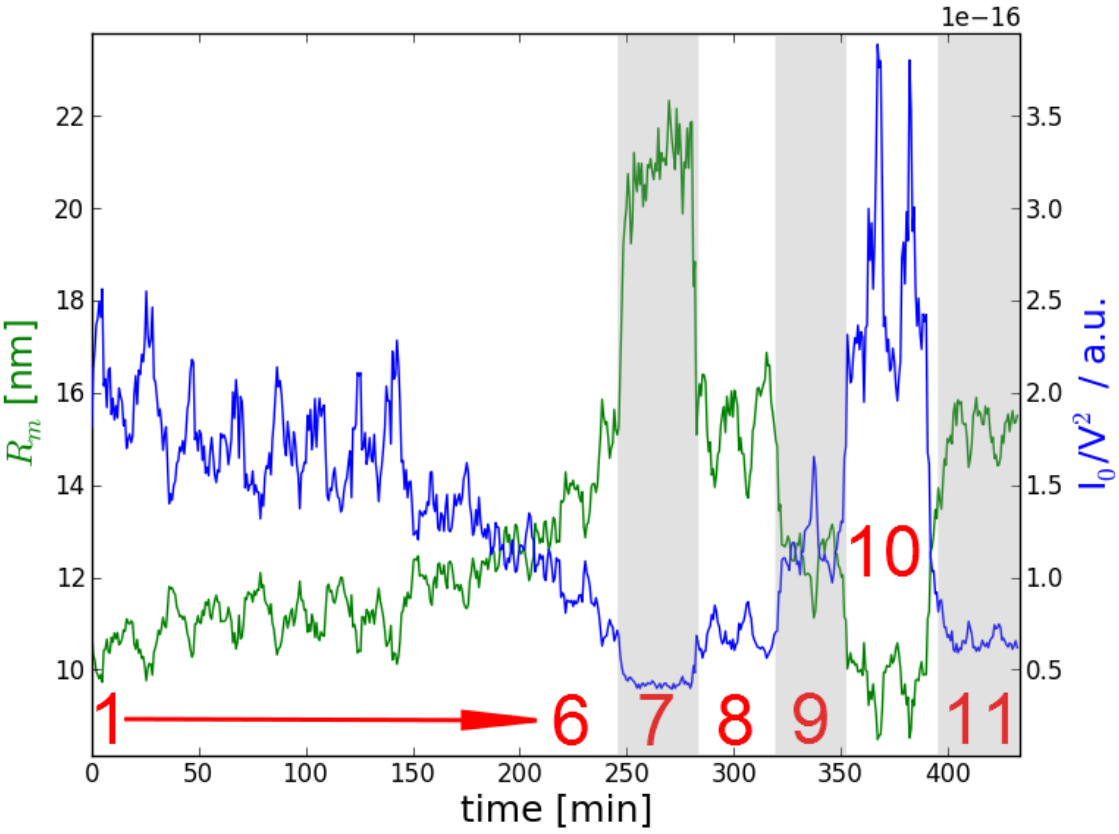

Figure 6.12: Mean radius R_m and the quantity I_0V^{-2} as a function of time and different synthesis conditions for a TEOS concentration of 80 mM.

6.1.5 Summary and discussion of the results

The findings on the influence of the synthesis parameters such as on size, size distribution and number density can be summarized as following:

1. **Influence of the flow rate ratio**: An increase of the flow rate of the TEOS-ethanol solution with respect to the flow rate of the ammonia-water solution (this is associated with a decrease of the $[NH_4OH]/[TEOS]$) leads to an increase of the mean radius.

2. **Influence of the reactor temperature**: An increase of the reactor temperature results in a decrease of the mean radius. The size decrease is accompanied by an increase of the particle number density.

3. **Influence of the residence time**: A decrease of the residence time leads to an increase of the mean radius. This is accompanied by an decrease of the particle number density.

According to the LaMer-Dinegar model, nanoparticle formation and growth is initiated after reaching a certain monomer supersaturation level, after which initial nuclei are formed. In the course of the synthesis the nuclei grow through continous addition of monomers to their surface. The final size of the particles is determined by the amount of the initial nuclei and the concentration of TEOS. For example, if a high amount of nuclei is formed, less TEOS is left for conversion into monomer and thus for further particle growth. The resulting nanoparticle suspension will exhibit a high particle number concentration. But the average particle size will be rather small.

The amount of initial nuclei is determined by the monomer supply rate. At a higher supply rate the critical supersaturation level is reached faster and the nuclei formation starts earlier. The duration of the nucleation phase is crucial for the final size, size distribution and particle number density [57]. If the nucleation phase is short all nuclei are produced at approximatelly the same time. Therefore, a short nucleation phase produces nanoparticles with a narrow size distribution [57, 31]. In contrary, if the nucleation phase is long, nuclei are produced at different times leading to a broader size distribution at the end of the growth phase. Furthermore, the duration of the nucleation phase affects the mean particle size and particle number density. At a short nucleation phase the mean size increases, whereas the particle number density decreases since less nuclei are formed.

In [57] it was reported that the ammonia amount has an impact on the hydrolysis reaction. At higher ammonia amount the hydrolysis and thus the monomer addition rate is accelerated compared to lower ammonia amount. Thus, increasing the ammonia amount can lead to an increase of the nuclei number, and consequently to a higher particle number density. Additionally, this would result in smaller particles at the end of the growth process. This could explain the first finding. However, in the increase of the

frr a decrease of the TEOS flow rate and thus TEOS amount is involved. Therefore, the particle size decrease can also stam from the lower TEOS amount. Consequently, to investigate the influence of the ammonia amount further measurements with systematic variation of the ammonia amount at constant flow rate ratio and TEOS amount would be neccessary.

According to the classical nucleation theory of homogeneous nucleation the nucleation rate r as function of the temperature T is given as [60]

$$r = \rho Z j \exp(-\Delta F/kT)\,, \tag{6.3}$$

where ρ is the number density of the monomers, j is the upper bound of the rate at which a monomer attaches to the surface of a nucleus, Z is the Zeldovich factor giving the propability that a formed nucleus doesn't dissolve again, k is the Boltzman constant. Finally, ΔF is the free energy barrier of nucleus formation. According to equation 6.3 a temperature increase results in an increases of the nucleation rate. At higher temperatures more nuclei are formed which leads to a higher particle number density at the end of the growth phase. At the same time, the mean size is lower, since at a given monomer amount the monomers are predominantly used for nuclei formation instead for growth. This could explains the second finding.

Finally, the residence time influences the mean particle size and the particle number density as shown in Figure 6.12. These findings indicate that the residence time affects the duration of the nucleation phase. A temperature decrease leads to an decrease of the hydrolysis and condensation rate [16]. When the solution exits the first microflow reactor, it is cooled down in the delay line. Due to the cooling of the solution to room temperature the monomer supply rate gets damped. Hence, the monomer supersaturation level descent is accelerated and the duration of nucleation phase is shortened. However, this requires that the condensation rate is less affected by the temperature decrease. The experimental results obtained with the R2-setup indicate that the net-effect of shortening the residence time inside the heated reactor is a shortening of the nucleation phase. This is concluded from the result that the mean radius increases while the number density decreases when decreasing the residence time. Moreover, at short nucleation phase a narrow size distribution is expected according to the LaMer-Dinegar model. Indeed, the comparison of TEM images and size results obtained with TEM between the R1-setup and R2-setup experiments indicate that the size distribution is narrower for the shorter residence time.

With the measurement performed on silica nanoparticle while production, the capability of the NanoSTAR device and the implemented software of performing real-time monitoring was shown. With the aid of the developed experimental setup it is possible to follow trends and changes of the size which arise from adjustments of the synthesis parameters. In this way the influence of different synthesis conditions can be investi-

gated and synthesis parameters can be optimized. An exposure time for an individual SAXS measurement of 10 s was reached. By using DLS simultaneously and probing the same capillary facilitated to investigate the influence of the reactor temperature on the nanoparticle size.

6.2 Simultaneous SAXS and DLS measurements

6.2.1 Simultaneous SAXS and DLS measurements at stopped nanoparticle flow

Simultaneous SAXS and DLS measurements were perfomed on nanoparticles synthesized under different synthesis conditions. For the synthesis the R1-setup was used. The synthesis parameters are summarized in Table 6.8. The reactor temperature was 60°C. For each synthesis parameter set the nanoparticle solution was guided through the capillary, then collected in a flask. The capillary was aligned vertically as shown in Figure 5.5. The collected nanoparticle solution was then used for additional TEM and DLS measurements. The additional DLS measurements were performed on a standard stationary DLS Vasco (from Cordouan) device to validate the results obtained with the VascoFLEX device.

synthesis parameter set number	overall flow rate F_1+F_2 [µl min^{-1}]	frr
1	120	1/3
2	120	1/2
3	120	1/1.5
4	40	1/2

Table 6.8: Summary of synthesis parameters for silica nanoparticle production with a 1000 µl microflow reactor and a TEOS concentration of 75 mM for simultaneous SAXS and DLS measurements.

For each measurement and systhesis parameter set the flow was stopped and SAXS and DLS measurements were performed simultaneously. The DLS measurement time was 5 minutes, whereas the SAXS measurement time was 20 seconds for each synthesis parameter set. The obtained results are summarized in Table 6.9.

All size results follow the same trends: when the mean radius obtained with SAXS decreases, the hydrodynamic radii and the TEM results also decrease. In set number 4 the overall flow rate was decreased which resulted in an increase of the residence time up to 25 min inside the 1000 µl reactor and 11 min inside the delay line. The particles were fully grown when they reached the capillary. Therefore, the SAXS and TEM results give approximately the same values. Comparing the SAXS and TEM results for the set num-

set	SAXS		DLS VascoFLEX	DLS Vasco	TEM	
number	R_m [nm]	σ_R [nm]	R_h [nm]	R_h [nm]	R_m^{TEM} [nm]	σ^{TEM} [nm]
1	6.1	3.7	17.7	15.4	13.5	4.5
2	5.2	2.7	12.3	14.8	8.6	2.9
3	3.2	1.6	9.3	8.5	—	—
4	9.4	3.6	14.6	15.4	9.8	4.4

Table 6.9: Summarized size values obtained by SAXS, DLS and TEM. The DLS measurements with the VascoFLEX device and the SAXS measurements were performed simultaneously. After the synthesis additional TEM and DLS measurements were performed.

bers 1 - 3 indicates that particles continued to grow after passing through the capillary. Consequently, the DLS VascoFLEX measurements were performed while ongoing growth of the particles inside the capillary. As the DLS Vasco measurements were performed several hours after the synthesis, larger values compared to the DLS VascoFLEX measurements were expected. However, both DLS results are rather similar. The reason for this might be that dynamics related to the growth process interfered with the diffusion dynamics and caused the particles to appear larger then their actual size.

6.2.2 DLS measurements on flowing nanoparticles

A substantial prerequisite for monitoring the production of nanoparticles with DLS is the ability to measure flowing nanoparticles, i.e., diminish or eliminate flow related dynamics with respect to diffusion dynamics. This is possible under following conditions [20]:

1. small scattering volume with respect to the capillary diameter
2. low flow rates
3. scattering vector and flow velocity are perpendicular to each other $\mathbf{q} \cdot \mathbf{v} \approx 0$ to minimize the Doppler frequency shift.

Flow dynamics are associated with a velocity gradient perpendicular to the longitudinal axis of the flow-through capillary due to Poiseuille flow. If the first and the second condition are fulfilled the particles in the scattering volume under investigation are in a homogeneous velocity field and the gradient can be approximated to be zero. Furthermore, the transition through the scattering volume can be considered as much slower then the diffusion at sufficient low flow rates. The condition $\mathbf{q} \cdot \mathbf{v} \approx 0$ is achieved by a proper alignment of the capillary described in section 5.2.1.

DLS measurements on gold nanoparticles were performed at different flow speeds to test whether the above described conditions are fullfilled for the VascoFLEX DLS device and the flow-through capillary. The gold nanoparticles were provided by KU Leuven and

were synthesized in a commonly used batch reaction. The gold nanoparticle solution was kept inside the batch for 24h to complete all reaction and growth processes. The gold nanoparticles were suspended in water and were not functionalized.

To achieve a flow the particles were filled into a flask and one of the syringe pumps was used to pump the particle solution through the capillary. The results were compared with measurements performed with a second Vasco DLS device available at KU Leuven which measures particles in stationary mode, i.e., without flow. All results are summarized in Figure 6.13. At zero flow 6 measurements, each yielding a hydrodynamic diameter,

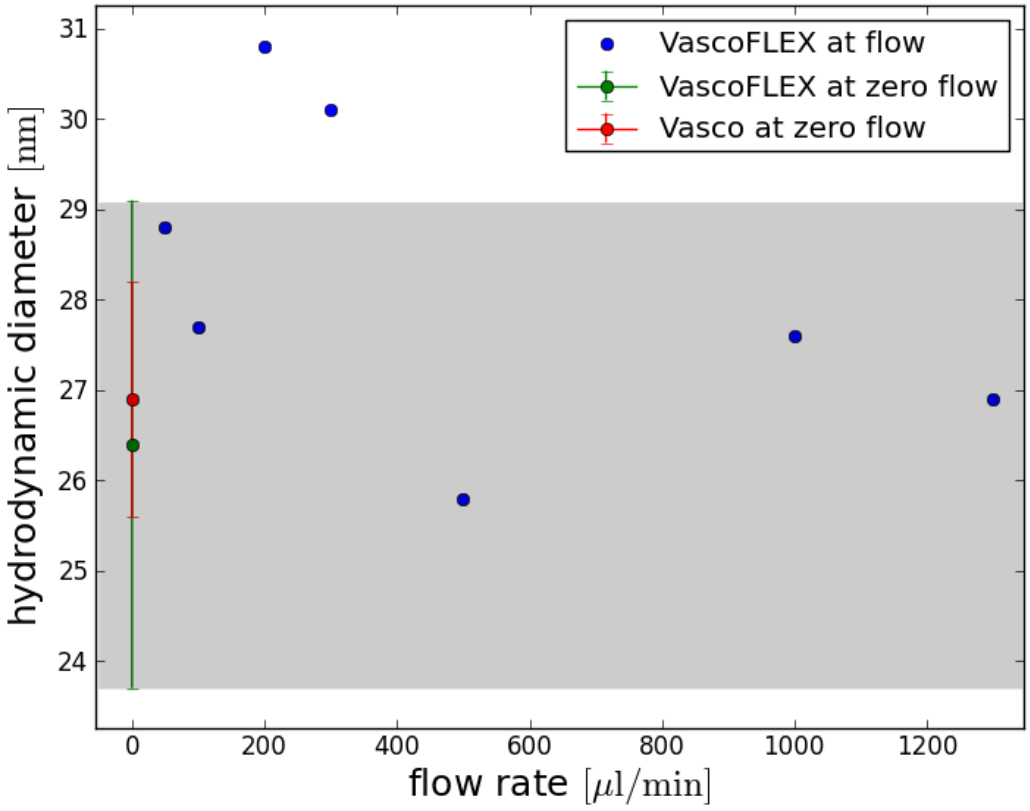

Figure 6.13: Illustration of the hydrodynamic diameter for zero flow and different flow rates obtained with the Vasco and the VascoFlex device.

were performed with the VascoFlex and the Vasco device, respectively. Then, for each of the two devices the mean hydrodynamic diameter was calculated according to $\bar{D}_m = \frac{1}{N}\sum_{i=1}^{N} D_i$ where $N = 6$, resulting in $\bar{D}_m^{VF} = 26.4 \pm 2.7\,\text{nm}$ and $\bar{D}_m^{V} = 26.9 \pm 1.3\,\text{nm}$ for the VascoFlex and the Vasco device, respectively. The corresponding error is chosen to be the standard deviation $\sigma = \sqrt{\frac{1}{N-1}\sum_{i=1}^{N}(D_i - \bar{D})^2}$. In contrary, measurements at flow were performed only once. Up to a flow rate of $1300\,\mu\text{l/min}$ reasonable hydrodynamic diameter values can be obtained. It can be assumed that the Vasco zero-flow measurement yields the most accurate result with the lowest error. To each hydrodynamic diameter measured in flow, the error of the Vasco zero-flow measurement can be assigned. This leads to the conclusion that all flow measurements are in good agreement with the zero-flow measurements within the error bars. A further increase of the flow rate becomes

noticeable as a gradual deformation of the auto-correlation curve as illustrated in Figure 6.14. One can observe oscillatory behaviour over the entire τ range accompanied by an increase of the slope at low τ values. From these curves hydration diameters cannot be extracted. Additionally, the gold nanoparticles were measured with SAXS as shown

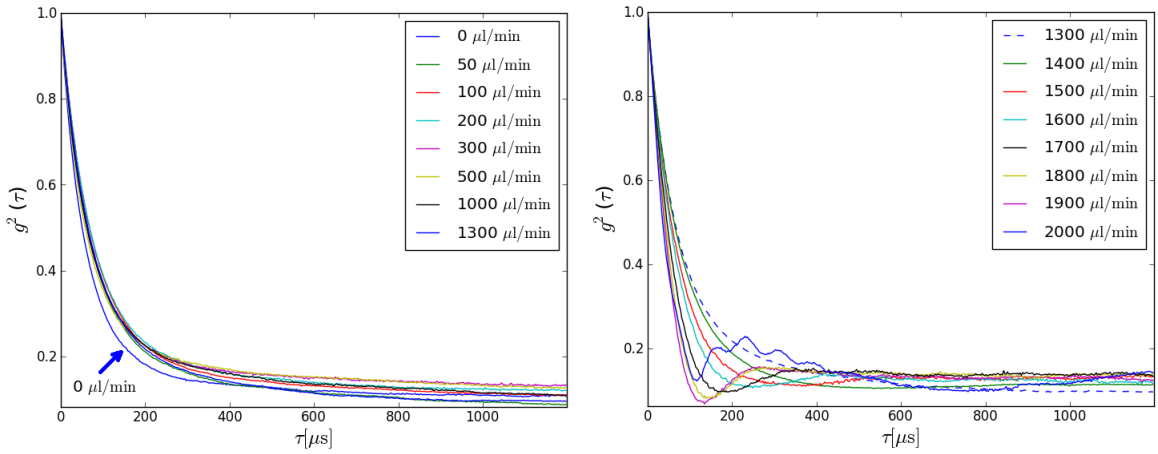

Figure 6.14: Illustration of auto-correlation functions for different flow rates.

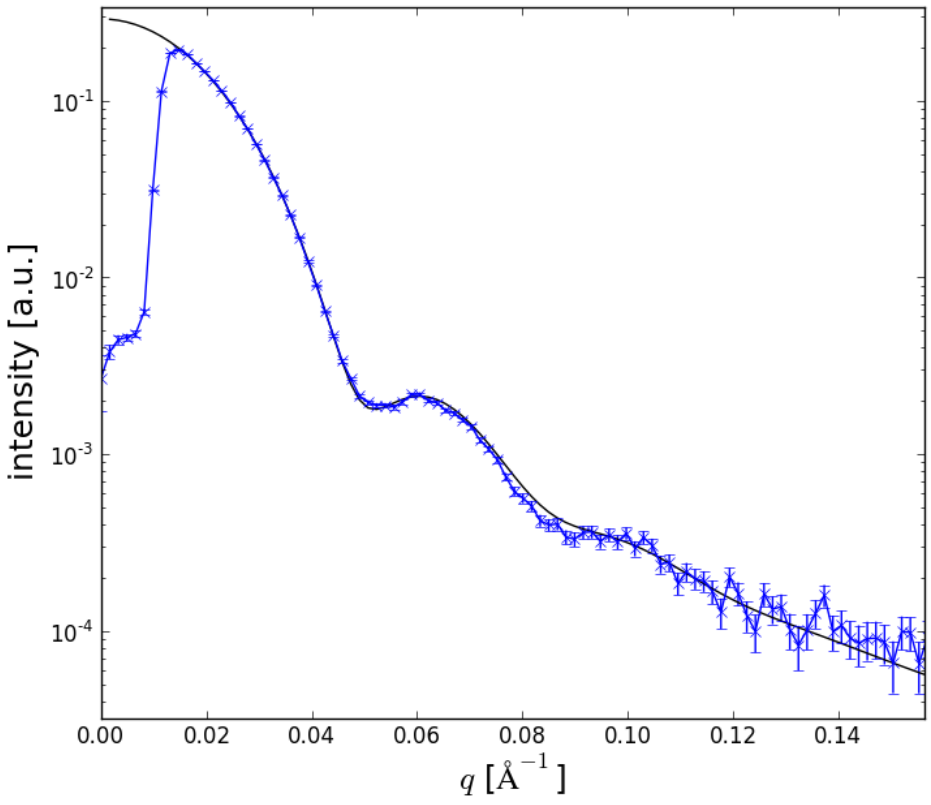

Figure 6.15: SAXS measurement of the gold nanoparticles performed simultaneously with DLS. The solid curve represents the model function fit.

in Figure 6.15 yielding a mean diameter of $D_m = 17.2\,\text{nm}$ and a standard deviation of $\sigma_D = 2.2\,\text{nm}$. The relative standard deviation is $\frac{\sigma_D}{D_m} = 0.13$. The deviation of around 10 nm between the DLS and SAXS results indicates a hydration shell around the particle.

These results show that characterization of flowing nanoparticles with DLS is feasible with the VascoFlex and the used flow-through capillary. These results allow DLS measurements to be performed simultaneously with SAXS. In turn, this makes it possible to monitor nanoparticle production with SAXS and DLS simultaneously and use SAXS and DLS as complimentary probe techniques.

Chapter 7

Summary and conclusions

In the presented work a real-time monitoring of nanoparticle production was realized. This achievement bases on two major implementations. Firstly, a microflow reactor based synthesis station for nanoparticle synthesis was connected to a SAXS (NanoSTAR from Bruker AXS) and a DLS device (VascoFLEX from Cordouan Technologies). Secondly, the NanoSTAR was optimized in terms of flux at the sample position to reduce the exposure time and, thus, increase the sampling rate of the monitoring process. To measure the produced nanoparticles coming from the microreactor a dedicated flow-through capillary was fabricated and connected to the outlet of the reactor. The flowing nanoparticles were measured with SAXS. For automated SAXS data processing, a dedicated software was implemented. The software also includes a graphical user interface which allowes to track the nanoparticle properties such as size and size distribution while ongoing flow and production of the nanoparticles. An exposure time of around 10 s for an individual SAXS measurement was achieved resulting in a sampling rate of around $\frac{1}{13}\,\mathrm{s}^{-1}$ (10 s exposure time plus 3 s computation time). The short exposure time was obtained by increasing the X-ray flux at the sample position. For this purpose the novel high brilliance MetalJet X-ray source (from Excillum) was utilized and optimized, which yields a factor of approximately 3 more flux compared to the high brilliance rotating anode NanoSTAR systems. Furthermore, the X-ray beam conditioning was optimized by using only two SCATEX pinholes. This gives an additional flux increase of a factor of 2.75 compared to the standard pinhole system composed of three standard pinholes.

Silica nanoparticles were used as a sample system. Due to the short exposure time of the SAXS measurements and the possibility to adjust the synthesis conditions while ongoin production, an effective optimization and investigation of the synthesis parameters was achieved. In this work the synthesis parameters for silica nanoparticles were found for a wide size range from around 10 nm to 100 nm in diameter. It was demonstrated that the size of the nanoparticles can be tuned by adjusting the concentration of TEOS in ethanol, the flow rate ratio between the first precursor (TEOS-ethanol solution) and the second precursor (ammonia-water solution). A decrease of the ratio between TEOS

and ammonia and a decrease of the TEOS concentration lead to a decrease of the mean size of the silica nanoparticles. Moreover, a decrease of the reactor temperature results in an increase of the mean size. The influence of the overall flow rate or the residence time on the size was also investigated. An increase of the overall flow rate leads to an increase of the nanoparticle size and to a decrease of the particle number density. Moreover, the results indicate that the size distribution of the nanoparticles is narrower at a shorter residence time.

Furthermore, the VascoFlex DLS device was integrated into the NanoSTAR sample chamber. In this manner it was possible to perform simultaneous measurements together with SAXS. Simultaneous SAXS and DLS measurements were performed on silica nanoparticles in stopped flow mode. Additionally, the extension of the capabilities of DLS to characterize flowing nanoparticles was investigated. It was found that with the used DLS device and the flow-through capillary DLS measurements can be performed up to a flow rate of 1300 µl min^{-1}. This result is well above the typically used flow rates for silica nanoparticle production in this work. The combined and complementary use of DLS and SAXS facilitated to investigate the influence of reactor temperature on the nanoparticle size.

Concludingly, in this work a real-time monitoring of the production of silica nanoparticles was achieved by an optimization of the SAXS device and implementation of a dedicated monitoring software. The developed concepts of real-time monitoring can be applied to other types of nanoparticles such as Au, Ag and Si which are relevant in medical and industrial applications. As it was shown in the thesis, the real-time monitoring provides a powerful mean for fast and effective optimization of synthesis conditions. It was also shown that simultaneous SAXS and DLS measurements can be performed while nanoparticle flow. A combined and simultaneous use of DLS and SAXS can be used to monitor the functionalization of nanoparticle surfaces, which is important for biolabling and medical applications.

Chapter 8

Outlook

Based on the achievements of this thesis, future work could address different topics: Despite the advantages of a microflow reactors, the flow speed profile due to Poiseuille flow broadens the size distribution at high flow rates [40]. Therefore, to narrow the size distribution, segmented flow with inert gas should be investigated. Therefore, an additional syringe pump must be added. For DLS measurements bubbles can have a tremendous effect. Therefore, the influence of bubbles on DLS measurements must be investigated.

The results of this thesis can serve as basis for production monitoring of other types of nanoparticles such gold. Synthesis parameter can be found for different nanoparticle sizes. Furthermore, synthesis of core-shell nanoparticles can be investigated. For this purpose a second Asia flow-chemistry system is necessary. In the first reactor the core-particles are synthesized. In the second reactor the formed particles are used as seeds for the shell formation. Depending on the shell thickness and shell formation time, proper flow rates and reator volumes must be used. To find out the proper synthesis conditions for core-shell nanoparticle formation the synthesis stations can be integrated to the NanoSTAR and the flow-throug capillary as demonstrated in this thesis. A second flow-through capillary can be utilized to monitor the core-particles prior to guide them into the second reactor. In analogy, nanoparticle functionalization can be performed by utilizing a second reactor. Using SAXS and DLS simultaneously yields complementary and mutually supporting information on the core size and the functionalization layer thickness.

NanoSTAR performance can be further improved by utilizing a dedicated optics which focuses the X-ray beam on the beam stop. In combination with SCATEX pinholes the beam stop size can be decreased while preserving a high flux.

The major obstacles encoutered during the use of the DLS device is the challenging alignment of the laser beam in the center of the 2 mm capillary. To adjust the hight of the capillary with respect to the beam, the capillary must be moved manually, which is somewhat laborious and sometimes it results in an inaccurate alignment. DLS measuremets and alignment can be facilitated by the use of a motorized stage which also allows an adjustment of the hight of the DLS probe head.

Bibliography

[1] *ASTM 2456-06 Standard Terminology Relating to Nanotechnology.*

[2] *ISO ISO/TS 27687:2008 Nanotechnologies - Terminology and definitions for nano objects - nanoparticle, nanofibre and nanoplate.*

[3] *Scientific Basis for the Definition of the Term "nanomaterial".* ISSN 1831-4783 ISBN 978-92-79-12757-1, doi:10.2772/39703 ND-AS-09-004-EN-N.

[4] *VÅNTEC-2000 User Manual.* Bruker AXS, Madison, 2008.

[5] *Implementation of the Levenberg-Marquardt algorithm in Python.* http://code.google.com/p/astrolibpy/source/browse/trunk/, Date checked: 25.06.14.

[6] J. Als-Nielson and D. McMorrow. *Elements of modern X-ray physics.* John Wiley & sons, New York, 2011.

[7] U. W. Arndt. Focusing optics for laboratory sources in x-ray crystallography. *Journal of Applied Crystallography*, 23:161 – 168, 1990.

[8] Z. Bajzer, A. C. Myers, S. S. Sedarous, and F. G. Prendergast. Pade-laplace method for analysis of fluorescence intensity decay. *Biophysical Journal*, 56:79 – 93, 1989.

[9] L. E. Berman, Z. Yin, S. B. Dierker, E. Dufresne, S. G. J. Mochrie, O. K. C. Tsui, S. K. Burley, F. Shu, X. Xie, M. S. Capel, and R. M. Sweet. Performance of the double multilayer monochromator on the nsls wiggler beam line x25. *AIP Conference Proccedings*, 417:71 – 79, 1997.

[10] B. J. Berne and R. Pecora. *Dynamic Light Scattering: With Applications to Chemistry, Biology, and Physics.* John Wiley & sons, New York, 2011.

[11] R. Bienert, F. Emmerling, and A. F. Thünemann. The size distribution of gold standard nanoparticles. *Analytical and Bioanalytical Chemistry*, 395:1651 – 1660, 2009.

[12] G. H. Bogush and C. F. Zukoski IV. Uniform silica particle precipitation: An aggregative growth model. *Journal of Colloid and Interface Science*, 142:19–34, 1991.

[13] H. Boukari, J. S. Lin, and M. T. Harris. Small-angle x-ray scattering study of the formation of colloidal silica particles from alkoxides: Primary particles or not? *Journal of Colloid and Interface Science*, 194:311 – 318, 1997.

[14] H. Boukari, G. G. Long, and M. T. Harris. Polydispersity during formation and growth of the stöber silica particles from small-angle x-ray scattering measurements. *Journal of Colloid and Interface Science*, 229:129 – 139, 2000.

[15] J. M. Caruge, J. E. Halpert, V. Wood, V. Bulovi, and M. G. Bawendi. Colloidal quantum-dot light-emitting diodes with metal-oxide charge transport layers. *Nature Photonics*, 2:247 – 250, 2008.

[16] S. Chen, P. Dong, G. Yang, and J. Yang. Kinetics of formation of monodisperse colloidal silica particles through the hydrolysis and condensation of tetraethylorthosilicate. *Industrial and Engineering Chemistry Research*, 35:4487 – 4493, 1996.

[17] B. Chu and T. Liu. Characterization of nanoparticles by scattering techniques. *Journal of Nanoparticle Research*, 2:29 – 41, 2000.

[18] Y. S. Chung, M. Y. Jeon, and C. K. Kim. Fabrication of nearly monodispersed silica nanoparticles by using poly(1-vinyl-2-pyrrolidinone) and their application to the preparation of nanocomposites. *Macromolecular Research*, 17:37 – 43, 2009.

[19] B. R. Cuenya. Synthesis and catalytic properties of metal nanoparticles: Size, shape, support, composition, and oxidation state effects. *Thin Solid Films*, 518:3127 – 3150, 2010.

[20] F. Destremaut, J. B. Salmon, L. Qi, and J. P. Chapel. Microfluidics with on-line dynamic light scattering for size measurements. *Lab Chip*, 9:3289–3296, 2009.

[21] J. Eyssautiera, D. Frot, and L. Barré. Structure and dynamic properties of colloidal asphaltene aggregates. *Langmuir*, 28:11997 – 12004, 2012.

[22] L. Fan, M. Degen, S. Bendle, N. Grupido, and J. Ilavsky. The absolute calibration of a small-angle scattering instrument with a laboratory x-ray source. *Journal of Physics: Conference Series*, 247:012005, 2010.

[23] K. S. Finnie, J. R. Bartlett, and C. J. A. Barbe ang L. Kong. Formation of silica nanoparticles in microemulsions. *Langmuir*, 23:3017 – 3024, 2007.

[24] S. Fouilloux, J. Daillant, and A. Thill. Single step synthesis of 5-30 nm monodisperse silica nanoparticles: Important experimental parameters and modeling. *Colloids and Surfaces A: Physicochemical and Engineering Aspects*, 393:122 – 127, 2012.

[25] S. Fouilloux, A. Désert, O. Taché, O. Spalla, J. Daillant, and A. Thill. Saxs exploration of the synthesis of ultra monodisperse silica nanoparticles and quantitative nucleation growth modeling. *Journal of Colloid and Interface Science*, 346:79 – 86, 2010.

[26] S. Fouilloux, O. Taché, O. Spalla, and A. Thill. Nucleation of silica nanoparticles measured in situ during controlled supersaturation increase. restructuring toward a monodisperse nonspherical shape. *Langmuir*, 27:12304 – 12311, 2011.

[27] J. Freudengerber, E. Hell, and W. Knüpfer. Perspectives of medical x-ray imaging. *Nuclear Instruments and Methods in Physics Research A*, 466:99 – 104, 2001.

[28] O. Glatter. *Static Light Scattering of Large Systems.* In: Neutrons, X-rays and Light. Editors: P. Lindner and T. Zemb. Elsevier Science, 2002.

[29] D.L. Green, S. Jayasundara, Yui-Fai Lam, and M.T. Harris. Chemical reaction kinetics leading to the first stober silica nanoparticles - nmr and saxs investigations. *Journal of Non-Crystalline Solids*, 315:166–179, 2003.

[30] D.L. Green, J. S. Lin, Y. Lam, M. Z. C. Hu, D. W. Schaefer, and M.T. Harris. Size, volume fraction, and nucleation of stober silica nanoparticles. *Journal of Non-Crystalline Solids*, 266:346 – 358, 2003.

[31] L. Gutierrez, L. Gomez, S. Irusta, M. Arruebo, and J. Santamaria. Comparative study of the synthesis of silica nanoparticles in micromixer-microreactor and batch reactor systems. *Chemical Engineering Journal*, 171:674–683, 2011.

[32] K. D. Hartlen, A. P. T. Athanasopoulos, and V. Kitaev. Facile preparation of highly monodisperse small silica spheres (15 to >200 nm) suitable for colloidal templating and formation of ordered arrays. *Langmuir*, 24:1714 – 1720, 2008.

[33] B. B. He. *Two-Dimensional X-Ray Diffraction.* John Wiley & sons, 2009.

[34] P. He, G. Greenway, and S. J. Haswell. Microfluidic synthesis of silica nanoparticles using polyethylenimine polymers. *Chemical ingineering Journal*, 167:694 – 699, 2011.

[35] O. Hemberg. *Compact Liquid-Jet X-ray Source.* Dissertation, 2004.

[36] O. Hemberg, M. Otendal, and H. M. Hertz. Liquid-metal-jet anode electron-impact x-ray source. *Applied Physical Letters*, 83:1483 – 1485, 2003.

[37] F. Hertlein, S. Kroth, C. Michaelsen, A. Oehr, and J. Wiesmann. Nanoscaled multilayer coatings for x-ray optics. *Advanced Engineering Materials*, 10:686 – 691, 2008.

[38] T. B. Huff, L. Tong, Y. Zhao, M. N. Hansen, J. Cheng, and A. Wei. Hypherthermic effect of gold nanorods on tumor cells. *Nanomedicine*, 2:125 – 132, 2007.

[39] Z. Jiang, W. Yuan, and H. Pan. Luminescence effect of silver nanoparticle in water phase. *Spectroscopica Acta Part A: Molecular and Biomolecular Spectroscopy*, 61:2488 – 2494, 2005.

[40] S. A. Khan, A. Günther, M. A. Schmidt, and K. F. Jensen. Microfluidic synthesis of colloidal silica. *Langmuir*, 20:8604 – 8611, 2004.

[41] S. A. Khan and K. F. Jensen. Microfluidic synthesis of titania shells on colloidal silica. *Advanced Materials*, 19:2556 – 2560, 2007.

[42] T. Kim, K. Cho, E. K. Lee, S. J. Lee, J. Chae, J. W. Kim, D. H. Kim, J. Kwon, G. Amaratunga, S. Y. Lee, B. L. Choi, Y. Kuk, J. M. Kim, and K. Kim. Full-colour quantum dot displays fabricated by transfer printing. *Nature Photonics*, 5:176 – 182, 2011.

[43] P. Kirkpatrick and A. V. Baez. Formation of optical images by x-rays. *Journal of the Optical Society of America*, 38:766 – 773, 1948.

[44] M. Kotlarchyk and S. Chen. Analysis of small angle neutron scattering spectra from polydisperse interacting colloids. *The journal of chemical physics*, 79:2461 – 2469, 1983.

[45] E. Krestel. *Imaging Systems for Medical Diagnostics*. Siemens AG, Berlin, Munich, 1990.

[46] V. K. LaMer and R. H. Dinegar. Theory, production and mechanism of formation of monodispersed hydrosols. *Journal of the American Chemical Society*, 72:4847–4854, 1950.

[47] D. H. Larsson, U. Lundström, U. K. Westermark, M. A. Henriksson, A. Burvall, and H. M. Hertz. First application of liquid-metal-jet sources for small-animal imaging: High-resolution ct and phase-contrast tumor demarcation. *Medical Physics*, 40:021909, 2013.

[48] J. Lim, S. Ha, and J. Lee. Precise size-control of silica nanoparticles via alkoxy exchange equilibrium of tetraethyl orthosilicate (teos) in the mixed alcohol solution. *Bulletin of the Korean Chemical Society*, 33:1067–1070, 2011.

[49] C. J. Lin, C. Lee, J. Hsieh, H. Wang, J. K. Li, J. Shen, W. Chan, H. Yeh, and W. H. Chang. Synthesis of fluorescent metallic nanoclusters toward biomedical application: Recent progress and present challenges. *Journal of Medical and Biological Engineering*, 29:276 – 283, 2009.

[50] Y. Lin, K. C. Klavetter, P. R. Abel, N. C. Davy, J. L. Snider, A. Heller, and C. B. Mullins. High performance silicon nanoparticle anode in fluoroethylene carbonate-based electrolyte for li-ion batteries. *Chemical Communications*, 48:7268 – 7270, 2012.

[51] S. Link and M. A. El-Sayed. Size and temperature dependence of the plasmon absorption of colloidal gold nanoparticles. *Journal of Physical Chemistry B*, 103:4212 – 4217, 1999.

[52] T. Matsoukas and E. Gulari. Monomer-addition growth with a slow initiation step: A growth model for silica particles from alkoxides. *Journal of Colloid and Interface Science*, 132:252, 1988.

[53] M. Montel. The x-ray microscope with catamegonic roof-shaped objective. *X-ray Microscopy and Microradiography*, 5:177 – 185, 1957.

[54] K. Nakayama, K. Tanabe, and H. A. Atwater. Plasmonic nanoparticle enhanced light absoption in gaas solar cells. *Applied Physics Letters*, 93:2488 – 2494, 2008.

[55] M. Otendal, O. Hemberg, T. T. Tuohimaa, and H. M. Hertz. Microscopic high-speed liquid-metal jets in vacuum. *Experiments in Fluids*, 39:799–804, 2005.

[56] M. Otendal, T. Tuohimaa, U. Vogt, and H. M. Hertz. A 9 kev electron-impact liquid-gallium-jet x-ray source. *Review of Scientific Instruments*, 79:016102, 2008.

[57] S. K. Park, K. D. Kim, and H. T. Kim. Preparation of silica nanoparticles: determination of the optimal synthesis conditions for small and uniform particles. *Colloids and Surfaces*, 197:7–17, 2002.

[58] J. Pederson. A flux- and background-optimized version of the nanostar small-angle x-ray scattering camera for solution scattering. *Journal of Appplied Crystallography*, 37:369–380, 2004.

[59] J. S Pederson. *Modelling of Small-Angle Scattering Data from Colloids and Polymer Systems.* In: Neutrons, X-rays and Light. Editors: P. Lindner and T. Zemb. Elsevier Science, 2002.

[60] A.C. Pierre. *Introduction to Sol-Gel Processing.* Kluwer Academic Publishers, Boston, 1988.

[61] J. Polte, R. Kraehnert, M. Radtke, U. Reinholz, H. Riesemeier, A. F. ThÃ¼nemann, and F. Emmerling. New insights of the nucleation and growth process of gold nanoparticles via in situ coupling of saxs and xanes. *Journal of Physics: Conference Series*, 247:012051, 2010.

[62] P. N. Pusey. *Dynamic Light Scattering.* In: Neutrons, X-rays and Light. Editors: P. Lindner and T. Zemb. Elsevier Science, 2002.

[63] I. Ab Rahman and V. Padavettan. Synthesis of silica nanoparticles by sol-gel:size-dependent properties, surface modification, and applications in silica-polymer nanocomposites - a review. *Journal of Nanomaterials*, 2012:15, 2012.

[64] K. S. Rao, K. El-Hami, T. Kodaki, Kazumi Matsushige, and K. Makino. A novel method for synthesis of silica nanoparticles. *Journal of Colloid and Interface Science*, 289:125 – 131, 2005.

[65] W. Reschetilowski. *Principles of Microprocess Technology. In: Microreactors in Preparative Chemistry. Editor: W. Reschetilowski.* John Wiley & sons, Weinheim, 2013.

[66] P. Riello, M. Mattiazzi, J. S. Pedersen, and A. Benedetti. Time-resolved in situ small-angle x-ray scattering study of silica particle formation in nonionic water-in-oil microemulsions. *Langmuir*, 24:5225 – 5228, 2008.

[67] D. S. Sivia. *Elementary Scattering Theory.* Oxford University Press, New York, 2011.

[68] W. Stöber, A. Fink, and E. Bohn. Controlled growth of monodisperse silica spheres in the micron size range. *JOURNAL OF COLLOID AND INTERFACE SCIENCE*, 26:62–69, 1968.

[69] B. Sun, E. Marx, and N.l C. Greenham. Photovoltaic devices using blends of branched cdse nanoparticles and conjugated polymers. *Nano Letters*, 3:961 – 963, 2003.

[70] D. V. Talapin, J. Lee, M. V. Kovalenko, and E. V. Shevchenko. Prospects of colloidal nanocrystals for electronic and optoelectronic applications. *Chemical Reviews*, 110:389 – 458, 2010.

[71] R. Taylor, S. Coulombe, T. Otanicar, P. Phelan, A. Gunawan W. Lv, G. Rosengarten, R. Prasher, and H. Tyagi. Small particles, big impacts: A review of the diverse applications of nanofluids. *Journal of Applied Physics*, 113:7–17, 2013.

[72] D. J. Tobler and L. G. Benning. In situ and time resolved nucleation and growth of silica nanoparticles forming under simulated geothermal conditions. *Geochimica et Cosmochimica Acta*, 114:156 – 168, 2013.

[73] D. J. Tobler, S. Shaw, and L. G. Benning. Quantification of initial stepsof nucleation and growth of silica nanoparticles: An in-situ saxs and dls study. *Geochimica et Cosmochimica Acta*, 73:5377 – 5393, 2009.

[74] F. Vines, J. R. B. Gomes, and F. Illas. Understanding the reactivity of metallic nanoparticles: beyond the extended surface model for catalysis. *Chemical Society Reviews*, 43:4922 – 4939, 2014.

[75] J. B. Wacker, I. Lignos, V. K. Parashar, and M. A. M. Gijs. Controlled synthesis of fluorescent silica nanoparticles inside microfluidic droplets. *Lab on a chip*, 12:3111 – 3116, 2012.

[76] L. Wang, W. Zhao, and W. Tan. Bioconjugated silica nanoparticles: Development and applications. *Nano Research*, 1:99 – 115, 2008.

[77] T. Yokoi, Y. Sakamoto, O. Terasaki, Y. Kubota, T. Okubo, and T. Tatsumi. Periodic arrangement of silica nanospheres assisted by amino acids. *Journal of the Americal Chemical Sociaty*, 128:13664 – 13665, 2006.

[78] T. Yokoi, J. Wakabayashi, O. Yuki, F. Wei, M. Iwanma, R. Watanabe, K. Aramaki, A. Shimojima, T. Tatsumi, and Y. Okubo. Mechanism of formation of uniform-sized silica nanospheres catalyzed by basic amino acids. *Chemistry of Materials*, 21:3719 – 1720, 2009.

[79] H. Yuan, F. Gao, Z. Zhang, L. Miao, R. Yu, H. Zhao, and M. Lan. Study on controllable preparation of silica nanoparticles with multi-sizes and their size dependent cytotoxicity in pheochromocytoma cells and human embryonic kidney cells. *Journal of Health Science*, 56.

[80] F. Zhang, D. G. Dressen, M. W. A. Skoda, R. M. J. Jacobs, S. Zorn, R. A. Martin, C. M. Martin, G. F. Clark, and F. Schreiber. Gold nanoparticles decorated with oligo(ethylene glycol) thiols: kinetics of colloid aggregation driven by depletion forces. *European Biophysical Journal*, 37:121904, 2008.

[81] C. Zhao and A. P. J. Middelberg L. He, S. Z. Qiao. Nanoparticle synthesis in microreactros. *Chemical Engineering Science*, 66:1463 – 1479, 2011.

Acknowledgements

First I want to thank Prof. Dr. M. Tolan and Dr. L. Brügemann for giving me the opportunity to do a PhD in an exciting and industry-oriented project. I also thank the EU Commission for the financial support through the FP7-project SNOWCONTROL (263510).

Furthermore, I kindly thank the XRD department at Bruker for support. Especially, I want to express my gratitude to Dr. C. Ollinger, Dr. J. Lange and Dr. G. Evrard for valuable advice and discussions.

I want to say big thanks to the Excillum team, especially to Dr. P. Takman, Dr. M. Otendal and Dr. T. Tuohimaa for support with the MetalJet X-ray source.

A great thanks goes also Dr. D. Jacob and B. Pedrono for assistance and support with the DLS measurements.

I want to thank Prof. Dr. J. P. Locquet at KU Leuven for providing me the equipment for nanoparticle synthesis. I wish to say a big thanks to B. De Roo for assistance and support with the synthesis equipment and TEM measurements. Furthermore, I kindly thank Dr. L. Dillemans, S. Vandezande, B. Opperdoes, the electronic and the mechanical workshop staff for technical support.

I kindly thank A. Kopaczynski, M. Peters, A. Plocher for technical support.

For proof-reading I thank Dr. C. Ollinger, Dr. L. Brügemann, Dr. J. Lange, Dr. G. Evrard and Dr. M. Paulus.

Besonders möchte ich meiner Familie und Julia S. für moralische Unterstützung danken. Ihr habt auch dazu beigetragen, dass ich diese Arbeit fertigstellen konnte.

Eidesstattliche Erklärung

Hiermit erkläre ich an Eides statt, dass ich die vorliegende Arbeit ausschließlich unter Verwendung der angegebenen Hilfmittel und unter Beratung meiner wissenschaftlichen Betreuer angefertigt habe. Ich habe keine anderen als die angegebenen Quellen und Hilfsmittel benutzt sowie wörtliche und sinngemäße Zitate kenntlich gemacht. Die Arbeit wurde weder ganz noch in Teilen an anderer Stelle im Rahmen eines Prüfungsverfahrens vorgelegt.

Ort, Datum	Unterschrift